Static Analysis of Masonry Arches

Syed Hamid Safeer AHMAD

School of Computing, Science and Engineering College of Science and Technology University of Salford, Salford, UK

Submitted in Partial Fulfilment of the Requirements of the Degree of Doctor of Philosophy, July 2017

Abstract

The aim of the present research was to provide a practical theoretical model based on elementary statics, for assessment for masonry arch bridges, that benefits from the large scale experimental programme at Salford University, together with insight gained from the Distinct Element numerical modelling work.

The need for large scale laboratory controlled load tests of physical models that may be reliably confined to a specific domain of behaviour with known parameters and modelling constraints, was highlighted in chapter 2 with reference to literature.

Load tests on various distributions of surcharge were carried and the mechanisms of failure observed. The numerical modelled was shown to agree with expected theoretical behaviour and shown good agreement with experimental results.

A theoretical model was developed which benefitted from insight from the experimental and numerical work to provide a means of predicting the failure load of the arch-fill system for the lading arrangements carried out in the physical and numerical tests.

The model provided predicted failure loads for a range of material variation within a reasonable expected range and showed promising resemblance to the physical modelling results.

Acknowledgements

If this work contains anything of value, I attribute this to the Gracious God.

I pray that any shortcomings on my part may be covered by His Mercy.

I am deeply grateful to all those individuals who were inspired with the kindness and beneficence to support me in various ways during the course of my research.

I wish to acknowledge the EPSRC for granting the University of Salford the funding which enabled me to carry out this research.

I wish to express my gratitude to my supervisors Dr Gareth Swift and Jonathan Haynes for their support and guidance throughout my research.

I am also extremely grateful to my friend and colleague Dr Levingshan Augusthus Nelson who has been in constant contact with me while I have been living away from campus. He has supported me selflessly with genuine concern.

I owe immense gratitude to my wife and children who accompanied through this long and challenging journey and to my Parents and family for all their support and prayers.

Contents

Chapter 1 Introduction

1.1 Background

1.1.1 Two-dimensional modelling

Evidence of arch construction can be found in ancient civilisations dating back several millennia. Before the scientific revolution, construction was based on experience, trial and error and empirical rules.

Early theoretical developments on the stability of the masonry arches were primarily two-dimensional. These were during a time when masonry arch bridges were studied for design and construction. When construction of these structures came to an end in the early 1900's, the decades following saw little research effort in this area. As the demands on Britain's transport infrastructure grew rapidly, research activity in this area was revived, but with a focus on assessment rather than design.

A review of research carried out in the past few decades, reveals that the pursuit of an improved understanding of even the two dimensional behaviour of only a single span arch restrained to single-ring rigid voussoir action has been an active area of research in which substantial experimental and numerical efforts have been made in the present decade alone. It has become clear that further work on explicit modelling the fill and it's interaction with the arch is needed. There is currently no practical assessment methodology the ultimate limit state capacity based directly on statics. There has been a leap from early theoretical knowledge to advanced numerical modelling work, leaving a gap in the theoretical and intuitive understanding of the static stability of the arch-fill system.

The present research has focussed on an in-depth study of the static stability of the arch and fill as a composite system by means of physical, numerical and theoretical modelling. Taking a two-dimensional slice in the longitudinal direction of unit width (Figure 1.1).

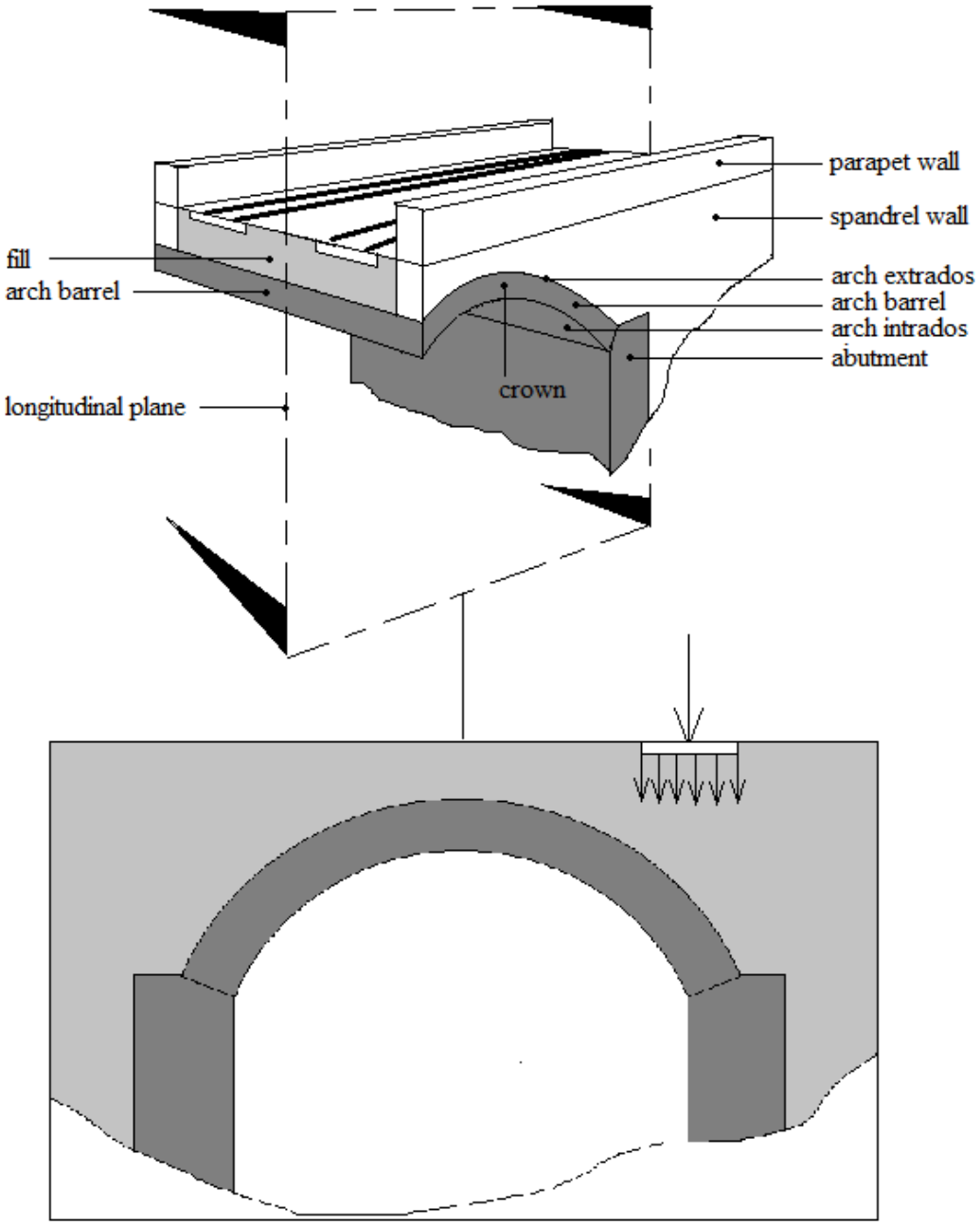

Figure 1.1 – Typical features of a masonry arch bride span and two-dimensional scope of study in the present research

The behaviour of Masonry-arch bridges is three dimensional in reality, and the role of lateral stability, out of plane buckling and increased capacity due to the spandrel wall is likely to be very important.

1.2 Modes of failure under investigation

In the theoretical model described in the present research, crushing failure of the arch barrel is not considered directly. In continuation of the research recently carried out on single-ring voussoir arches the physical model in the present research is constructed with a header bonded configuration to limit behaviour to resemble that of a single-ring voussoir arch as previously done at Salford University.

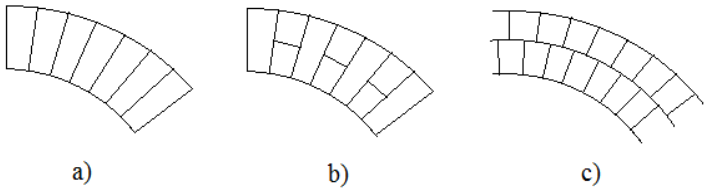

Figure 1.2 – a) Single-ring voussoir arch. b) Header-bonded construction. c) Multi-ring arch

However the effects of masonry crushing may be accounted for by reducing the thickness of the arch barrel according to some constitutive criteria. Experimental evidence as well as numerical and theoretical observations indicate that shear forces in the arch cross section are rarely permitted to reach high enough values for frictional shear to occur before rotational failure becomes incipient. Thus the most onerous mode of failure in the plain-strain arch-fill system is usually by rotational opening of radial joints about specific points of contact, termed hinges.

In the present research, the tensile and cohesive strength of masonry joints is modelled numerically for a range of values. These have a significant influence on the load bearing capacity of the system; however these have not been included in the theoretical model for reasons discussed in Chapter 2.

Failure of the arch in shear, i.e. relative sliding of radial joints is very unlikely other than for unusual geometric and loading conditions as discussed in section #. The reason for this becomes clearer on consideration of the basic statics of the arch fill system under a concentrated surcharge, as discussed in section #. Shear failure of the masonry in the direction tangential to the arch, i.e. inter-laminate sliding as may occur in multi-ring arches is also eliminated from the present study by using header-bonded construction in the physical model as shown in Figure 1.2b.

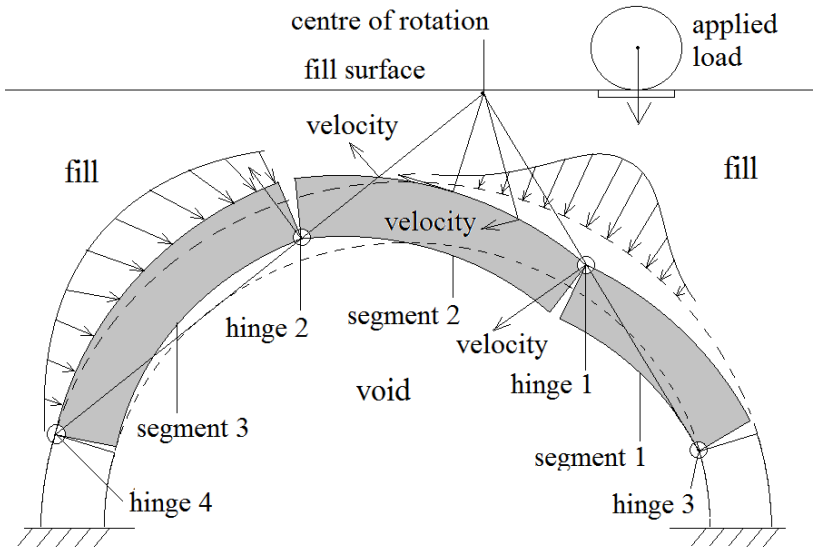

Figure 1.3 – Typical four-hinged rotational failure of a masonry-arch bridge

For some geometric and loading configurations it may not be possible for a purely rotational failure mechanism to occur, in these cases, the additional degree of freedom is released by translation of an abutment. The role of abutment translation on the single span arches as well as sway at intermediate piers in multi-span arch bridges is discussed in Chapter 4.

Furthermore, the initial failure mechanism may only be a transient one and can often be very different to the ultimate failure mechanism. An advantage of the numerical modelling software used in the present research (UDEC) is that it is a time-stepping scheme that re-evaluates the statics as well as kinematics of the system continuously as loading progresses. If loading or displacement is increased slowly enough, inertial terms become negligible and equilibrium may

be assumed. This enables any transient processes to be distinguished from the residual state after ultimate failure.

1.3 Problems related to fill-arch interaction

The invaluable experimental work carried out in the 1930's by Pippard et al resulted in Pippard's elastic analysis of arches and was followed by Heyman's work on the static's and stability of arches. This was a prime example of theoretical development in the area of static analysis of arches that benefitted directly from experimental work and visa versa.

Heyman and others later, described geometrically the relationship between a set of vertical point loads and the corresponding polygon of internal forces within the arch to transmit these to the abutments and the conditions under which failure mechanisms may occur.

1. These existing models require further generalisation to enable soil-structure interaction studies. In order to apply realistic loading to the arch, to fully capture the loads due to interaction with the fill, normal stresses as well as traction components need to be considered which may be continuous stress distributions.
2. The aforementioned aspect of the model only deals with the general relationship between stresses acting at the arch-fill interface and internal forces within the arch. In order for the static stability of an arch-fill system to be assessed, methods for modelling the fill are required for two key situations.
    a. Transmission of surcharge by the fill to the arch
    b. Resistance of the fill to deformation of the arch.

    The transmission of surcharge by the fill material has been treated very simplistically to date. Current UK practices such as Highways Agency, Netweor Rail and London Underground recommend simple longitudinal distribution at a fixed gradient of 1:2; horizontal : vertical which has not been justified by research and workers such as Harvey have highlighted the need for re-evaluation of this area. (Callaway et al 2011)

    The only attempts to model the resistance experienced by the arch from the fill as a Mohr-Coulomb medium have been through the use of numerical modelling software. Some bespoke numerical models have been setup with special one-dimensional elements to idealise the resistance from the fill, however these have grossly simplified the

behaviour of the fill and the assumptions used have only been justified by the absence of any better alternative.

3. There is nothing stopping the pressures due to a) - dispersed from the applied surcharge, from overlapping specially on the arch with pressures due to b) - Resistance of the fill to deformation of the arch. This potentially results in a coupled interaction of the applied surcharge (active) pressure reaching the arch on one hand and the (passive) pressure resisting displacement of the arch into the fill on the other. Pressures causing deformation of the arch need to be clearly distinguished from those that are a reaction to arch deformation in order for straightforward static stability assessment to be carried out.

1.4 Contributions of the present research

1. A generalised equilibrium formulation to account for this level of interaction is described in the present thesis (section#). This takes a continuous pressure distribution over the arch with both normal and traction components and provides a continuous mathematical relationship between these external pressures and the internal line of thrust. A system of equilibrium differential equations is formulated and their simultaneous solution is shown to agree with the direct application of static equilibrium.
2.
    a. In the present thesis, the Boussinesq distribution has been applied, accounting for the horizontal stress components which have previously been ignored. A novel application of the Boussinesq distribution in the present thesis is consideration of the change in direction of the horizontal component of pressure either side of the resultant surcharge described in section#. The curvature of the arch-fill interface has also been accounted for in the present application of the Boussinesq distribution. The analytical model, makes use of simple statics to establish the direct causal relationship between an arbitrary stress distribution acting on the arch and the resulting forces transmitted through the arch-fill system in the context of the limiting equilibrium state for stability analysis.

b. A novel analytical model is presented in the present research that generalises Rankine passive earth pressure theory for smooth vertical retaining walls, to extend the same approach so that it may be applied to the curved arch interface with the bridge fill, including friction at the interface, as discussed in section #. One of the aims of the present research is to provide an improved idealisation of the resistance experienced by the arch from the fill and an analysis procedure that is at least as rigorous as existing analytical methods used for geotechnical analysis of earth retaining walls in current practice. For this reason the novel analytical model presented in this thesis has been limited to the non-associative Mohr-Coulomb, perfectly plastic shear failure model commonly used for geotechnical analysis. The role of dilation and other complexities of the behaviour of the fill are discussed, however are beyond the scope of the model presented present research although further work to extend the present model to account for the effects of dilation is recommended.

3. A procedure for two-dimensional static analysis of masonry arches with backfill, subject to a concentrated or arbitrarily distributed surcharge is presented in the present thesis, which benefits from insight gained from experimental and numerical observations carried out hand-in-hand. One of the benefits of the experimental and numerical observations was been a deeper insight in to the role of the fill in the failure mechanism of the composite system this has enabled some assumptions to be made which enable the separation of pressures in to the two parts below. Further insight gained about the systems behaviour has enable the difficulties of the coupled system to be broken down into a straightforward analysis procedure, described in section #.
    a. 'known' pressures – i.e. those that come directly from the known dead loads and dispersal of known surcharge.
    b. 'unknown' pressures – i.e. those that are a reaction to deformation of the arch. These are initially unknown because they depend on the specific locations of hinges. The locations of hinges also depend on these 'unknown' pressures

Chapter 2 Physical Modelling

2.1 Background

2.1.1 Pippard's Experiments

At the request of the Building Research Board, Pippard et al (1936) very precisely constructed a model voussoir arch at Imperial College London, in order to investigate aspects of the mechanics of the voussoir arch. In particular, the opening and closing of hinges in response to an imposed point load as it increases, and its relationship to the horizontal thrust. A detailed description of these experiments is given in Pippard et al (1936).

The apparatus consisted of a set of fifteen precisely machined steel voussoirs, spanning four feet and rise one foot. This was in order to experiment on an arch with definite elastic properties. A thin rubber sheet was used to provide more consistent behaviour at the interfaces. The design of Pippard's apparatus is shown in Figure 2.1 below.

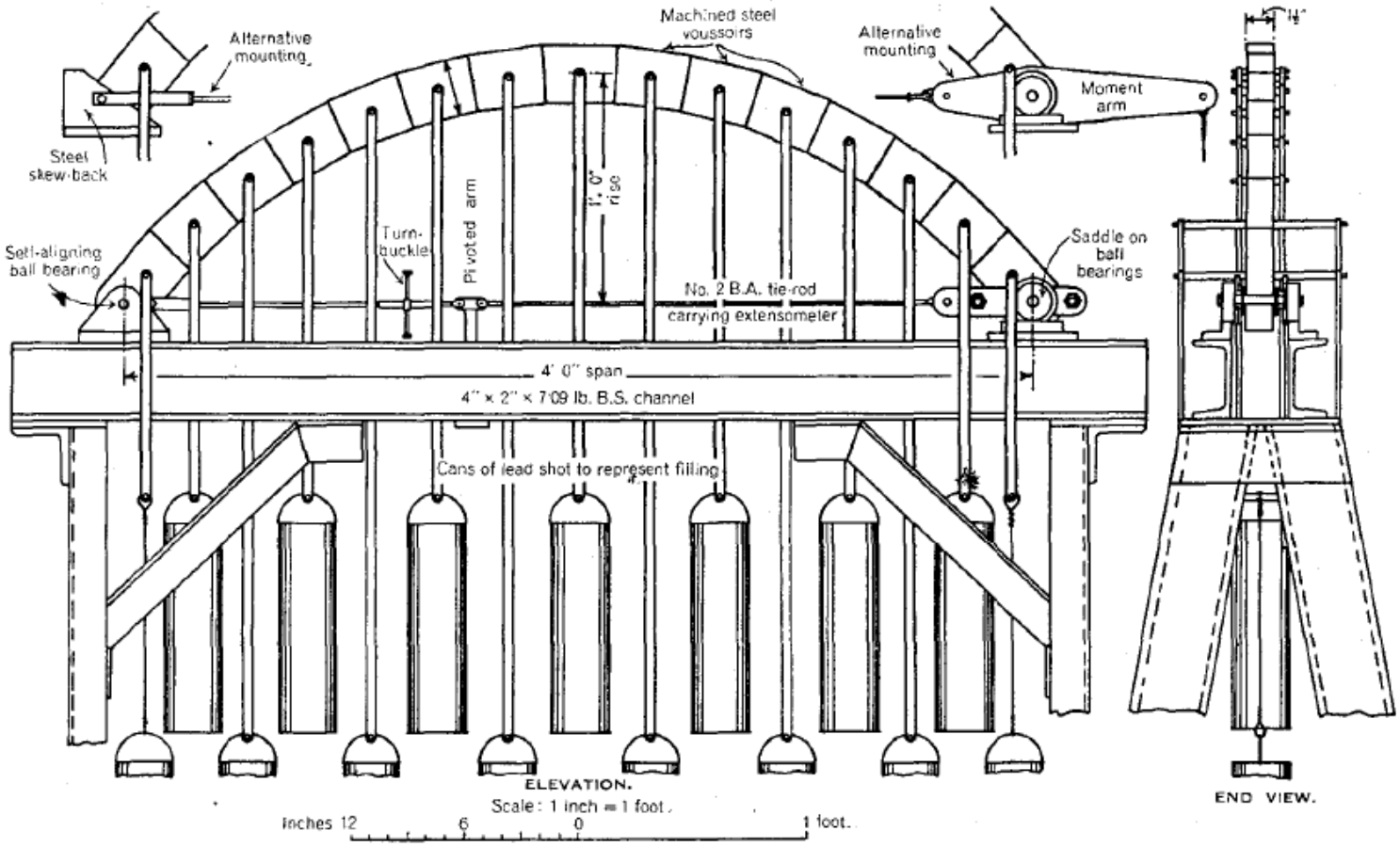

Figure 2.1: Experimental Apparatus of Pippard's steel voussoir arch tests (after Pippard et al, 1936)

Weights were hung from voussoirs to simulate dead load from fill and an extra weight was hung at specified points to represent live load. The first set of experiments were with pinned supports at both abutments. The relationship between vertical load and horizontal thrust at abutments was measured for different live load positions.

As highlighted earlier, Pippard advocated that in reality masonry arches would be effectively three pined arches under their own dead load, due to imperfect contact at supports which may be caused, for example, by horizontal or differential settlement of the abutments. This may also be caused by setting out error of the abutments so that they are closer together than the designed span.

> *"In order to complete the investigation, therefore, observations were made of the behaviour of the model structure when the arch was given a small but definite spread and also when the abutments were brought closer together"*

It should be noted here, that the hinges at the abutments in Pippard's two-pinned model structure are not representative of a voussoir arch mechanism; the pins are located at the centre of the section, so that the thrust line is forced to always pass through the centre of the end voussoir or springing. In a real voussoir arch, however, the thrust line may be anywhere within the section and in the case of the existence of a hinge; this would be either at the intrados or the extrados of the springing, which, in general, would affect the overall shape of the thrust line.

Figure 2.2(a) illustrates the gradual migration of the third hinge from the central voussoir, towards the loaded voussoir, as the load is gradually increased. This phenomenon is a clear demonstration of the effect of a point load on the thrust line within the arch. The hinge remained at its final position, beside the loaded voussoir toward the centre, until failure. When the load was removed, the hinge returned to its original position, to the left of the central voussoir. These observations were consistent on subsequent loading and unloading. From this, Pippard concluded that when a two-pinned arch is spread slightly at the abutments, it becomes effectively a three pinned arch with a hinge on the extrados. Conversely, it was observed that when the abutments were contracted, a hinge formed on the intrados, initially beside the central voussoir, but on the opposite side to that of the loaded voussoir. As the load was gradually increased, the hinge migrated away from the loaded voussoir (Figure 2.2 (b))

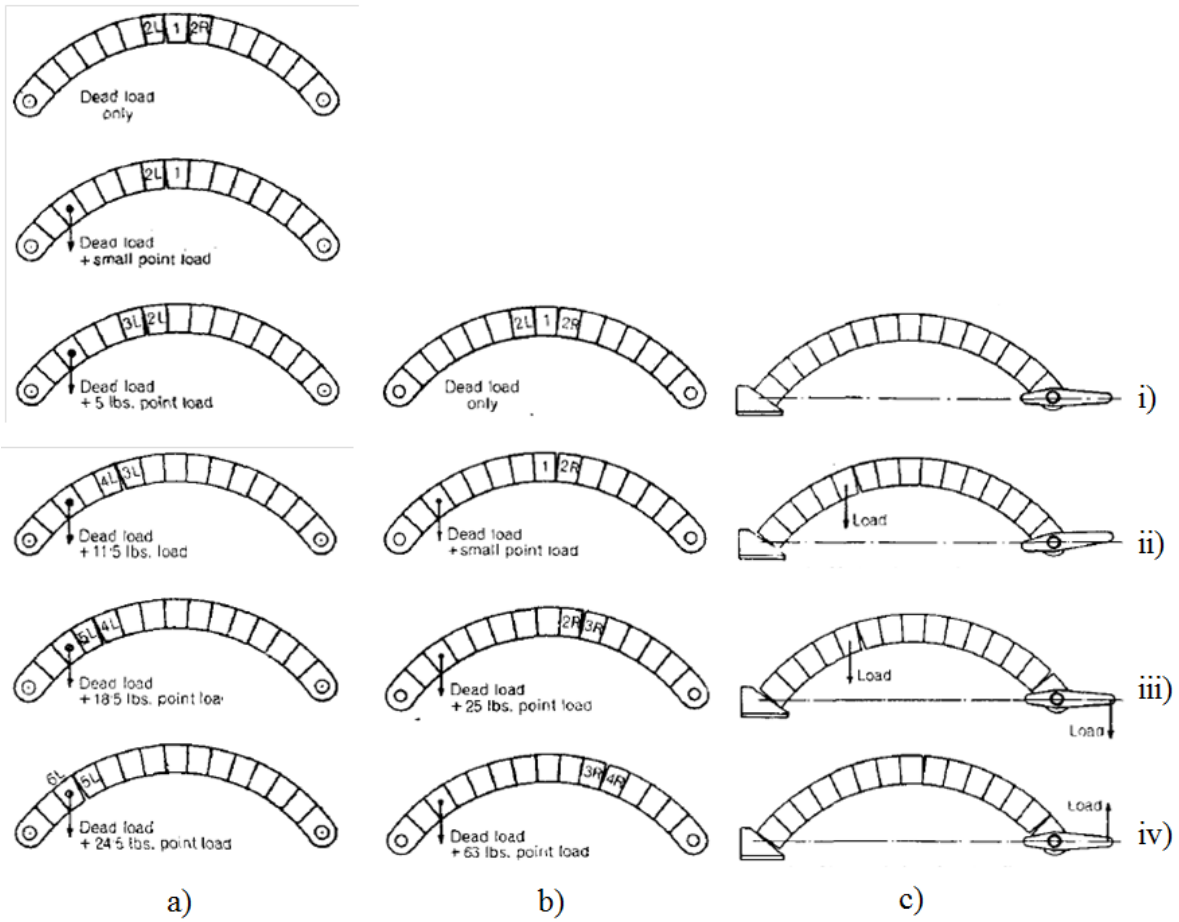

Figure 2.2: a) Under dead load only, (top left) a double hinge exists either side of the central voussoir, as the load is gradually increased, the hinge migrates towards the loaded voussoir
b) When the abutments are contracted, the initial hinge is on the intrados, opening on the extrados. As the load is increased, it closes the existing hinge as before, but the new hinge opens away from the loaded voussoir.
c) (i) Arch trued (ii) Abutments spread, arch free to rotate (iii) Abutments spread, no rotation of skewbacks (iv) Abutments too close together, no rotation of skewbacks. (after Pippard et al (1936))

The highly idealised model structure used by Pippard et al (1936) was developed further to include some more realistic characteristics of a masonry arch. Pippard and Ashby (1939) used a larger apparatus than previously used as well as mortar joints, introducing non-zero tensile capacity and concrete voussoirs, introducing the possibility of material failure in compression. The new arch was built as large as possible within the practical constraints of the laboratory. The same span to rise ratio of 4:1 was maintained as in his steel arch, this time with a span of 10 feet and rise of 2.5 feet.

Two sets of loads were used to represent the vertical deadweight of the backfill; 'light' and 'heavy'. The light loading was estimated on a fill height of 6 inches above the crown and a density of 70 lb. per cubic foot. The heavy loading was estimated on a 12 fill depth at the crown, of density 140 lb. per cubic foot. The majority of the tests were made under the light loading; the distribution of dead load is shown in Figure 2.3. One test was, however, made with heavier loading.

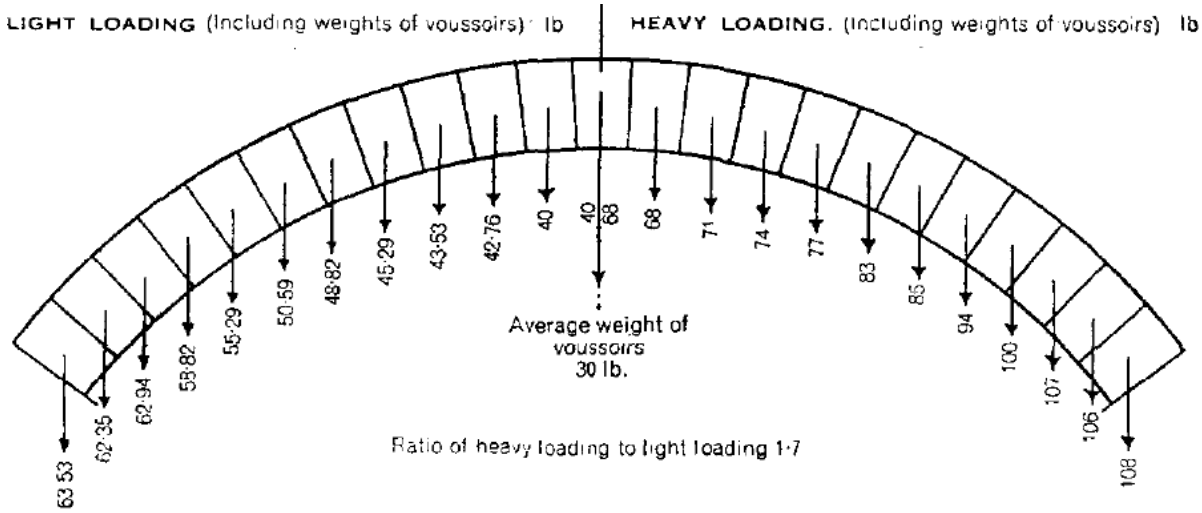

Figure 2.3: Distribution of dead load applied to the masonry voussoir arch to represent fill (after Pippard and Ashby, 1939)

Seven series of tests were made on arches built in various combinations of limestone or granite voussoirs and Non-hydraulic lime or Rapid-hardening Portland cement mortar.

- *"The non-hydraulic lime gives a mortar with practically no tensile strength, and it was used solely to form a bedding for the voussoirs. It is also weak in compression compared with cement mortar. "*
- *"The cement mortar was a mixture of rapid-hardening Portland cement and sand in the proportion 1 : 3 by weight."*

The following procedure was followed in these tests:

- *"Each test consisted in applying an extra load to one or other of the voussoirs by means of a turnbuckle attached to a spring balance "*
- *"The load was gradually increased by suitable increments while observers kept careful watch on the tell-tales* (plaster of Paris smeared over joints). *The normal observations made were the loads causing the appearance of the first tension-crack and subsequent cracks, and the positions of these failures. The test was continued until complete failure occurred, usually by the development of a fourth " pin-point "* (or hinge) *causing the structure to become unstable, or in some cases by spalling of the voussoirs, or by slipping along a joint."*

Pippard et al observed:

- *"It was found that the load could be steadily increased to the value at which a fourth pin developed, when a sudden collapse occurred. The centring of the arch prevented a complete break-up, and on removing the point load it was generally found that the structure returned to its original position unless slipping between voussoirs had occurred."*

2.1.1.1 Early load tests on field Bridges

Das (1995) reports that soon after the start of Professor Pippard's research, the Building Research Station itself began a programme of tests on behalf of the Ministry of Transport on actual arch bridges under applied vehicle loads of various configurations. In 1942, the Ministry of War Transport asked the Station to carry out similar tests on typical arch and other older types of bridges for assessment purposes. The results of these tests were then used as the basis for the assessment of other similar types. Full details of these tests were recorded by (Davey, 1953). Based on the tests, the Building Research Station recommended the following criterion for the assessment of arch bridges:

For bridges up to 45 feet span, under a single 20-ton axle

(1) The spread (increase in span) should not exceed 0.015 in.

(2) The deflection at the crown should not exceed 0.05 in.

If the above criteria were satisfied, it was considered safe for the bridge to carry a 40-ton bogie.

The above criterion was derived from the load deflection characteristics observed in a number of collapse tests on the basis that pins (hinges) did not form until such deflections were reached.

This was later confirmed by Chettoe and Henderson (1957) through tests.

These load tests were intended to extend the work already reported by Davey et al (1953) for the Building Research Station (B.R.S.) at the request of the Ministry of Transport by testing a variety of bridges under a greater range of loads than was available to the B.R.S., using the same assessment criteria for crown deflection and abutment spread described above, by Davey et al (1953).

Chettoe and Henderson were conscious of the wide variety that exists in masonry arch bridges and the countless parameters that vary from bridge to bridge. Recognising that it would be impossible to conduct such a large number of tests that would make it meaningful isolate

parameters, they tried to derive a method of assessment based on the elastic behaviour of an ideal arch,

" ..with allowances, where necessary, for other factors. "

Although the arches were comparatively few in number to those of Davey et al (1953), Chettoe and Henderson observed that the tested bridges were fairly representative.

A key advancement of the load testing program of Chettoe and Henderson, following that of Davey et al was their ability to apply far greater loads. In this investigation deflexion and spread were measured at various load increments, located above the crown. A test vehicle was used that was able to apply loads ranging from 20 tons by increments of 6 tons to 90 tons-a far heavier test load than had previously been used. The maximum load used in the previous tests by Davey et al was a 36-ton on a bogie or a maximum single axle of 27 tons. The loading arrangement of the test vehicle is described on detail in Chettoe and Henderson, (1957).

Comparison with the BRS tests reported by Davey et al (1953)

Due to the wide and complex variations amongst masonry arch bridges, Chettoe and Henderson found that it was very difficult to directly compare the results, even for apparently very similar bridges. Chettoe and Henderson observed very inconsistent behaviour between apparently very similar bridges. They set out to interpret the test results with the aim of answering, as far as possible, the following questions.

- What dispersion of load through the fill covering the arch ring can be assumed?
- What allowance can be made for transverse strength of the bridge and the possibility of there being slab action?
- To what extent can it be assumed that masonry arches behave elastically?
- What is the effect of abutment movement?
- What allowance can be made for the strength contribution of the fill, the parapet, and the spandrel walls?
- To what extent can mortar joints be assumed to carry tension?

Chettoe and Henderson presented the results of these tests in a very large number of figures, including plots of the deflection profiles of the transverse sections of the bridges for all load increments. These are not presented here as they are not relevant to the present research. The plots of primary importance however are those that show the vertical crown deflection verses load. The reader is referred to paper cited in this section.

The presence of mortar joints, with non-zero tensile capacity also makes more likely that the transition from elastic rib behaviour to mechanism behaviour would be more abrupt as well as stable (due to the fill), than the gradual transition observed in Pippard and Ashby (1939). confirms that, although the load verses deflection plots are all fairly linear, the bridges were not behaving elastically since significant residual deformation was observed. For the same bridge, the consistent recovery of spread shows that this residual deflection of the crown was occurring due to deformation in the masonry rather than movement of the supports.

2.1.1.2 Transport Research Laboratory Tests

After attempts to codify arch bridge assessment with the MEXE rules, developed after the second world war and later modified to take account of the needs of civilian traffic and civil engineers, the code of practice remained unchanged for several decades. Research in this area, however did continue. A step forward was made with the publication of the Departmental Standard BD21/84 (Department of Transport, 1984a) and companion advice note, BA16/84 (Department of Transport, 1984b), following the initiation of a major programme of research in the late 1970s. These documents introduced the concept of equilibrium analysis of arches as described by Heyman.

Das (1995) relates that by 1991, Bridges Engineering Division of the Department of Transport, had the results of collapse tests carried out under a Transport Research Laboratory (TRL) programme on 9 redundant bridges and 2 small-scale models, and the details of a number of computer based failure analysis methods. In addition, the Department was also supplied with the theoretical estimates of the ultimate capacities of the 10 bridges tested to failure. Bridges Engineering Division of the Department of Transport had the task of revising the Assessment

Code recommendations based on this information, and in particular, the task of determining the appropriate factors of safety to be applied with these methods.

Harvey(2002) further relates that in 1993, a revision to the departmental standard was produced (BD21/93) in an effort to derive benefit from the program of experimental and numerical research that followed BD21/84 into the revised document. According to Harvey, subsequent revisions of this document have brought relatively insignificant improvement.

The tests mentioned above, carried out by TRL, are reviewed in this section. These were a series of load tests to failure or near failure on eleven masonry arch bridges undertaken between 1984 and 1994. The series covered a wide variety of spans, materials and conditions and a wide variety of maximum loads and failure modes were achieved. The details of the procedure followed and the results are available in **Error! Reference source not found.**

Discussion

From these tests it can be seen that there is wide diversity and complexity in masonry arch bridges. Although a standard procedure was intended, the method of applying the load had to be adapted to suit each bridge, so that in practice, it was not possible to maintain much consistency in the test conditions. For example, as described earlier by Page (1995), the entire loading rig was supported on steel rods that passed through holes drilled straight through the bridge. As the bridge deformed laterally, the entire loading rig would move with it, while the steel rods passing through the bridge would bend and interact heavily with the arch mechanism. The methods used to analyse these bridges, were based on simplifications that did not allow them to take into account significant features of the bridge behaviour, such as the contribution of the spandrel walls, and 3D effects, introducing uncertainty to the results.

For example the, the modified MEXE method of assessment was recommended in UK practice, (BD 21/93 and BA 16/93, Department of Transport, 1993a, b) before other methods of analysis are attempted. It calculates the allowable axel loads for a single axel, two and three axel bogies and as such, is not directly comparable with these load tests. In fact, based on the following

conditions, given in BD 21/93, for seven of the eleven bridges tested, it was doubtful whether the MEXE method was applicable at all, as reported by Page (1995):

- It is not intended for use with heavily skewed bridges such as Barlae.

- Where the depth of fill is greater than the arch ring thickness, BD 21/93 states that the results should be confirmed by a more rigorous method; this applies to Bargower, Preston, Bolton model and Rotherham Road.

- Where the arch is appreciably deformed, BA 16/93 states that the method should not be used; this applies to Prestwood.

- The method is not intended for use with multi-span bridges such as Rotherham Road unless the intermediate piers are short and stocky enough to treat each span as an individual single arch span; the load test on Rotherham Road suggested this was

The results from various methods of analysis were obtained and provided for consideration by the Department of Transport in the publication of BD21/93. Harvey noted much inconsistency in the performance of these analyses in predicting the failure load from bridge to bridge. The methods used involved, Pippard's elastic method, the mechanism method and 2D finite element models. Harvey plotted the predicted failure loads of the various methods used as percentages of the actual failure loads for each bridge.

These results illustrated the various issues. In order to develop more reliable models, we will need to gain deeper insight into the behaviour of the masonry arch bridges. This requires careful experimentation and detailed measurement. Individual aspects of the masonry arch bridge behaviour need to be systematically isolated as precisely as possible. This is important so that objective conclusions may be made that are based on reliable and accurate experimental evidence and can justifiably be generalised in to improved models. From field tests such those described so far, it is clear that this is very difficult due to the unavoidable and gross variability from test to test. In addition, for a given test, it is impossible to gain accurate information about any of the materials involved in the bridge, whether masonry, fill or internal features, as

explained in section 1. This makes it impossible to isolate any individual aspects for study, so that that causes of variability in capacity from bridge to bridge may be identified with any certainty.

2.2 Experiments on backfilled masonry arches

2.2.1 Introduction

From Pippard's experiments' in the 1930's on model voussoir arches, to the TRL tests on complete masonry arch bridges, we have seen the extent of complexity in these structures. The precision and simplicity of Pippard's laboratory sized model arches, enabled him to closely observe their qualitative as well as quantitative behaviour. This enabled Pippard to draw conclusions about the fundamental mechanisms of idealised voussoir arches. These conclusions, however definite, were drawn from experiments on highly idealised models and thus limited in their validity for the assessment of real masonry arches. Analytical models were developed based on understanding gained from these experiments, which were later developed into numerical models and computer algorithms. By the late 1990's in light of the results from the TRL load tests, it became apparent that existing models were not capable of capturing the complexity of real masonry arch bridges. This was true even for the full scale models at Bolton and Dundee, due to the complexity of their three dimensional behaviour.

On one hand, idealised laboratory models enable detailed measurements to be taken but do not represent the complexity of real bridge. On the other hand, in load tests on complete bridges, very little information is provided apart from the geometry and the failure load, although this information represents the real response of the bridge. Even if an abundance of measurements were taken in the later case, the data would be impossible to interpret without an understanding of the complex processes and their relative influence on various aspects of the response of the bridge, unless a sufficient degree of control is introduced in order to isolate parameters of interest.

In light of the above, and the limited of understanding of the complex behaviour of masonry arch bridges, workers at Salford and Sheffield Universities sought a compromise in their experimental apparatus, which have been designed to provide high quality data under controlled boundary conditions, while accommodating essential aspects of the interaction of the fill, masonry arch and abutments. These include small scale physical models at Sheffield University and large scale models at Salford University (to which the author is party).

They decided to eliminate the three-dimensional components of the bridge, the third dimension being in the lateral direction (the horizontal axis, perpendicular to the span of the arch) and to study the complex composite behaviour of the soil fill and the masonry arch in the longitudinal plane (i.e. parallel to the arch span).

In order to eliminate the three dimensional aspects of the bridge and simulate plain strain conditions in the laboratory model, firstly, the spandrel walls were excluded and the fill was contained within a very stiff walled chamber. Secondly, the inside faces of the longitudinal walls were treated in order to minimise friction.

Recent intrusive investigations performed on local authority owned bridges in the UK have frequently identified that abutments are relatively insubstantial (i.e. not much wider than the thickness of the arch itself) and that a wide range of fill material exist, from granular fill, to clays. As steps toward addressing these aspects of diversity among masonry arch bridges, the Salford and Sheffield tests are being conducted with granular as well as clay fills. To create more realistic support conditions at the arch springings, the abutments were designed with a horizontal mortar joint below the springings in order to model the complexity of yielding supports and their interaction with passive soil pressure.

In order to observe the two-dimensional displacement field of the fill using imaging techniques, one of the longitudinal walls were made of transparent acrylic, lined with silicone grease and thin latex sheet. In the case of the small scale tests, the latex sheet was excluded due to poor visibility, and a single acrylic panel provided sufficient stiffness to simulate plain strain conditions under the pressures involved. In the case of the large scale tests, acrylic panels were

fitted between an array of vertical steel beams within a structural frame forming the longitudinal wall of the chamber designed to achieve sufficient stiffness to simulate plain strain conditions.

All arch barrels tested within both setups are of identical geometry. These are segmental arches with span to rise ratio of 4:1. The large scale arches are constructed with 'header bonds' (Figure 2.4) so as to behave as a single ring. The masonry is laid in the traditional manner by an experienced bricklayer. The small scale arches are one quarter scale of the large scale arches with equivalent ring thickness. However, the width is not equal, but this should not have an effect of the comparability of results since this is the irrelevant dimension in the plain strain assumption. The voussoirs of this arch are cut from clay bricks and are joined by a non-cohesive soil.

Figure 2.4: Header bonded arch barrel construction

Scaling laws, however prohibit the direct comparability of results between the small and large scale tests; stresses in the small scale tests are not representative of those in the large scale tests. A solution to this problem in small scale mechanical models has been found through the use of centrifuges (e.g. Burroughs et al. 2002), which enable experiments to be carried out under several g. However, it is very difficult and time consuming to conduct tests in this manner, which

also limits the scope of the apparatus. To minimise the influence of stress-level related issues, the arch barrel is composed of rigid blocks separated by frictional soil.

The most onerous position to apply a vertical point load on a segmental arch is considered to be at quarter span. This is also the position conventionally used by most experimenters in past research. In order to keep all tests as consistent as possible every arch loaded to failure in these apparatus was loaded at quarter span. In order to maintain plain strain conditions the load was applied evenly across the entire width of the arch by means of a rigid beam (bearing beam). The width of the beam was of an appropriate width so as not to cause premature failure of the soil fill. The load is applied by means of a servo controlled hydraulic actuator. The relevant dimensions are shown in **Error! Reference source not found.** for the large scale tests.

Insight from an understanding of active and passive soil pressures on retaining walls, together with that of the four hinged mechanism that develops in arches under such loading, indicated that active and passive actions of the fill are developed on the loaded and opposite sides of the arch respectively. This indicated that the horizontal range within which significant influence on the fill in response to the arch deformation, would be greater on the passive side than on the active (loaded) side. Earlier small scale tests (Calloway 2007) confirmed this.

As a result, the arch barrel was positioned with the loaded side closer to the end of the chamber (see **Error! Reference source not found.**), leaving a greater range of fill material on the other side. This was done to minimise the influence of the end walls on the stresses experienced by the arch barrel so as to minimise the error in generalising results to real bridges which are not confined in this way.

2.3 Recent Experimental work on Backfilled Masonry arches

Laboratory Tests on 3D Multi-span backfilled arches with spandrel wall at Bolton Inst.

Melbourne et al (1995b) constructed a full scale masonry rch bridge under laboratory conditions, this was a realistic model, incorporating most degrees of freedom including in the transverse direction, such that it3 dimensional modes of deformation or failure were also free to occur as the system was not confined. The bridge include brickwork spandrel wall, constructed in the usual way and the arches were multi-ringed, allowing the possibility of delimitation of arch rings. Pressure cells were installed on the arch extrados and deflections were monitored. The test to failure provided useful insight into the failure mechanism as it could be observed closely and in a controlled manner. However it was not possible to observe the deformation of the fill or the failure mechanism of the arch-fill system during the test.

Small Scale 2D tests with backfill at Sheffield

Calloway et al (2012), Made significant progress in this regard, using a small scale test chamber designed to confine a model arch-fill system to plain strain conditions and was also transparent on one side to enable image analysis of the deformation of the fill during load tests. A number of test were carried in order to observe the respective effects of the backfill on the loaded side of the bridge and the restraining effect of fill on the side of the arch furthes from the applied load. These two sides of the arch crown were separated by inclusion of a physical vertical barrier fied to the crown, to force a separation between the role of the fill on either side. With this apparatus, various loading scenarios were tested, including point loads applied directly to the arch with back fill on the other side to for restraint. Also repeating the same scenario with fill on both sides to observe influence of the fill. The fill range of scenarios are described in detail in Calloway et al (2012).

However real nature of separation between the fills influent on the loaded side and that on the furthest side of the arch is not known. In fact it cannot be assumed that these tow aspects of the fill’s interaction with the arch can be separated at all.

Preliminary large scale tests at Salford

Preliminary tests on the apparatus described in section 2.2 earlier, were carried out prior to the present research. The arches in these preliminary tests were constructed in an identical manner as those in the present research. Gilbert et al (2007) report that the main initial objective of these tests was to prove the test apparatus. The first test bridge was designed to be similar to the 3m span bridges tested at Bolton in the 1990s (Melbourne and Gilbert 1995), thereby permitting direct comparison. However, unlike the Bolton bridges, which had been constructed between rigid abutments, potentially movable abutments were specified and furthermore the walls of the plane-strain test chamber marked the edges of the bridge, rather than brickwork spandrel walls as used previously. The second test bridge was designed to be identical to the first with the exception that fill material below the level of the crown of the arch was replaced with a soft clay, representative of that found in some local authority owned bridges in the UK.

2.4 Apparatus and Procedure

This section describes the physical model used for the present research, to study the behaviour of a masonry arch with backfill, subjected to a vertical load at the surface of the fill.

As discussed in section 2.3, there are a number of problems associated with small scale models when studying soil structure interaction in geotechnical structures. To avoid these problems so that the physical model may better represent the conditions within a real masonry-arch bridge, a large scale model was constructed for the purpose of the present research. The construction of the arch and abutments is described in the present section.

As stated in section #, an aim the present research is to study the fundamental two-dimensional behaviour of the arch-fill system. To enable investigation of the only two-dimensional behaviour of the arch-fill system, the model was confined to plane strain conditions as far as possible using a specially designed test chamber. The fill was placed and compacted in a controlled manner so as to enable a reliable and repeatable density. The procedure for placement of the fill within the test chamber is described in section #. The special features of the test chamber to facilitate two-dimensional modelling are described in section #. With the same objective, multi-ring behaviour has been eliminated in the design and construction of the arches, as described in section #. The abutments have been designed to enable displacement and rotation as described in section #.

The test apparatus setup was largely a precise replication of an earlier series of tests (EP0) for which the test chamber mentioned above, was originally designed and constructed. EP0 consisted of a single actuator load, slowly increased up to and beyond peak capacity of the fill-arch system, bearing on a rectangular hollow section steel beam representing a statically loaded sleeper at quarter span of the arch. The confining structure and load reaction frame was re-used in the test series carried out for the present research. The results of the former tests are also compared with those carried out during the present research, primarily to assess the repeatability of the model construction and apparatus setup.

In the tests prior to the present research as well as during the present research, two types of fill material were tested. The first was a MOT type 1 aggregate of crushed limestone, a cohesionless

frictional fill of low moisture content. The second was a moist, high plasticity clay. The present thesis has only studied the case of cohesionless fill.

In addition to a repeat of the former test (EP0), several new loading regimes were introduced along with associated structures and apparatus during the present research. All physical model tests used in the present study are listed below.

i. EP1 – The fill-arch system was first subjected to 1 million cycles of service loading by means of a five actuators, each bearing on steel beams representing sleepers. Each on the 1 millions cycles consisted of an oscillation of the actuator loads in sequence so as to simulate a moving axel load across the bridge to represent a prolonged period of service. Subsequently a steadily increasing load was applied to one sleeper at quarter span position, slowly enough to avoid any inertial component, passed ultimate failure of the system and continued to achieve a steady state of yield before undoing.
ii. EP2 – This was an exact repeat of EP1 but without the cyclic loading regime
iii. EP3
    a. EP3 PH1- the cyclic loading regime applied in EP1 was repeated, followed by a s steadily increasing static load applied over three steel sleepers, equally spaced and connected by a high stiffness longitudinal beam. The steel sleepers were positioned at mid-span, quarter-span and end of span as shown in Figure #.
    b. EP3 PH2 – Following EP3 PH1, a series of restorative loads were applied sequentially, starting from the side furthest actuator from the position at which the static load to failure was applied in EP3 PH1, and working towards he crown. The purpose of this sequence of loading was to resort the arch to it's original configuration as far as possible. Another cyclic loading regime of 10^5 cycles was then applied to the system in order to re-bed the system to a more realistic state. Subsequently, the same static loading regime to failure as was applied in EP3 PH1 was applied to the restored system. The purpose of the EP3 PH2 was to investigate the residual strength of the fill-arch system after having failed at least once in the past.

c. EP3 PH3 – This was a repeat of EP3 PH3 but with the three sleepers spaced at half the spacing as in EP3 PH2, i.e.1/8th span, ¼ span and 3/8th span.

During all of the tests listed above, the arch and apparatus were fitted with various measurement instrumentation which were all connected to a data acquisition system. Those from which measurement data was used in the present research included soil pressure cells built into the arch extrados, to measure pressures acting normal to the arch from the fill and displacement gauges (LVDT) on the arch intrados, abutments and chamber walls. Preparation and setup of this instrumentation is described in section #.

2.4.1 Abutments design and construction

The overall objective of the physical model in the present research, to seek a compromise between investigating realistic behaviour while limiting the complexity to enable study of the fundamental two dimensional behaviour of the system, is reflected in the design of the abutments to simulate:

i. The case of insubstantial abutments as frequently found in field inspections, i.e. with dimensions comparable to the thickness of the arch.
ii. To investigate the role of abutment displacements on the failure mechanism of the arch-fill system.
iii. To limit the behaviour of the abutment to rigid body horizontal displacement and/or rotation and to eliminate vertical settlement and internal material deformation such that material failure may only occur at mortar joints.

In line with the above objectives, the abutments were constructed of reinforced concrete in two parts, lower (base) and upper (skewback). The bases were fully fixed to the structural floor by means of a steel beams, fully fixed at either end to prevent bases from spreading relative to each other, lifting or rotating in any direction.

The skewbacks were only temporarily fixed to the bases by means of removable anchors which only remained in place prior to decentring, which is the removal of temporary supports when the arch-fill system is ready to be loaded. The skewbacks were connected to the bases by horizontal

mortar joints. These enabled failure of the joints which may include horizontal translation or rotation of the skewbacks. The dimensions and construction details are shown in Figure #. Figures # and # are photographs of the abutments and associated fixtures.

2.4.2 Arch design and construction

The majority of brickwork masonry arch bridges are multi-ringed and multi-span. These, among many other aspects of masonry construction and configuration such as the role spandrel walls and three-dimensional mechanisms, have all been studied to some degree and as discussed in section # all of these aspects are influential and therefore should be incorporated into models for assessment of masonry arch bridges. A model that accounts for all of these complexities should therefore be the ultimate aim of the present line of research.

However, a common area to which attention is required is that of soil-arch interaction in masonry arch bridges and many important questions remain unanswered in this area with respect single-span, two-dimensional arch-fill systems before introducing further complexities such as the role of spandrel walls and three-dimensional behaviour.

Prior to test series EP0, full scale bridges incorporating fill that have been tested have been field bridges which are generally multi-ring, multi-span, with various hidden features such as backing, heterogeneous fill with contrasting strata, varying in defect types and states of deterioration. Tests on full-scale laboratory models have been conducted which have incorporated homogeneous fill but have also been either multi-span, multi-ring with spandrel walls.

The complexity of three-dimensional behaviour and the large number of geometric and/or material parameters that may contribute significantly to the overall capacity, made it difficult to identify with clarity the respective roles of individual elements in a repeatable manner. Harvey () made a number of observations in this regard with respect to the TRL series of load tests to collapse (). The most notable large scale laboratory tests incorporating fill were those carried out by Melbourne et al () which were three-dimensional, multi-span, multi-ring and had spandrel walls. Some of the many questions that arise due to these complexities are also listed below#.

What is the relationship between of the following attributes and their contribution to the overall capacity of the bridge?

- Spandrel wall
  - Brickwork pattern or configuration
  - Thickness profile with depth
  - Lateral deflection/strain response with respect to vertical load/lateral stress profile
  - Lateral stability
  - Frictional resistance to deformation/flow of the fill
- Multi-span
  - Relationship between horizontal thrust and stability of piers
  - Resistance to sway of intermediate piers provided by adjacent arches
  - Propagation of horizontal thrust and deflection over multiple spans
- Multi-ring
  - Location of centres of rotation of multi-ringed hinges
  - Location of centres of pressure at multi-ringed hinges
  - Moment resistance of multi-ringed hinges
  - Energy dissipated by inter-ring sliding throughout segments between hinges
  - Buckling of individual rings and restraint from the fill and adjacent rings

An in-depth study with high quality data and that can be dependent on a smaller number of geometric and material parameters and tied in with numerical modelling as well as theoretical modelling studies, required a strategic reduction in complexity in order to make meaningful

progress in this area. Once fundamental behaviour is more thoroughly understood, the aforementioned complexities may be introduced one at a time as separate subsequent studies.

The physical model used in the present research has therefore adopted particular features that are designed to provide a compromise between realistic behaviour and simplicity in order to obtain reliable data that may contribute to clear information about the behaviour of the system being modelled albeit limited in complexity. This is with the hope that improved understanding of a simplified model, may enable introduction of complexities in a controlled and well informed manner in subsequent research endeavours. These features are described as follows:

2.4.3 Masonry construction

Single span

The transmission of forces and displacements from one span to another is not studied directly in the present research. Since these forces and displacements depend on the interaction of individual arches with the loads above them, there would be no real benefit in understanding the interaction between adjacent arches until the transmission of loads by a single arch span to the thrust at the springings is better understood. Therefore the focus of the present research has been on an individual arch span and it's interaction with applied loads, the fill, and the abutments.

Shallow abutments with horizontal movement joints

A wide variety of abutment geometries and construction types exist in the field. These interact with the adjacent earth or structure in various ways depending on site conditions. In most cases, the displacement of abutments is primarily horizontal rather than vertical. A survey carried out by Essex county council () revealed that a large proportion of these were non-substantial, i.e. of width not much greater than the thickness of the arch. For these reasons as well as due to the need to carry out controlled tests within a laboratory environment the abutments were only slightly wider than the arch barrel. In order to enable the study of the effect of yielding supports, the abutments were constructed with a fixed base and an upper part, termed skewbacks, connected to the arch springing. A horizontal mortar joint forms the connection between the skewback and the fixed base. This is designed to distinguish between two possible modes of

failure at the abutment. The abutment may either slide along the horizontal joint or overturn about an edge of contact with the fixed base. Although this does not prevent these two modes from existing simultaneously, the additional cohesion provided by the mortar joint is designed to encourage one mode to occur distinctly from the other.

Header-bonded masonry construction

This prevents deformation of the arch cross section such that arch behaviour is equivalent to a single ring or voussoir arch. In multi-ringed construction (Figure 2.5c) there is a continuous mortar surface between rings from one springing to the next. The header-bonded configuration eliminates this so that it is not possible for shear failure or loss of cohesion to occur over more that than one course by mortar failure only. In order for a crack to propagate tangentially to the arch through more than one course in header bonded construction, it would be necessary for the bricks themselves to fracture which would be the same case for a single ringed arch. Thus the header bonded construction enables single-ringed behaviour to be studied for thicker arches. This configuration also provides interlocking in the transverse direction, which prevents longitudinal shearing deformation of courses across the width of the bridge. Thus header bonded arch of thickness of one stretcher (Figure 2.5a), would model the rigid voussoir arch better than an arch of the same thickness constructed of all bed jointed bricks. The arch was constructed to the dimensions in Figure 2.7.

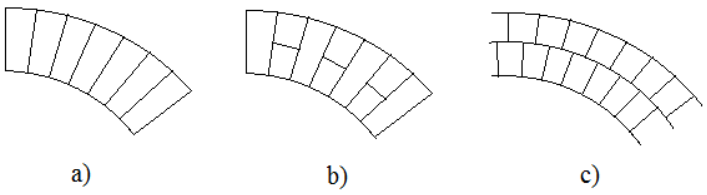

Figure 2.5 – a) Single-ring voussoir arch. b) Header-bonded construction. c) Multi-ring arch

2.4.4 Fill Material

Cohesionless fill, low moisture content

Although the test carried out as part of the test program were also carried out with a cohesive clay fill, the present research has focussed on the behaviour of an arch-fill system which is purely frictional and cohesionless. Part of the reason for this was the difficulty in compacting the clay to achieve a homogeneous medium within the apparatus. Another difficulty was the highly nonlinear behaviour and compressibility of the clay well before the ultimate load was reached. Another reason the tests on clay were not studied was that his would have greatly expanded the theoretical scope of the research while very little by way of theoretical modelling of the arch-fill interaction in masonry arch bridges has been established to date. It was therefore considered prudent to seek theoretical advancements in the area of cohesionless fill with the hope that this could provided a bases for extension to cohesive clays and possibly generalised to $c - \phi'$ soils in subsequent research endeavours.

Uniformly compacted, Homogeneous

To enable straight forward analysis of the relationship between the applied loads at the surface of the fill and the pressures occurring at the arch extrados, substantial investment was made in to achieving a medium that was as uniform as possible after compaction with a fill material that was not unrealistic. MOT type 1 crushed limestone used. This was a course grained angular fill, quantitative details obtained from laboratory testing on this fill are described in section #. This was placed in 120mm thick layers and compacted using a 10.5 kN compaction plate to a unit weight of 2.0 kN/m^3. The material was placed within the apparatus using a hopper that contained the required mass for the intended layer thickness after compaction. Sensitive areas where there was risk damage to the apparatus or masonry were compacted manually using a hand rammer.

2.4.5 Boundary conditions

In order to meaningfully study the two dimensional behaviour of the arch-fill system, it was necessary to confine the system to plane strain conditions. This was achieved by means of very stiff structural steel panels forming two longitudinal walls and two end walls. These were formed of a series on closely spaced structural steel beams vertically arranged to form that longitudinal wall panels. Spanning each of these beams were 50mm thick acrylic slabs, forming a continuous plane, lining the steel frame to form the inside surface of one side the test chamber. The other side was lined with 50mm plywood slabs with 4mm acrylic sheet over it, forming another smooth plane. In order to achieve plane strain conditions as far as possible, the stiffness of the chamber was maximised and the traction in the longitudinal plane was sought to be minimised. To minimise traction, these inside faces were further treated by application of a thin layer of a silicone based sealant upon which a 0.33 mm latex sheet was placed. For normal stresses >10 kPa, it has been reported that this treatment gives interface friction angles of <2° (Fang et al., 2004)

The length of the chamber was designed to accommodate foreseeable failure mechanisms within the fill. On the side at which the load is applied the end panel is not a very far from the arch, however the far side, the end panel is placed much further. This is based on the expectation that the loaded side of the ach would exhibit a mechanism between the point of application of the load and the arch barrel. The only influent the adjacent soil was expected to have on this area of the stress filed, was the confinement of the compressive stresses between the applied load and the arch. On far side however, from mechanisms observed in other tests with arch fill, such as the small scale tests carried out at Sheffield University () , a more far reaching failure mechanism was expected, resembling the passive failure zone of an earth retaining wall. The upper boundary is simply a free, horizontal surface. The space between the two longitudinal walls is uniform as shown in the diagram at approximately 1m. The lower boundary of arch-fill system is formed of the concrete structural strong floor of the heavy structures laboratory, which may be assumes not to undergo unnoticeable deflection relative to the displacements measured within the ach-fill system at any point during the load tests.

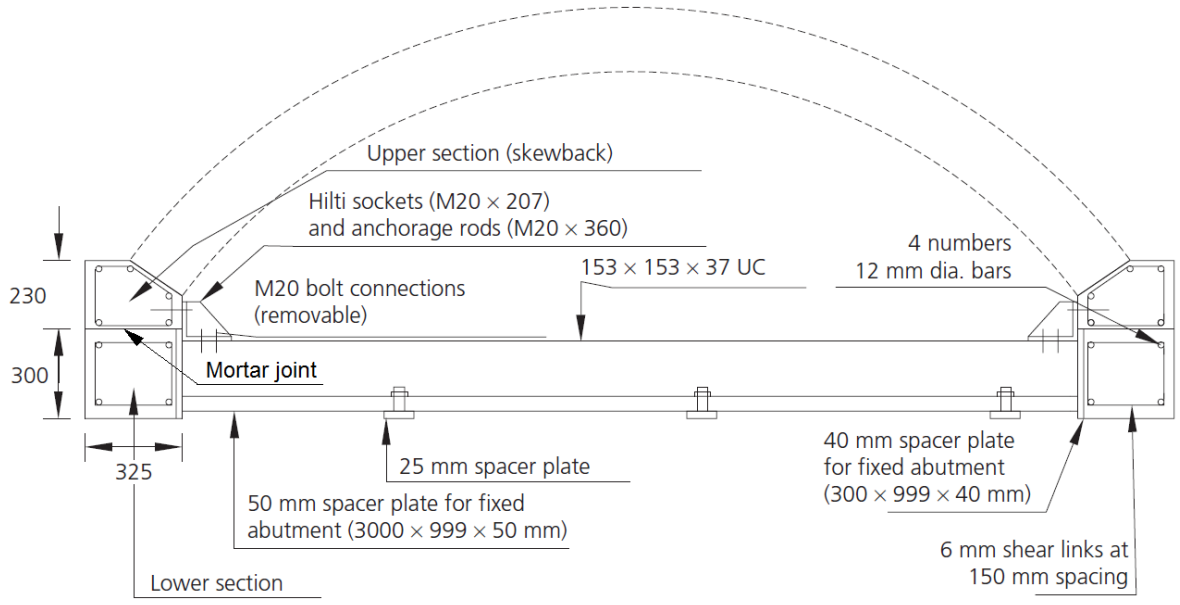

Figure 2.6 – Geometry, arrangement and construction of the abutments and arch

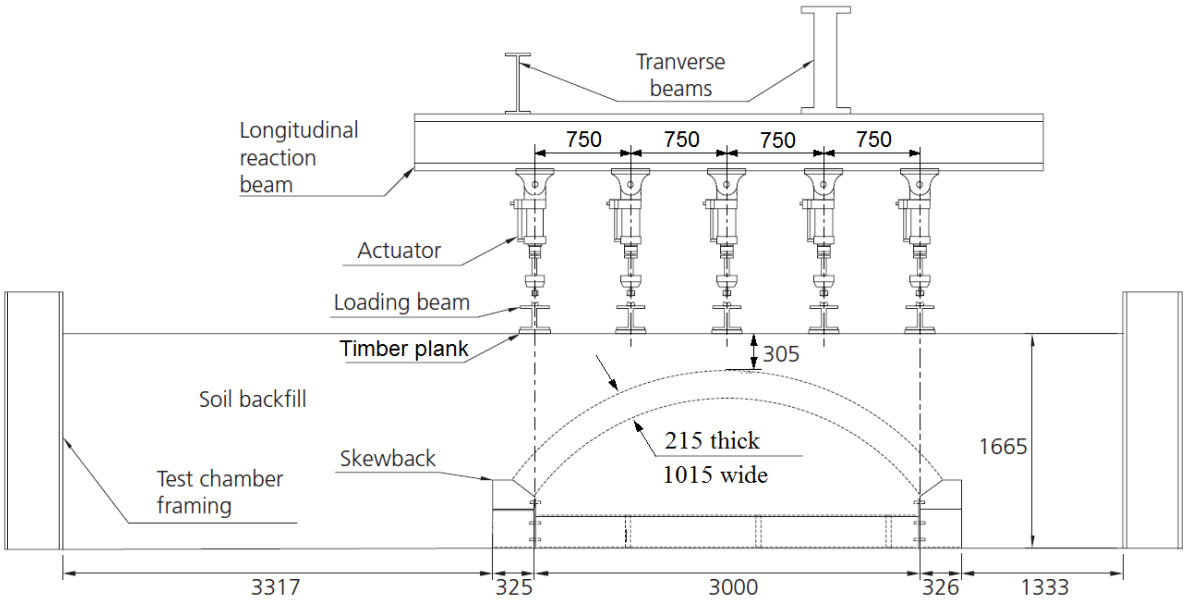

Figure 2.7 – Longitudinal cross section of the arch fill system within the test chamber, showing loading actuator arrangement and supporting structural elements

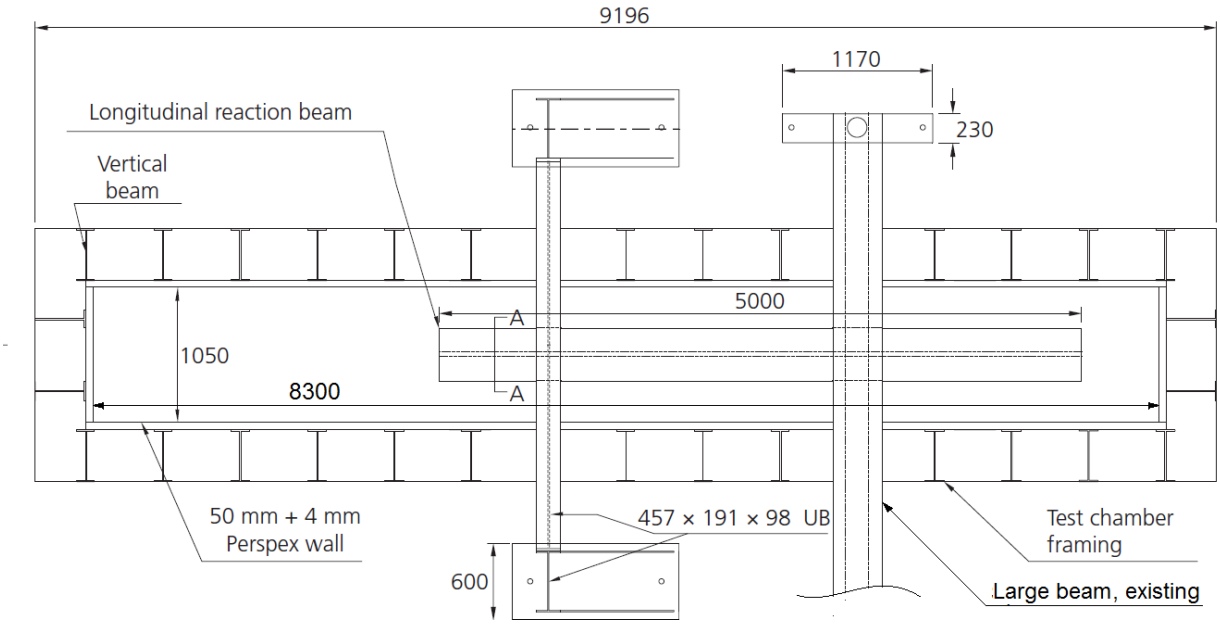

Figure 2.8 – Plan of structural apparatus including elements forming the test chamber and reaction beams to support applied load from actuators by transmission to the structural floor

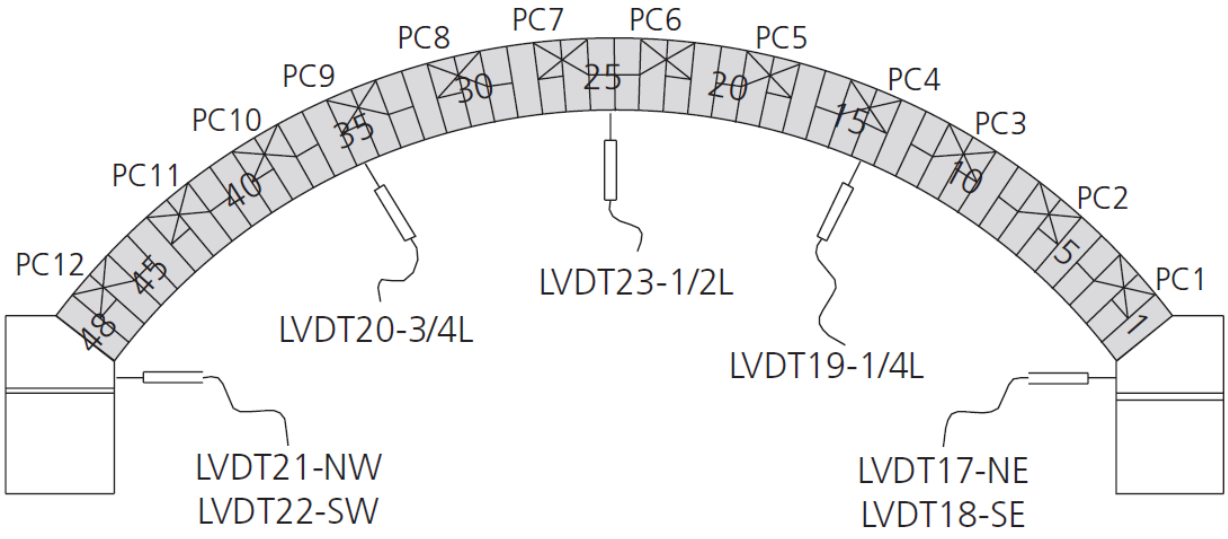

Figure 2.9 – Arrangement of pressure cells (PC) and displacement transducers (LVDT)

Figure 2.10 – Concrete abutments showing skewback with horizontal mortar joint and tie beam

Figure 2.11 – Fixture of tie beam to lower abutment and removable upper restraint to skewback

Figure 2.12 – Brickwork configuration and construction sequence

Figure 2.13 – Arch near completion with recesses to accommodate soil pressure cells

Figure 2.14 – Completed brickwork arch before fixing chamber wall into position

Figure 2.15 – Transparent Perspex slabs forming stiff, smooth plane lining of chamber, steels ties for lateral restraint of chamber walls visible on floor

Figure 2.16 – Fill material, main fill MOT type 1 limestone (left) and course fill for PIV (bottom)

Figure 2.17 – Fill placement in progress, course fill coloured with ash placed in front of windows, pressure cells covered with sand, greased latex lining on Perspex slab walls

Figure 2.18 – View of compacted layers of fill through chamber windows during placement

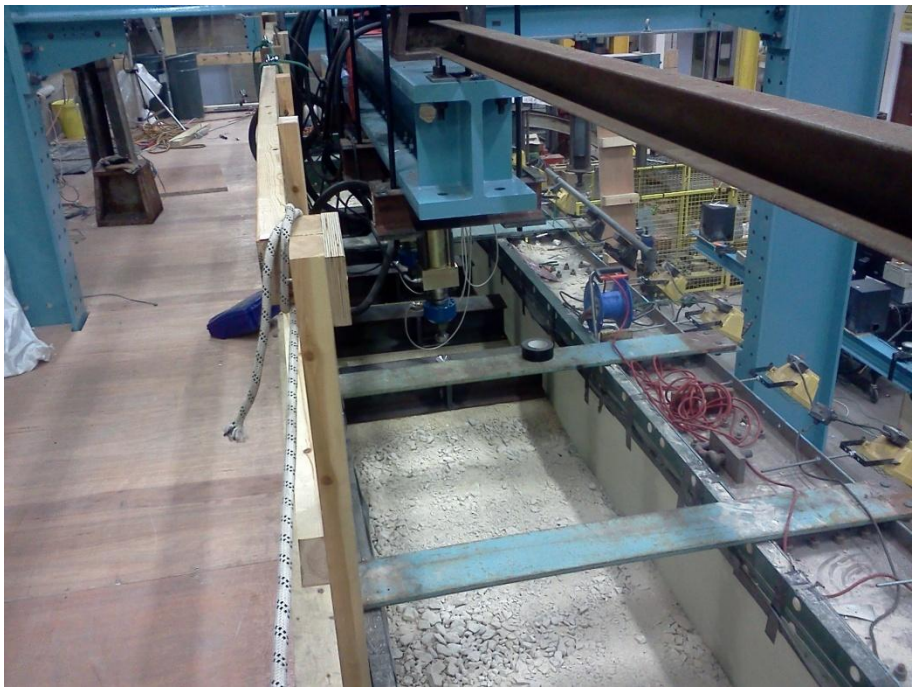

Figure 2.19 – Final Fill level, top level lateral ties visible, longitudinal reaction beam with actuators attached

Figure 2.20 – Loading arrangement showing bearing points between actuator heads and steel sleepers, timber interfacing steels to fill surface.

Figure 2.21 – Arrangement of LVDT displacement gauges on arch intrados

Figure 2.22 – LVDT displacement gauges positioned on skewback and soil pressure cell data cables passing through arch intrados to data acquisition system

Figure 2.23 – General perspective of apparatus (left), rig supporting camera array (centre), control and data acquisition terminals (right)

Figure 2.24 – South west perspective of main fill and arch after EP1 after removal of south chamber wall

Figure 2.25 - South east perspective of main fill and arch after EP1 after removal of south chamber wall

2.5 Materials Characterisation

2.5.1 Masonry

2.5.1.1 Strength

The type of bricks and mortar composition were informed by earlier tests on arch bridges such as Calloway 2007, Melbourne and Gilbert 1995, smith et al 204) with the aim of maintaining as much comparability as possible between tests.

Class A Engineering bricks were used and the mortar was mixed to a ratio of 1:2:9 – cement:lime:sand by volume. At the time of construction of the bridge, samples were prepared for strength tests. These were standard masonry prisms which were used to estimate the compressive and shear strength of the composite material. In addition to these, standard cube tests were carried on samples of the mortar mixture used in the bridge. Parameters obtained from these are given in Table 2.5. However, various workers such as (Brencich, et al., 2002), (Brencich & de Felice, 2009) have shown experimentally that the behaviour of masonry in compression when loaded eccentrically, as is the case in masonry arches, can have a significant impact on the strength which is particularly sensitive to the ductility of the mortar.

2.5.1.2 Stiffness

Continuous stress strain data was not obtained as part of the above tests, however experimental studies over a range of brick types and mortar mixes have been carried out in the literature. (Kaushik, et al., 2007) provided very comprehensive results on masonry in compression, including separate mortar tests, unit tests as well as prism tests. Similarly many authors such as those cited above have measured Elastic Moduli of masonry in compression and tension for a range of brick and mortar types. As the present research focuses on a rigid block modelling approach for ultimate stability analysis of the arch-fill system, a high value of stiffness is applied to the numerical model, given in Table 2.5. Although the theoretical model in the present research does not account for tensile stress, a range of tensile stiffnesses are tested in the numerical model to observe their influence on the system stability ant ultimate load bearing capacity

2.5.2 Fill Material

Particle Shape and Size Distribution

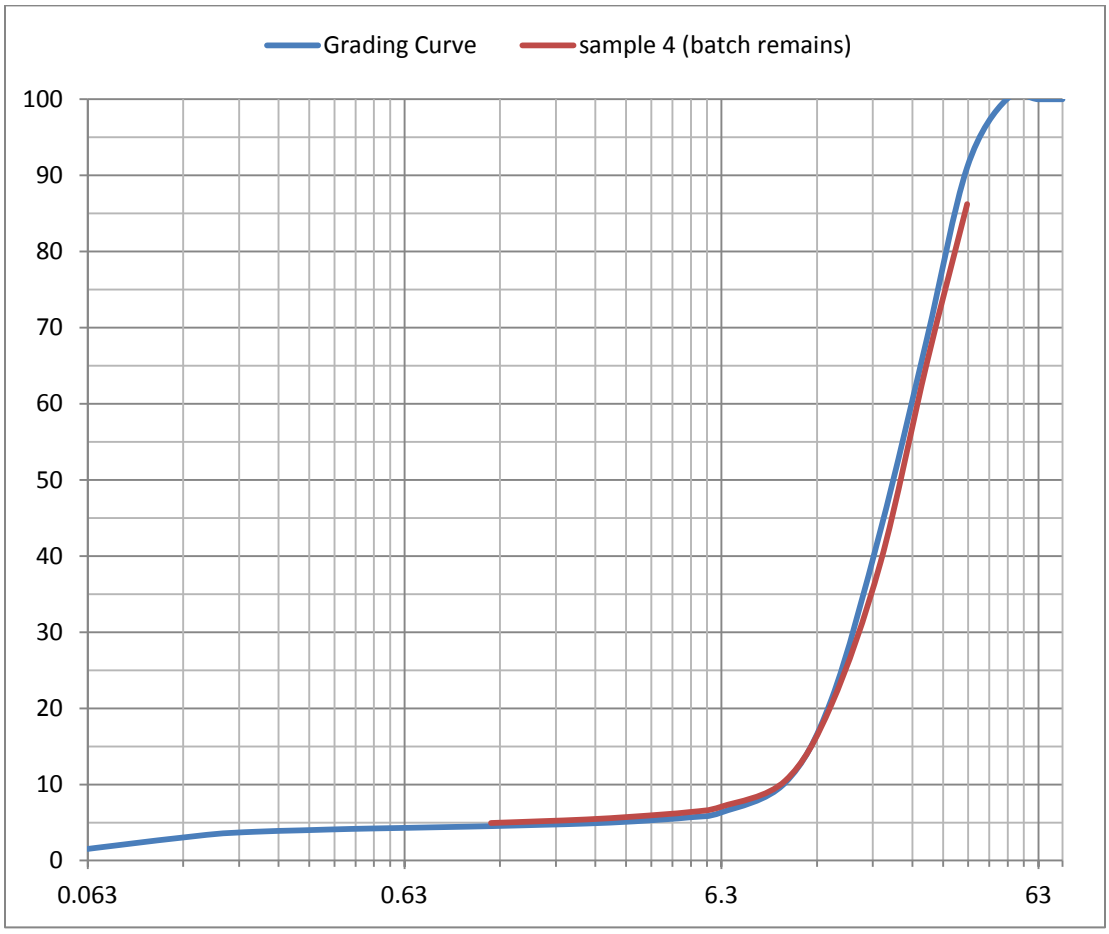

Figure 2.26 – Grading curve for the MOT type 1 crushed limestone fill used in the physical arch-fill system.

Table 2.1 – Particle Size Distribution Parameters for the MOT type 1 crushed limestone fill used in the physical arch-fill system.

			D10 10
			D30 17.5
CU	2.5	Uniformly graded	D50 22
CC	1.225		D60 25

Moisture Content

Samples of the fill material were regularly taken during the placement process at three samples per batch. These were prepared in the standard way, dried within a soils laboratory oven and weighed to determine the moisture content as given in Table 2.5

Direct Shear Box Test

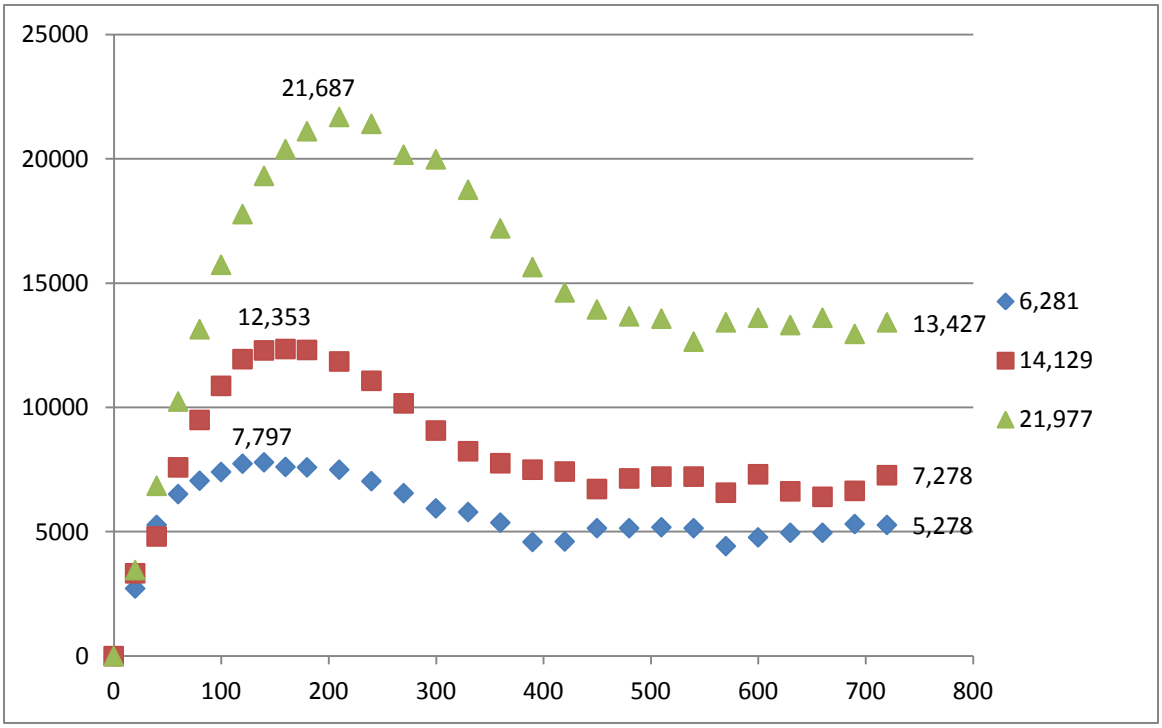

Figure 2.27 – Shear Stress plotted w.r.t. Time for the three tests at different normal stresses. Peak and Critical State values are labelled

Table 2.2 – Peak and Residual Shear Stresses for each Normal Stress

Normal Stess (Pa)	Shear Stress (Pa)	
	Peak	Residual
6,281	7,797	5,278
14,129	12,353	7,278
21,977	21,687	13,427

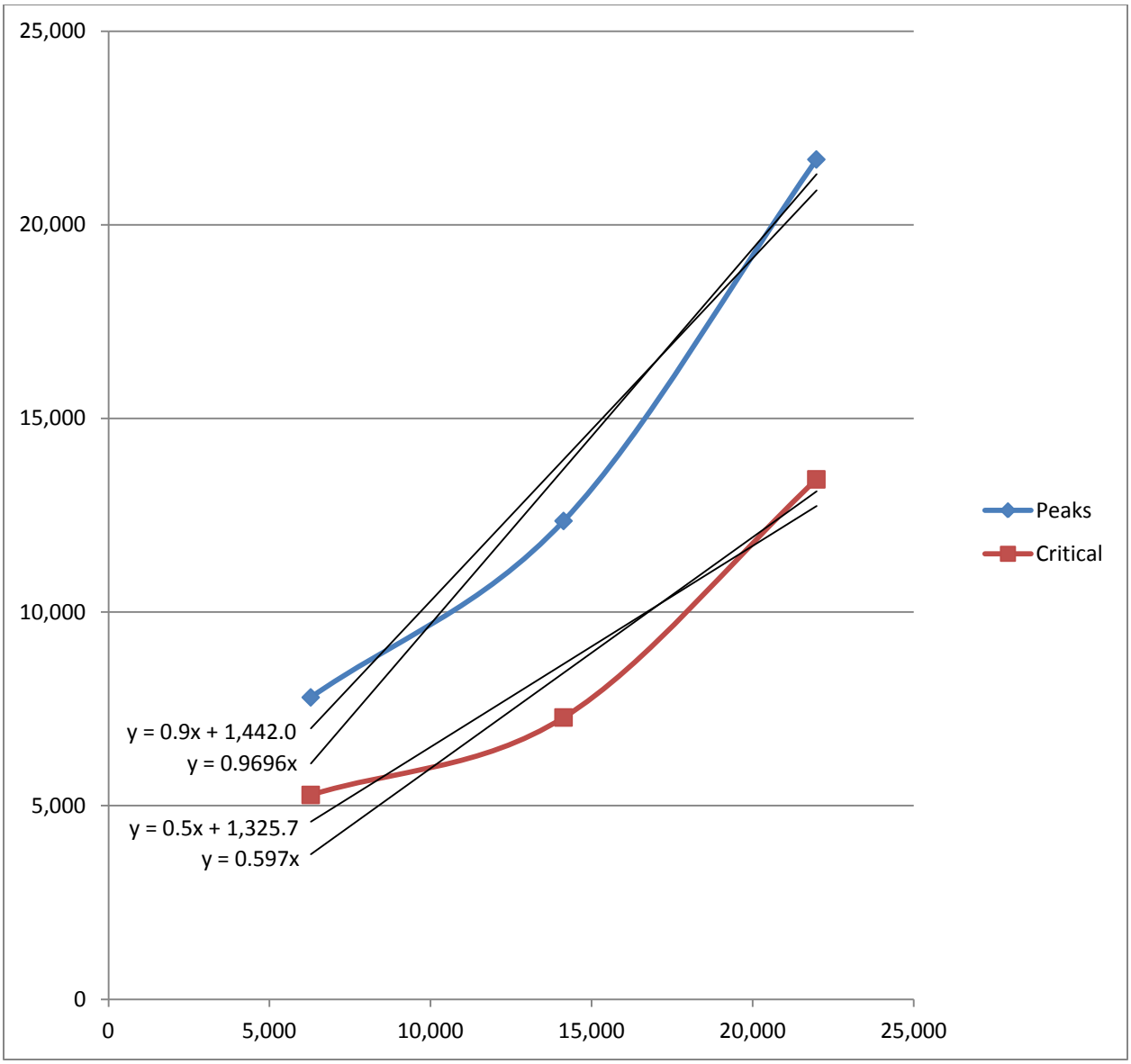

Figure 2.28 – Plot of Peak and Critical State shear stresses for the three normal stresses, showing linear regression for the two cases; with and without a zero-cohesion assumption

Table 2.3 – Showing effective angles of internal friction ϕ' derived from the direct shear tests for the peak and critical state cases

	Peak		Critical	
Cohesion (kPa)	0	1.44	0	1.33
ϕ' (degrees)	44.1	41.3	30.8	27.5

End Wall Test

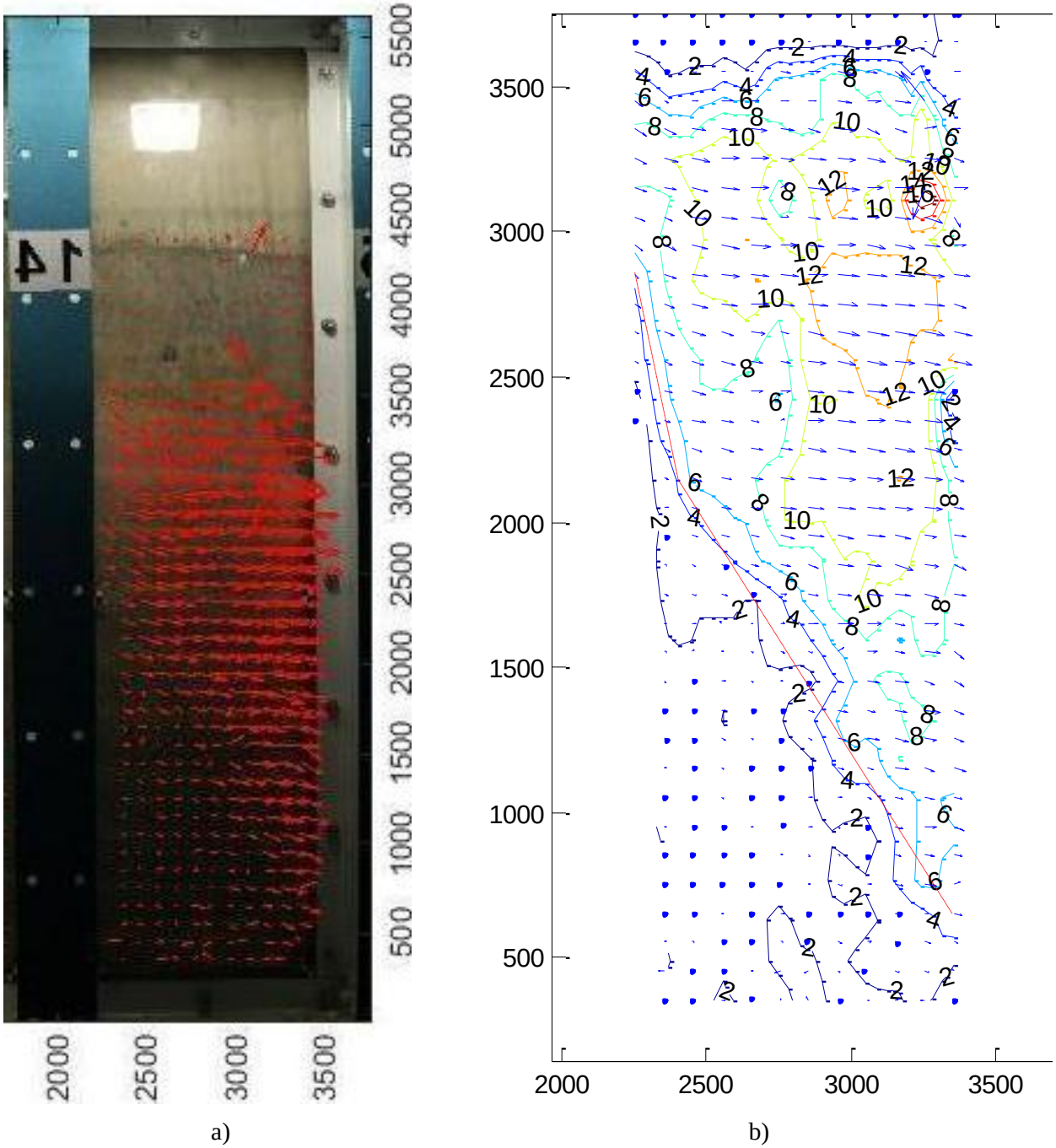

Figure 2.29 – Particle Image Velocimetry of the failure wedge formed by removal of the end wall and application of a surcharge to induce active failure.

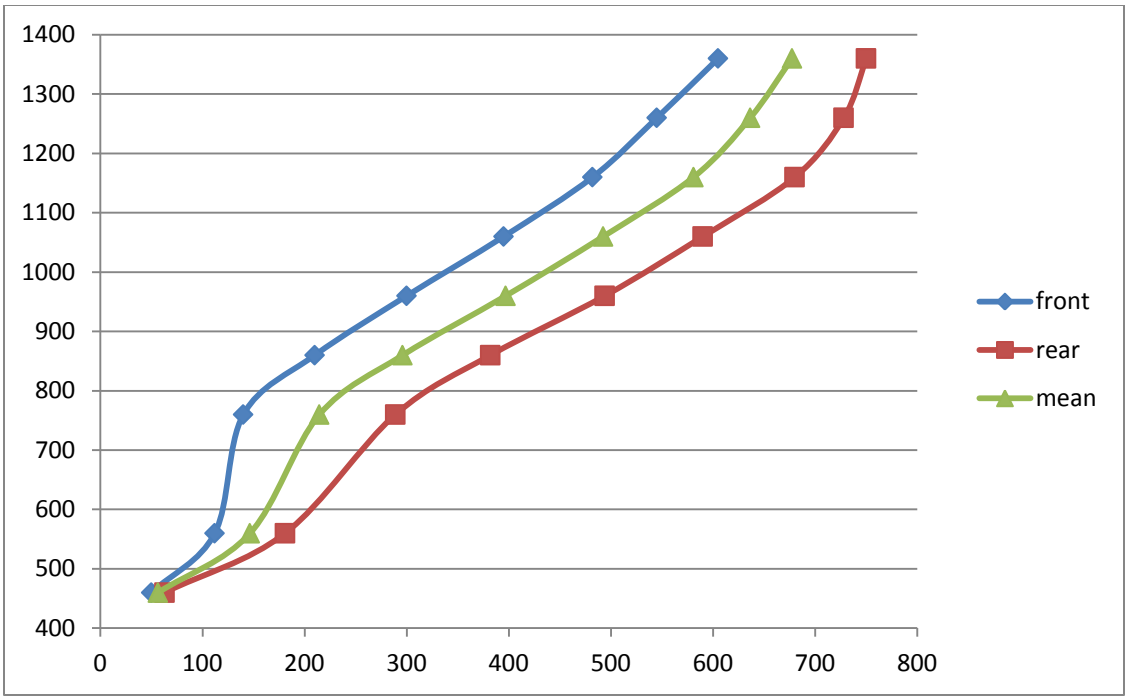

Figure 2.30 – Horizontal measurements taken of the resulting profile at a series of levels, after failure of the end wedge

Table 2.4 – Estimation of friction angle based on simple Mohr-Coulomb slip plane

	Distance From End Wall (mm)					
Height From Floor (mm)	Front Wall	Rear wall	mean	gradient	Slip angle θ (degrees) to the vertical	$\phi' = 2.(45 - \theta)$
1360	605	750	677.5			
1260	545	728	636.5	0.41	22.30	45.39
1160	482	680	581	0.48	25.77	38.46
1060	395	590	492.5	0.62	31.68	26.65
960	300	494	397	0.70	35.06	19.88
860	210	382	296	0.76	37.36	15.27
760	140	289	214.5	0.77	37.68	14.65
560	112	181	146.5	0.66	33.59	22.82
460	50	63	56.5	0.69	34.62	20.75

The apparently non-linear slip surface may be due to the applied load being positioned too far from the edge for a simple wedge to propagate to the vertical face. As a result, a more complex mechanism may have resulted, that minimises the work required for displacement to occur through to the vertical face. This problem may be treated in a similar way to that of bearing capacity of a shallow foundation near the edge of a slope, setting the slope angle to vertical.

However, the principal stresses in the locality of the applied load, near the surface may be assumed to be close to vertical. The bearing point, as described in Chapter 2, of the actuator on the steel sleeper is free to rotate. This minimises any traction component that may occur at the fill surface, thus increasing the likelihood that the principal stresses, as suggested, are approximately vertical in the locality of the applied load.

Therefore, a simple method of estimating the internal angle of friction may be to assume that the angle of slip at the upper level of the mechanism is as predicted by the Mohr-coulomb failure criterion, i.e. $\theta = 45 - \frac{\phi'}{2}$, giving: $\phi' = 2.(45 - \theta)$. This formula is evaluated throughout the slip plane in Table 2.4. From the slip angle nearest to the fill surface, we may estimate $\phi' \approx 45°$

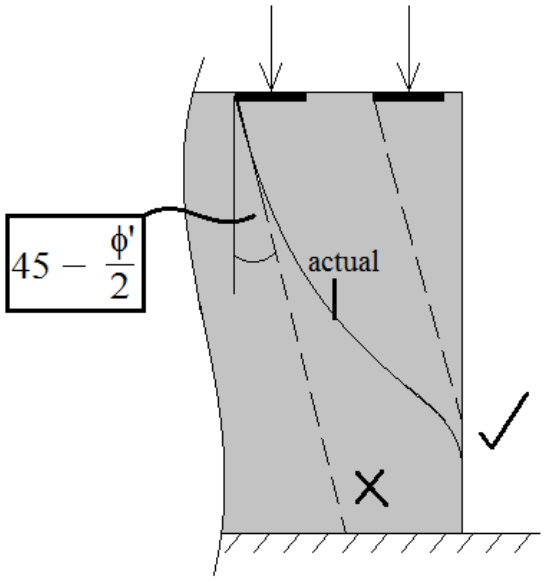

Figure 2.31 – Illustrating a possible explanation for the apparently nonlinear failure surface and suggested simple method of estimation of ϕ' using near surface slip angle

Table 2.5 – Material properties used for modelling in the present research

Material	Property	Value	Unit
Bricks	Mean dimensions	214 x 102 x 65	mm
Bricks	Density	2226	Kg/m^3
Bricks	Compressive Strength	176	N/mm^2
Mortar	Density	1470 – 1570	Kg/m3
Mortar	Compressive Strength	1.3	N/mm^2
Masonry	Unit weight	20	kN/m^3
Fill	Unit weight	20	kN/m^3
Fill	internal friction	45°	degrees

2.6 Loading

For the purpose of the present research, the physical model is used to investigate the behaviour of the arch-fill system when subjected to a static load that is sufficiently large to destabilise the system. The behaviour leading to destabilisation, at the point of destabilisation of the system as the state beyond that point is strictly under the requirement that equilibrium holds. This means the loading applied to the system must be at a slow enough rate that any inertial component must be negligible. Furthermore, the numerical and theoretical analysis of the system pre- and post-peak load assumes either a statically stable state, or a state of plastic equilibrium, such that no acceleration of any part of the system is occurring, i.e. all velocities are of constant magnitude. In order to achieve this, displacement controlled loading was applied to the system.

Another objective of the present research is to study, under the above conditions, the general mechanism by which loss of stability occurs in arch-fill systems within masonry arch bridges. Of particular interest are the more onerous load cases. For this reason the loading patters applied to the system in the physical model are not symmetrical, since symmetrical loading results in a special case of symmetrical mechanism which only occurs when the loading pattern is precisely symmetrical and is of sufficient intensity to cause loss of stability. For all other load cases experienced by a bridge as a load is moved slowly across, two specific types of mechanism may occur as discussed in Chapters 2 and 3 which together cover what is considered the general case.

Another important aspect of the present research is the effect of concentration or distribution of loads applied to at the surface of the fill. In order to observe the effect of this, the large scale experimental apparatus has been setup for three different loading patterns. The loading patters are intended to simulate a railway type of loading. As such, load is applied at equally spaced strips of pressure across the width of the bridge, simulating railway sleepers, achieved by means of steel beams, place on top of 25mm thick timber planks at the fill surface. The aforementioned three loading configurations are:

i. A single sleeper load centred at ¼ span (Figure 2.32a)
ii. Three sleepers, again centred at ¼ span, with the other two centred above $1/8^{th}$ span and $3/8^{th}$ span either side of the central sleeper, i.e. equally spaced at $1/8^{th}$ span centres apart. (Figure 2.32c)
iii. Three sleepers, again centred at ¼ span, with the other two centred above mid-span and end span either side of the central sleeper, i.e. equally spaced at ¼ span centres apart. (Figure 2.32b)

The potential influence that prior loading of the bridge may have on the response of the bridge to the above loading regimes was also investigated in the present physical modelling programme by applying the above loading regimes under various circumstances:

EP1 PH1 – Prior to carrying out the static load test (i) above, the system was subjected to one million passes of a loading pattern that simulated 50kN axles crossing the bridge in one direction at a rate of 2 Hz continuously. This was achieved by loading and unloading a series of actuators sequentially so as to simulate the effect of the 50kN axle rolling smoothly from one sleeper to the next, crossing ht e bridge in 0.5s. The loading arrangement to achieve this is that shown in Figure 2.7

EP1 – PH2 – This was to investigate the effect on the load bearing capacity of the arch-fill system after it had been previously loaded to failure. This was intended to represent the residual or critical state capacity of the arch. After EP1 PH1 the system was subjected to a re-setting procedure in order to bring it back to a configuration close to the original. This was followed by a repeat of the static loading as was done in EP1. The re-setting procedure involved placing the

five sleepers in the same positions as used for the cyclic loading in EP1, and the applying a 50kN load to each position in turn, starting from the side furthest the applied load and sequentially moving across in order to reverse the displacement that had occurred during the previous test as far as possible. This was followed by a period of simulated service loading as described in EP1, however this was for 100,000 cycle s rather than 1000,000 cycles.

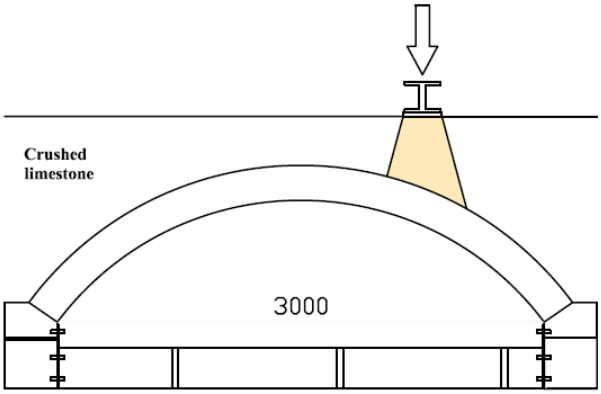

(a) EP1-PH1 & PH2

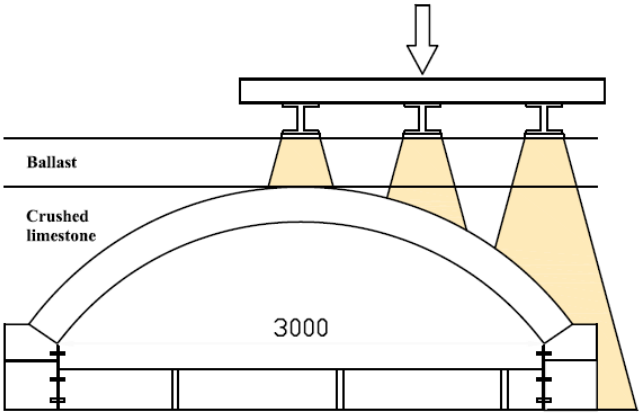

(b) EP3-PH1 & PH2

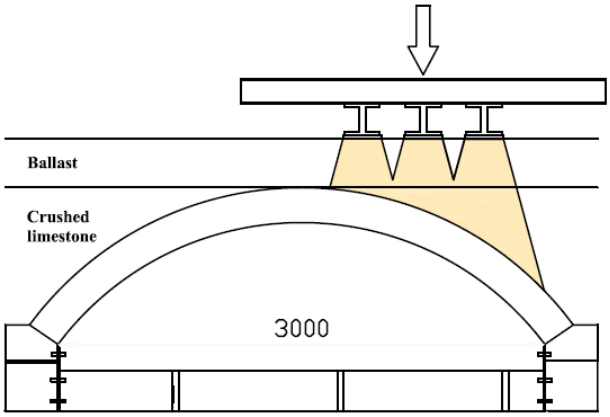

(c) EP3-PH3

Figure 2.32 – The three loading configurations tested on the physical model

EP2 – This was a repeat of the static loading described in EP1, but on a newly setup apparatus that had not undergone any simulated service loading.

EP3 PH1 – This was a repeat of the loading regime of EP1 PH1 Including the service loading, followed by static loading, only with the loading configuration (iii) described above. (Figure 2.32b)

EP3 PH2 – This was a repeat of the procedure described in EP1 PH2 including the arch re-setting procedure and 100,000 cycles of simulated service loading, only with configuration (iii).

EP3 PH 3 – This was a repeat of EP3 – PH2, only with the more closely spaced configuration (ii) described above. (Figure 2.32c)

The displacement controlled static loading regime in every case above, was applied at a rate of 10mm per hour. Details of the Loading apparatus are shown in Figure 2.7 and Figure 2.20.

2.7 Instrumentation

Load cells were positioned to measure loads applied by actuators and provided feedback to the control system in order to maintain displacement control.

LVDT Displacement gauges ere used to monitor the radial displacements at the arch intrados as well as the horizontal displacements of the skewback during the load tests.

12 equally spaced soil pressure cells were install within the arch extrados as shown in figure 2.5 in order to measure the pressure profile over the arch from the fill during the tests.

Numerous other LVDTS were used as well ass acoustic emissions gauges, however these not used directly in the present research. Details of all instrumentation including accuracy and calibration procedures carried out may be found in (Augusthus-Nelson et al 2017)

2.8 Load Test Results

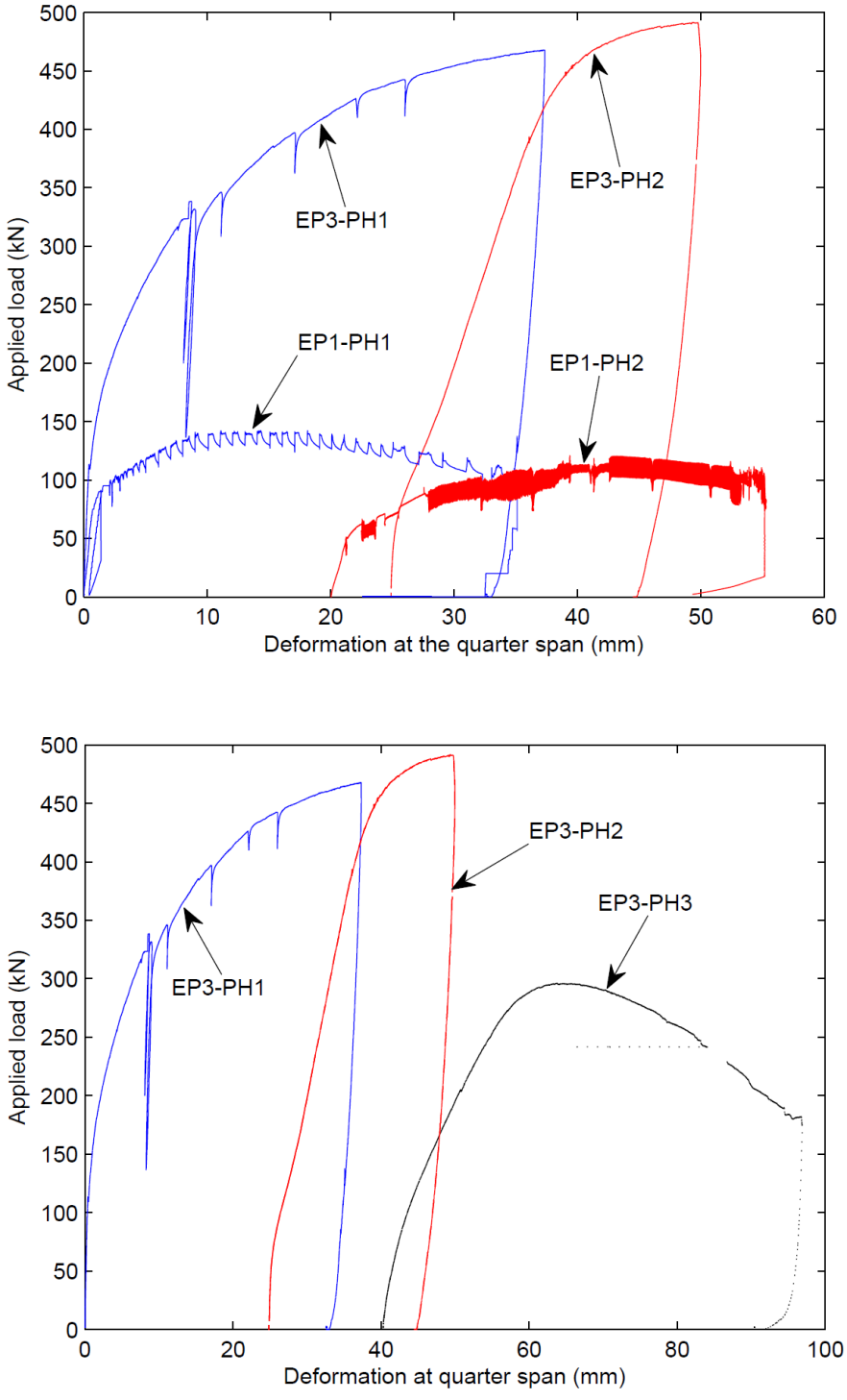

Figure 2.33 – Plots of applied load w.r.t. radial deflection at the quarter span LVDT

Chapter 3 Numerical Modelling

3.1 Background

3.1.1 Continuum Methods

The establishment of the finite element method in the late 1960s (e.g. Zienkiewicz and Cheung, 1967) as a numerical method for the approximate solution of boundary value continuum problems and its application to nonlinear problems in the early 1970s (e.g. Zienkiewicz, 1972) revolutionised the field of computational mechanics.

In the late 1970s the UK governing bodies concerned with transport infrastructure recognised the need for improved computational methods and more realistic models taking account of the influence of spandrel fill. This lead to a Transport Research Laboratory programme that set out to rectify shortcomings in the existing assessment approach based the MEXE method, through full scale and model testing as well as theoretical analysis. The analyses used non-linear finite element methods, linear elastic analysis and mechanism techniques closely related to those presented earlier.

Early attempts to use the finite element method for masonry arch analysis include Towler and Sawko (1982) and Towler (1985) who conducted a series of experiments on model brickwork arches and compared the results with their numerical solutions. Crisfield (1984) also developed a finite element model for the masonry arch. In this model as well as those of Towler and Sawko, no attempt was made to model the influence of the fill on the response of the arch. Crisfield (1985 a, b) found that a finite element model of a bare arch should give lower collapse loads than the mechanism method, which was not always the case in Towler's results. In subsequent work by Towler, Crisfield and Wills attempted to directly model the fill, such as the use if the Mohr-Coulomb yield criterion by Crisfield (1985a). The masonry in the above finite element studies, was modelled by a series of 1-D short prismatic beam elements, interconnected to form an arch. This was improved by Rauf (1984) who used curved beam elements.

In these 1-D elements, the possibility of an element having either an un-cracked or fully cracked cross section was included, depending on whether the hypothetical tension crack penetrated as far as midsection. Convergence of the solution to a stable configuration of cracked and un-cracked sections is achieved through an interactive procedure, using the Newton-Raphson method, with increments of load being applied to the arch. At each new load level, the nodes are examined for the existence of tensile stress, and if it exists, cracking is assumed over the tensile area. The associated tensile force is regarded as an 'unbalanced' force on the cross-section, and it is applied to the node in an iterative manner until eliminated (Choo et al 1991).

Crisfield (1985a) and Crisfield and Packham (1987) noticed the importance of properly modelling the influence of the fill such as lateral resistance, in their work with the mechanism method, which gave absurdly low collapse loads, particularly for low span to rise ratios when the positive influence of the fill was not considered.

Crisfield, Packham, and later, Wills (Crisfield and Wills 1986) attempted to model the lateral resistance of the fill, albeit indirectly, by introducing nonlinear springs near the springings into their models to simulate passive resistance.

Bridle and Hughes (1990) presented a program (referred to as the Cardiff Program) that uses Castigliano's second theorem to determine elastic stresses in an arch due to bending and compression only, eliminating tensile zones by limiting the effective depth of the cross section to the compression zone (Figure 3.1). Unlike Pippard's case, the computational implementation of this theorem enabled arbitrary geometrical, material and boundary settings to be given. The program used Castigliano's theorem to calculate forces and moments due to any arrangement of loads and allowed any arch shape to be chosen or specific geometric data to be entered.

However, A set of common limitations to methods of both Pippard and Bridle and Hughes stem from the conditions that must be fulfilled in order for Castigliano's second theorem to hold, namely; constant temperature, unyielding supports and linear elastic material response.

Furthermore this program also included strain energy due to axial load. Pippard ignored the axial thrust and shearing force terms in the strain energy equation. Wang et al (2010) showed that for relatively small span thick arches particularly those with large span to rise ratios, the error from excluding the axial strain energy becomes significant.

The solution procedure according to Bridle and Hughes description is outlined as follows:

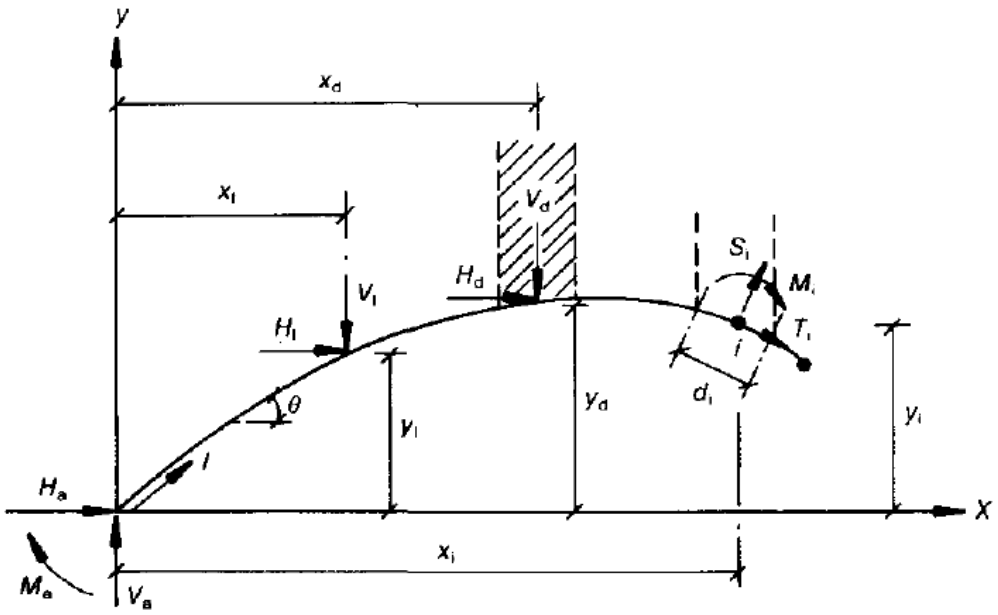

Figure 3.1: Definition of symbols in the Cardiff program: d_i= section depth at i, A_i section area at i,
I_i = second moment of area at i, l is the length of the arch measured from the left abutment (after Bridle and Hughes (1990))

Bridle and Hughes used the following discretised equation for strain energy due to moments and axial force:

$$U = \int_0^L \frac{M_i^2}{2EI_i}\delta l_i + \int_0^L \frac{T_i^2}{2EA_i}\delta l_i$$

It is not clear from Bridle and Hughes whether these displacements are known and whether, like in Pippard's analysis, they are presumed to be zero. They then appear to make use of the second moment area theorem to obtain displacements from these forces as follows:

$$\delta_{xp} = \int_0^L \frac{M_i(y_p - y)\delta l_i}{EI_i} - \int_0^L \frac{T_i^2 \cos\theta\, \delta l_i}{EA_i}$$

$$\delta_{yp} = \int_0^L \frac{M_i(X_p - x)\delta l_i}{EI_i} - \int_0^L \frac{T_i^2 \sin\theta\, \delta l_i}{EA_i}$$

The integrals were evaluated at each load increment where new forces and moments were calculated. At every load increment an incremental thinning procedure was implemented so that only the depth of the section that was in compression remained. Bridle and Hughes implemented this algorithm for the case of Bridgemill arch in Girvan. This arch was loaded to failure in 1984 (Hendry et al 1985) as part of the TRL program and had thus been the subject to analysis in several preceding publications. In particular that of Crisfield (1985a) who analysed Bridgemill arch using a 2-D finite element model as well as his mechanism program. Bridle and Hughes thus used the same basic data used in Crisfield's studies to setup their Cardiff Program, with no horizontal soil pressures. The load verses deflection curve at the position of the applied live load for the 40 element solution was plotted together with those of Crisfield's 2D continuum finite element model and his mechanism program for the same test case (Figure 3.10).

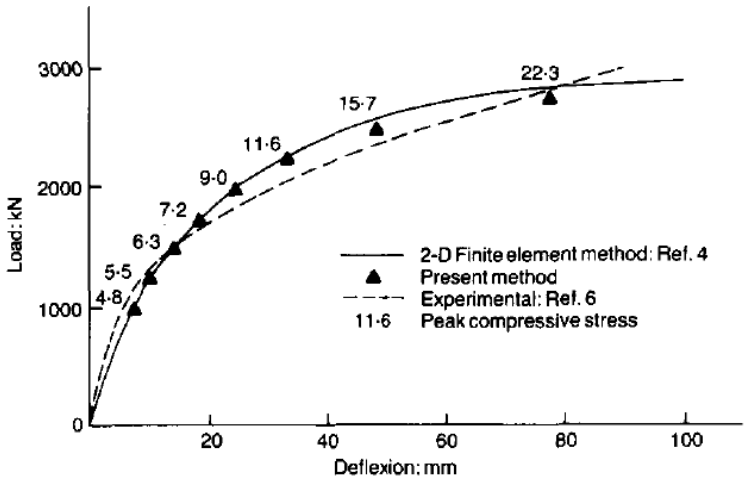

Figure 3.2 – Load verses deflection plots for the Cardiff program compared with Crisfield's results and the physical test data

To illustrate the effect of thinning the arch cross section, the effective arch thickness variation throughout the arch, obtained by the Cardiff Program was plotted at a load of 2250 kN applied at the left hand quarter span position (Figure 3.3). The un-shaded region represents the effective section remaining after thinning.

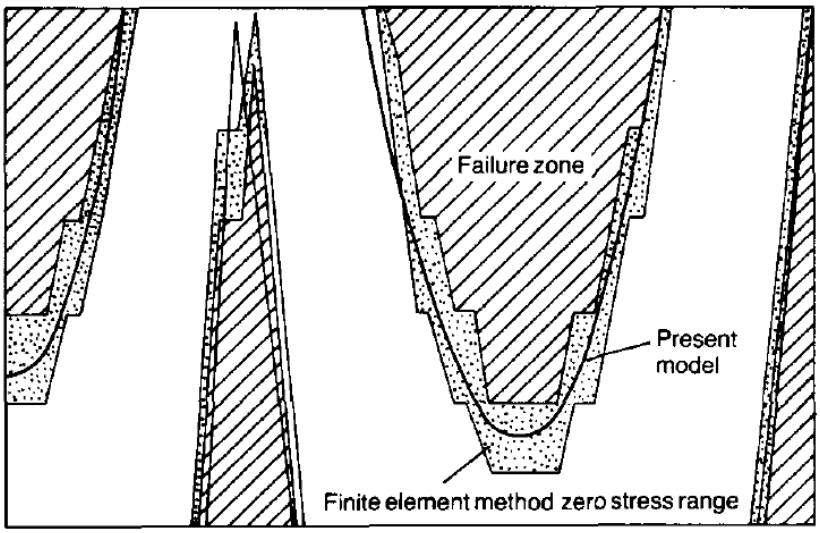

Figure 3.3: Effective arch profile resulting from the Cardiff program and qualitative comparison with 1-D finite element results (after Bridle and Hughes, 1990)

Also included in the plot is a range of results obtained from Crisfield's finite element model with geometrical nonlinearity and linear elastic material, to be consistent with the limitations of the Cardiff Program. Both results were obtained by assuming a 1 : 2 (horizontal : vertical) distribution of live load through the fill. The dotted regions in Figure 3.3 represent a range of neutral axis positions obtained by the finite element method to demonstrate the similar detail provided by both methods. The hatched regions represent tensile or cracked parts of the arch cross section, which are indicative of potential hinge positions.

Choo et al, (1991) formulated a 2-D, straight, tapered beam element (Figure 3.4, detail A) that enables exclusion of tensile material to a similar effect to the thinning procedure of Bridle and Hughes;

> "...as nodal cracks develop, the tension zone of each element is assumed to be ineffective and is neglected." (Choo et al, 1991)

These elements were strung together in the same manner as in the aforementioned 1-D element models. The tapered, 2D element enables the effective arch thickness to vary linearly across the element, resulting in a continuous variation of the effective arch as opposed to the binary variation in the 1-D elements seen earlier.

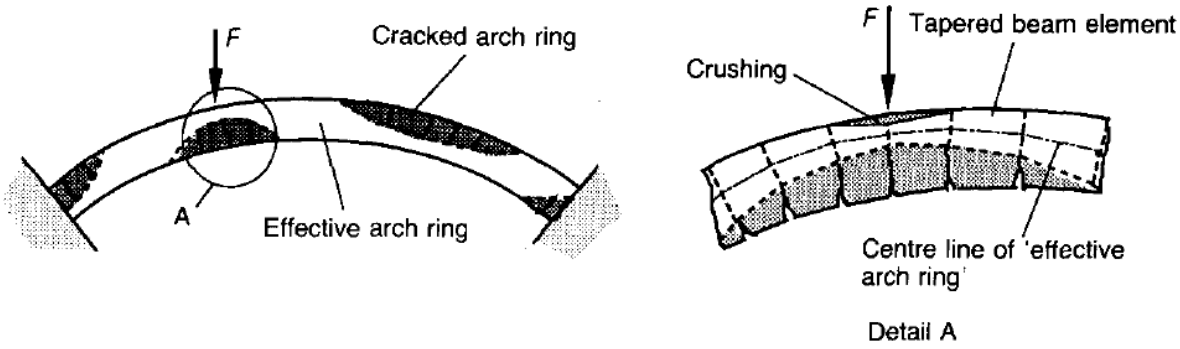

Figure 3.4: Effective arch ring from the 2-D nonlinear finite element model (after Choo et al, 1991)

Furthermore this element was also governed by a bilinear elastic, perfectly plastic material model (Figure 3.5) to enable representation of yielding of material in compression or crushing of masonry (Figure 3.4, detail A).

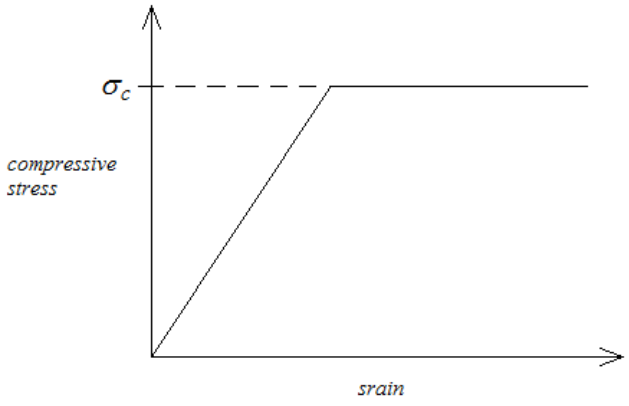

Figure 3.5: Assumed constitutive model in the 2-D nonlinear finite element model (after Choo et al, 1991)

The resulting effective depth was calculated at each nodal cross-section by satisfying equilibrium between the axial force P, the bending moment M and the internal stresses for the general case as shown in Figure 3.6

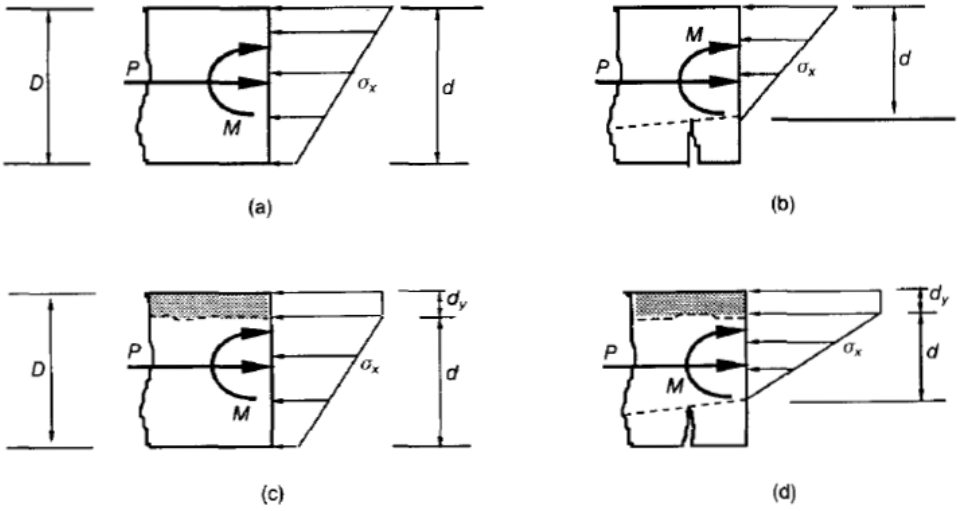

Figure 3.6: Effective section depth configurations corresponding to various internal stress cases
(after Choo et al, 1991)

Like Bridle and Hughes, Choo et al used an iterative solution procedure which showed good convergence characteristics. In addition, the required iterative procedure for achieving a solution is more straight-forward in that there is no need to consider unbalanced forces.

The purpose of the iterative procedure however, is essentially the same, namely, to repeatedly adjust the effective cross section until it converges to a stable configuration. Generally, the finite element method does not require iteration to obtain a solution; it solves a global boundary value problem by matrix inversion, to give a discretised approximation to the continuum stress field for the arch. Since the determination of the effective cross section is a function of the stress field throughout the arch and vice versa, the finite element method and the effective cross section algorithm are coupled processes, which need to be solved with mutual feedback, hence the iterative procedure:

$$[\mathbf{K}(d)]_i\{\delta\}_i = \{\Delta P\}_j$$

$$\{d\}_{i+1} = S\{\delta\}_i$$

Until $$\|\{d\}_{i+1} - \{d\}_i\| \leq \varepsilon$$

Where ε was a specified tolerance for convergence and $\{\delta\}_i$ was the global displacement vector, assembled from element displacement vectors $\{\delta\}_e$ given by:

$$\{\delta\}_e = [u_i \quad w_i \quad \theta_i \quad u_j \quad w_j \quad \theta_j]^T$$

From

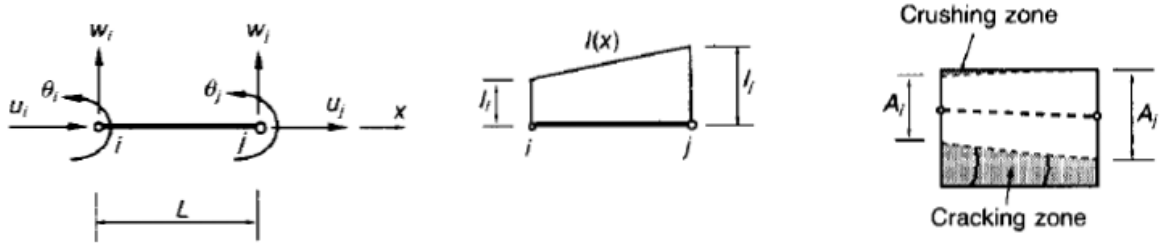

Figure 3.7: Tapered element formulation showing degrees of freedom and section variables (after Choo et al, 1991)

Where I_i and I_j are the second moments of area at nodes i and j respectively. And the cross sectional area of the element was assumed to be

$$A_e = \frac{A_i + A_j}{2}$$

K is the global stiffness matrix, dependant of the effective depth distribution, d, and is assembled from the element stiffness matrices $\mathbf{K}_\mathrm{e}$ given by:

$$\mathbf{K}_\mathrm{e} = \int_0^L [\mathbf{B}_\mathrm{w}]^\mathrm{T} EI(x)\mathbf{B}_\mathrm{w}\, dx + \int_0^L [\mathbf{B}_\mathrm{u}]^\mathrm{T} EA\mathbf{B}_\mathrm{u}\, dx$$

Where

$$\mathbf{B}_{\mathrm{w}} = \frac{d^2}{dx^2}\mathbf{N}_{\mathrm{w}} \qquad \text{and} \qquad \mathbf{B}_{\mathrm{u}} = \frac{d}{dx}\mathbf{N}_{\mathrm{u}}$$

$\mathbf{N}_{\mathrm{w}}$ and $\mathbf{N}_{\mathrm{u}}$ are shape functions that interpolate nodal values of lateral (w) and axial (u) displacements respectively, such that:

$$w = \mathbf{N}_{\mathrm{w}}\{\delta\}_e$$

and

$$u = \mathbf{N}_{\mathrm{u}}\{\delta\}_e$$

A detailed general introduction to the Finite Element Method is available in for example Chandrupatla and Belegundu (2002). Similar finite element models for masonry arches excluding tension have since been developed, for example the 1D Castigliano based model by Brencich et al (2001).

Choo et al provided an improvement on the linear load dispersal model of Bridle and Hughes by using a Boussinesq pressure distribution for the dispersal of a strip load at the fill surface to the arch extrados (Figure 3.8). Although the Boussinesq equation **Error! Reference source not found.** was derived on the basis of a uniform infinite half space, it is hypothesised to be a step forward in the realistic modelling of vertical soil pressures.

$$\sigma_y = \frac{p}{\pi}\left[\beta_2 - \beta_1 + \frac{1}{2}(sin2\beta_2 - sin2\beta_1)\right]$$

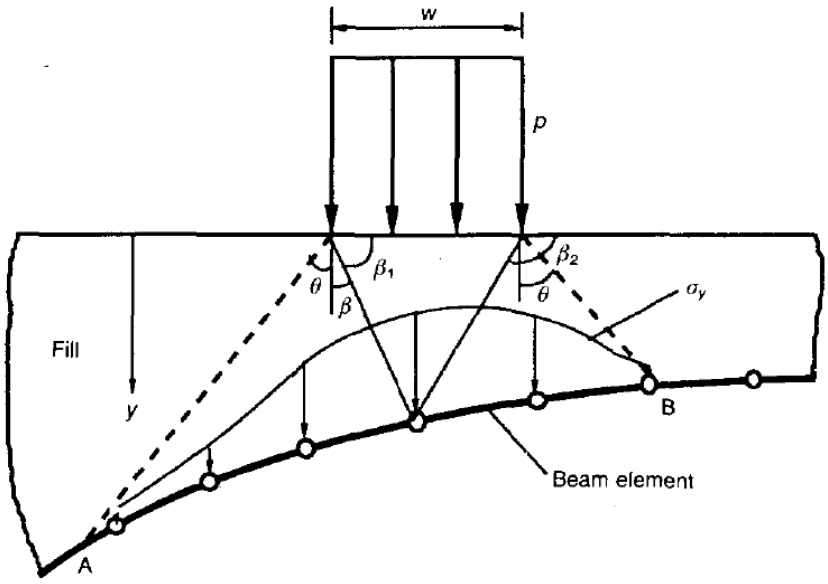

Figure 3.8: Boussinesq pressure distribution from an imposed uniform strip as it coincides with the arch
(after Choo et al, 1991)

3.1.2 Discontinuum Methods

Discontinuum numerical methods compute the mechanical behaviour of an assemblage of bodies by modelling their mutual interaction at interfaces as a system subject to external forces and kinematic boundary conditions applied to individual bodies. Thus there are two aspects of a Discontinuum based numerical model:

i) the behaviour of interfaces.
ii) the behaviour of the material of individual bodies.

There are generally two classes of Discontinuum method based on the way contacts are treated.

i) The soft contact approach, where a finite stiffness is attributed to the points of contact which are allowed to displace accordingly, including overlapping.
ii) The hard contact approach where contacts are treated as rigid and overlapping of material at contacts is prevented from occurring by the algorithm.

Discontinuum methods may be further categorised into those that assume blocks to be rigd and those that allow modelling of their deformation.

Of those that allow modelling of block deformation, their various methods by which this is done:

i) The direct method is where each body is discretised into internal and boundary elements and then treated by a continuum method such as finite elements or Lagrangian finite-difference within the body, interacting with other bodies according to the constitutive laws of the boundary elements.

ii) Another method used to obtain the deformation of a discrete body is by the linear superposition of a number model of deformation. Williams and Mustoe (1987). This approach is potentially very efficient, however non-linear deformation becomes a problem, for which superposition does not apply.

The applicability of each approach depends on the relative importance of contact stiffness to material deformability in the physics of the problem under consideration.

3.1.2.1 Computational Limit Analysis

The underlying framework for limit analysis and its application to masonry structures was outlined earlier, which provided an indication that optimization techniques (e.g. Linear Programming) may be applied to search for the exact solution, corresponding to the exact load factor λp. Livesley (1978) noticed the amenability of Heyman's limit analysis model to linear programming optimisation. He used this approach to search the static equilibrium or lower bound solution space, where the objective function is the maximization of the collapse load factor, subject to the constraints of the equilibrium equations. He reduced the stresses in the joint of a voussoir to resultants at the intrados and the extrados, corresponding to the limits of the lower bound static equilibrium condition. An equilibrium formulation, similar to that proposed initially by Livesley (1978), which can be solved very efficiently using modern interior point Linear

Programming (LP) algorithms was presented by Gilbert (2007). This algorithm searches for a line of thrust that corresponds to the largest load factor that satisfies equilibrium and the yield conditions for rotation and sliding. Gilbert developed this algorithm into a commercial software package. In this software, the load dispersal by the soil fill is modelled in the same manner as Choo et al, described earlier, namely by a linear Boussinesq distribution within the bounds of a pair of inclined planes dropping from the point of application of the load at a specified angle. Passive resistance of the soil is modelled by horizontal pressure acting against displacement of the arch into the soil, proportional the in-situ vertical pressure by at a specified coefficient of lateral earth pressure. The code also enables modelling of the effects of support movements.

This concept has been developed further by Smith and Gilbert (2007) who have developed a novel limit analysis procedure, termed 'discontinuity layout optimization' (DLO). This algorithm used linear programming to find an optimal layout of discontinuities in a two-dimensional medium subjected to an imposed load, such that the resulting failure mechanism occurs with the minimum work done at the discontinuities. Gilbert et al (2010) incorporated DLO in their limit analysis to model the soil fill in masonry arch bridges and found that reasonable estimates of load carrying capacity were obtained when partially mobilised soil strength was used.

3.1.2.2 Discrete Element Methods

The discrete element methods explicitly compute the motion of a large number of individual bodies as they interact with each other at mutual discontinuities. Cundall and Hart (1992) provide the following definition of a discrete element method: the name "discrete element" applies to a computer program only if it (a) allows finite displacements and rotations of discrete bodies, including complete detachment; and (b) recognizes new contacts automatically as the calculation progresses.

Cundall and Hart (1992) identify the following four main classes of codes that conform to the above definition

1. **Distinct element programs** use an explicit time-stepping scheme to solve the equations of motion directly. Bodies may be rigid or deformable. The 'soft contact' approach described earlier is adopted. 'Static relaxation' belongs to the same class. Representative codes are TRUBAL (Cundall and Strack 1979), UDEC (Cundall 1980; Cundall and Hart 1985), 3DEC (Cundall 1988; Hart et al. 1988), DIBS (Walton 1980), 3DSHEAR (Walton et al. 1988) and PFC (Itasca 1995).
2. **Modal methods** These also adopt the soft contact approach like the distinct element method. However, as described earlier, for deformable bodies, modal superposition is used (e.g., Williams and Mustoe 1987). This method is better-suited to situations in which only small linear deformations occur such as for loosely packed discontinua; in dynamic simulation of dense packings, eigenmodes are apparently not revised to account for additional contact constraints. A representative code is CICE (Hocking et al. 1985).
3. **Discontinuous deformation analysis** adopts the 'hard' contact approach, and bodies may be rigid or deformable. The condition of no-penetration is achieved by an iterative scheme; the deformability comes from superposition of strain modes. The relevant computer program is DDA (Shi 1989).
4. **Momentum-exchange methods** assume both the contacts and bodies to be rigid: momentum is exchanged between two contacting bodies during an instantaneous collision. Friction sliding may be represented (for example, see Hahn 1988).
5.

Another class of codes, defined as limit equilibrium methods, can also model multiple intersecting discontinuities but are not classified as discrete element code. These codes use vector analysis to establish whether it is kinematically possible for any block in a blocky system to move and become detached from the system. This approach does not examine subsequent behaviour of the system of blocks or redistribution of loads. All blocks are assumed rigid. The "key-block" theory by Goodman and Shi (1985) and the vector stability analysis approach by Warburton (1981) are examples of this method.

3.1.2.3 The Universal Distinct Element Code (UDEC)

This analysis tool has been used in the present research and will therefore be described in detail and in the context of its application in the present work. UDEC is designed to model discontinuous media for geotechnical problems, particularly jointed rock masses in which the deformation is strongly influenced by a system of predefined planes of weakness (Cundall and Hart, 1992). Masonry is a medium of this type, where the relatively stiff masonry units are interfaced by a pattern of mortar joints at which most of the deformation is concentrated, particularly tensile/rotational and shear failure.

The program computes the kinematics of a predefined set of interacting blocks in a time-explicit finite difference scheme. These blocks may be rigid or deformable. Deformable blocks are discretised into a triangulated mesh of material nodes. Since UDEC is designed for geotechnical problems, deformable blocks may be attributed nonlinear constitutive models suitable for soil, such as the Mohr-Coulomb yield criterion. Thus a region of soil may be represented in a UDEC model as a deformable block with a suitable constitutive model attributed to it. This feature is useful for modelling the interaction between the soil fill and the masonry arch. Furthermore the interfaces between blocks are treated explicitly in UDEC. In deformable blocks, the material nodes that lie on the block boundary where it is in contact with another block are treated as points of contact. In rigid blocks, a pair of contact points is created at each end of each edge of the polygonal block in contact with another (Figure below). These interfaces are treated as mutual boundary conditions between blocks. This is ideal for the study of interaction between fill and the masonry as well as between masonry units at mortar joints, particularly for investigating the general relationship betweeen external loading on the arch and the resulting internal forces and mechanisms responsible for or leading to failure. Nodes of deformable blocks as well as contact points between blocks belong to a class of computational object in UDEC termed ‘grid-points’. These are material points at which UDEC evaluates the Lagrangian kinematics and forces. State information at every location of contact between blocks is available at any time step.

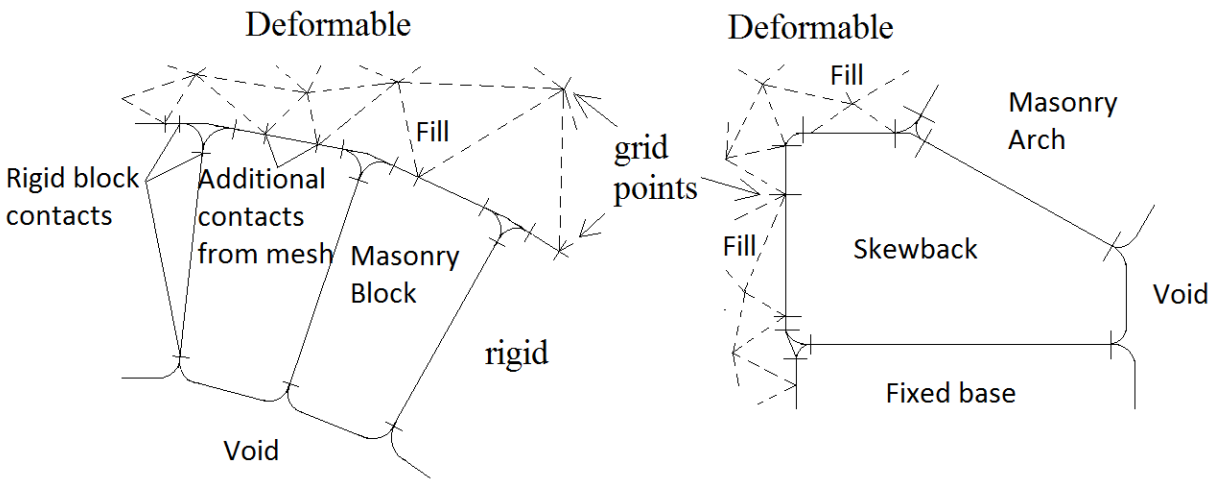

Contact creation in the UDEC model

The contact forces and displacements at the interfaces of a stressed assembly of blocks are found through an incremental solution procedure identical to that used by the 'explicit finite-difference method' for continuum analysis. The solution procedure does not require global equilibrium, but satisfies Newton's laws of motion and constitutive relations locally for individual grid-points, including inertial terms. This avoids the difficulties of global matrix inversion, simplifying the definition of constitutive relations and providing the flexibility to model highly nonlinear materials. This provides the potential for complex realistic behaviour to emerge from the interaction of a system of relatively simple computational elements. The explicit treatment of inertial terms enables concentration and dissipation of kinetic energy to be modelled directly, allowing physical instability and path dependent nonlinear behaviour to occur naturally without the risk of numerical instability.

3.2 Modelling Objectives

A primary objective of the numerical model in the present research is to test the hypothesis that the rigid block assumption for the masonry units, relying only on friction at their interfaces, together with the non-associative Mohr-Coulomb criterion for the fill, may be used to obtain reasonably accurate estimates of the ultimate limit state of the arch-fill system. The reason for testing this hypothesis is that this provides manageable bases from which a practical theoretical model may be developed and then qualitatively as well as quantitatively test with respect to both physical land numerical models.

Another objective the numerical modelling described in the present section is to provide some degree of insight in to the behaviour of arch-fill system that may prove useful in developing the theoretical model, particularly with respect to the deformation of the fill and it's interaction with the arch.

3.3 Model Setup

The geometry of the interior of the test chamber as detained in Figure 2.7 was replicated in the UDEC model. A rigid block of arbitrary thickness (50mm) was used to form the boundary of the system, with the inside dimensions matching those of the interior of the physical test chamber (Figure 3.9). The triangulated region is a single deformable block attributed with a non-associative Mohr-Coulomb plasticity constitutive model. The abutments, skewbacks and arch are of the same design dimensions as the physical model. A departure from the geometry of the physical model is the plain voussoir construction in the numerical model in place of the header-bonded construction in the physical model, however as explained in Chapter 2, the behaviour of these two types of construction are practically the same.

Blocks not containing any triangulation are modelled as rigid blocks. Mortar joints are modelled simply as the zero-thickness interfaces between the rigid masonry units. These interfaces do however have finite stiffnesses assigned to them in compression and shear, but not in tension. Likewise, although the blocks themselves are modelled as purely rigid and thus of infinite strength, at sufficiently high concentration of compressive stress, the interfaces, being of finite

stiffness may exceed a maximum overlap, fixed by the software. In shear however, shear strength is specified in the form of a Coulomb friction criterion in the present research.

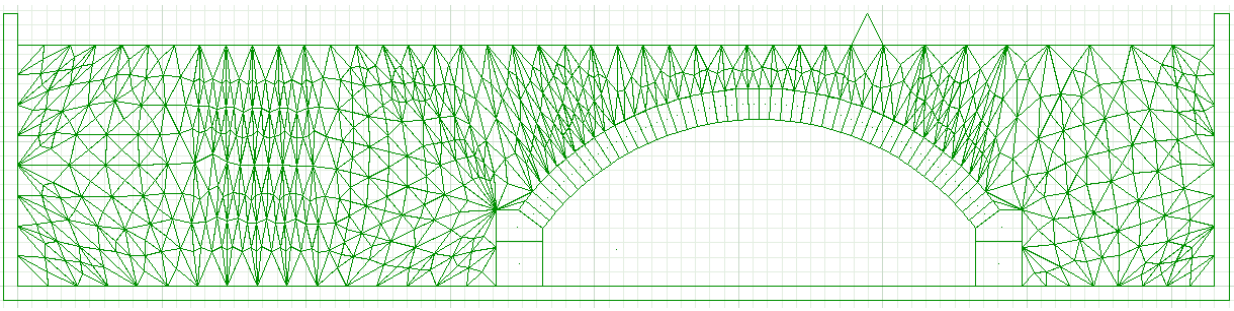

Figure 3.9 – Layout if the UDEC mode for EP1 static loading configuration

The sleepers at which the vertical loads are applied to the fill surface, are simulated by provision of a vertex at each loading position that spreads to the width of the sleeper. The material of this loading vertex is attributed with those of structural steel as is the case in the physical model. This was found through various trials to be the most stable way to apply the loads without encountering any numerical complications during running of the load test simulation.

In order to enable the numerical simulation of the physical load test for the static regime to be complete within a reasonable period of time such that it would be practical to use as a research tool, it was necessary to alter the time-step by means of mass scaling, which is a feature available to be implemented within UDEC if required. This was used to increase the size of the time step to 0.2 s which was the same time interval as the sampling rate of the data acquisition system in the physical model. Accordingly, the static load was increased gradually by controlling the vertical settlement of the loading sleepers at a rate of 10mm per hour to mach the rate at which the physical model was loaded. Fortunately, it was fount that the loading rate applied, together with the application of mass-scaling, did not have an adverse effect on the adherence of the numerical model to a state of equilibrium throughout the system during simulation of the displacement controlled static loading test. The conformity of the numerical model to a state of equilibrium at all times throughout the simulation was verified theoretically by demonstration of it’s conformity to the governing differential equations.

3.3.1 Theoretical Validation

3.3.1.1 Conformity of the UDEC model to the differential equations for equilibrium

3.3.1.1.1 Formulation of governing differential equations for equilibrium

Consider a small wedge-like segment of a cylindrical arch of small internal angle δ, bounded by the intrados, extrados and radial cross-sections at angles θ_1 and θ_2 from the vertical as shown in Figure 3.10 (a). The external forces acting on the wedge will consist of the weight W of the wedge and the forces P due to pressure acting on the extrados surface of the wedge. Each of these will in general have a component acting in the radial direction and a component acting in the direction tangential to the arch as shown in Figure 3.10(b). The internal forces acting on the cross-sections either side of the wedge may also be separated into normal and shearing components. All the external and internal forces mentioned above are presented in Figure 5, with associated definitions provided in Table 3.1.

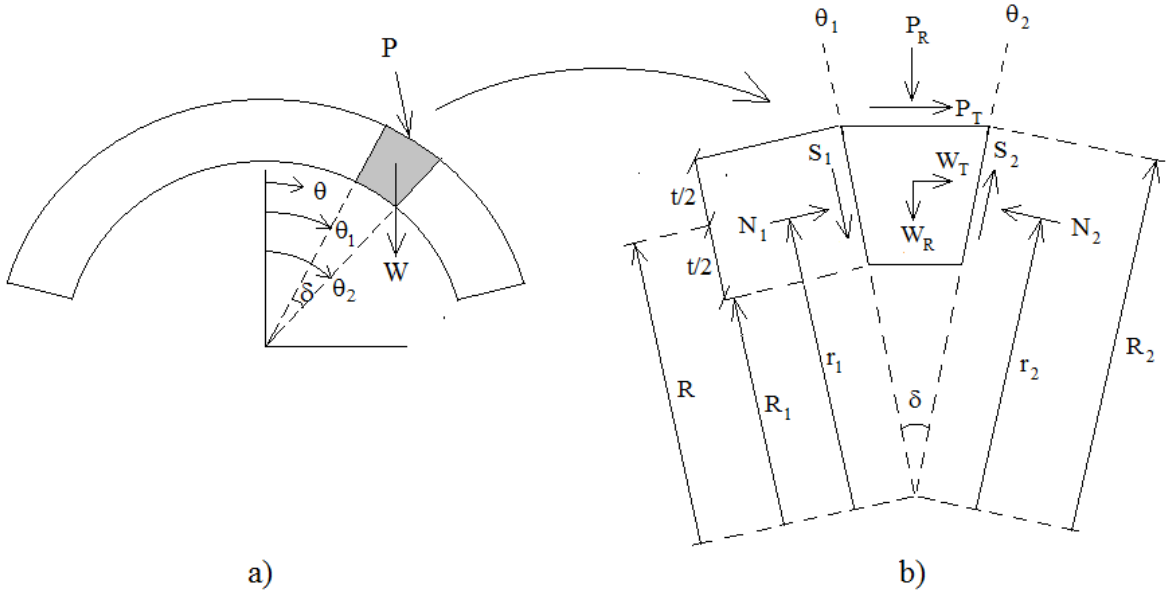

Figure 3.10 – External and internal forces acting on a small segment of an arch a) Total forces and angular ordinate and b) Force components in polar coordinates and sign convention adopted

Table 3.1 – Nomenclature of forces in Figure 3.10(b)

w_R	Component of the weight of the wedge resolved in the radial direction
w_T	Component of the weight of the wedge resolved in the tangential direction
P_R	Component of the resultant force due to external pressure σ_R acting on the extrados face of the wedge, resolved in the radial direction
P_T	Component of the resultant force due to external pressure σ_T acting on the extrados face of the wedge, resolved in the tangential direction, clockwise about the arch centre.
$N_{1,2}$	Component of the resultant force due to internal stress acting on the radial cross-section to the left of the wedge, resolved in the direction normal to the cross-section
$S_{1,2}$	Component of the resultant force due to internal stress acting on the radial cross-section, resolved in the anti-clockwise direction, tangential to the cross-section

The following model describes the relationship between external and internal forces in the form of a set of differential equations derived from the three available equations of equilibrium in two-dimensions. These are obtained by resolving forces in the radial and tangential directions and equating moments about the centre of the arch.

Equilibrium of forces in the radial direction gives:

$$(S_2 - S_1).cos\left(\frac{\delta}{2}\right) + (N_1 + N_2).sin\left(\frac{\delta}{2}\right) = P_R + W_R$$

Equilibrium of forces in the tangential direction gives:

$$(N_2 - N_1).cos\left(\frac{\delta}{2}\right) - (S_1 + S_2).sin\left(\frac{\delta}{2}\right) = P_T + W_T$$

Since the radial forces, P_R, w_R, S_1 and S_2 pass through the centre of the arch, there are no moments due to these forces about this point. Hence, equating moments about the centre of the arch:

$$\Rightarrow \qquad N_2.r_2 - N_1.r_1 = P_T.R_2 + w_T.R$$

Letting $\qquad \delta \to d\theta$

$$\Rightarrow \qquad cos\left(\frac{\delta}{2}\right) \to 1, \qquad sin\left(\frac{\delta}{2}\right) \to \frac{d\theta}{2}$$

$$\theta_1 = \theta, \qquad N_1 = N, \qquad S_1 = S, \qquad r_1 = r$$

$$\theta_2 = \theta + d\theta, \qquad N_2 = N + dN, \qquad S_2 = S + dS, \qquad r_2 = r + dr$$

$$W \to dw = \frac{dw}{d\theta}.d\theta = \dot{w}.d\theta$$

$$\Rightarrow \qquad W_R = \dot{w}.cos\,\theta, \qquad W_T = \dot{w}.sin\,\theta$$

In the case of a cylindrical arch, $\dot{w}$ is treated as a constant:

$$dw = \dot{w}.d\theta = \frac{\gamma}{2}(R_2^2 - R_1^2).d\theta = \gamma.R.t.d\theta$$

and $\qquad P_R = \sigma_R.R_2.d\theta, \qquad P_T = \sigma_T.R_2.d\theta$

Equilibrium of forces in the radial direction gives:

$$(S + dS - S).1 + (N + N + dN).\frac{d\theta}{2} = \sigma_R.R_2.d\theta + \dot{w}.d\theta.cos(\theta)$$

$dN.d\theta \approx 0 \Rightarrow$ $$\frac{dS}{d\theta} + N = \sigma_R.R_2 + \dot{w}.cos(\theta) = u_S(\theta) \quad (1)$$

Equilibrium of forces in the tangential direction gives:

$$(N + dN - N).1 - (S + S + dS).\frac{d\theta}{2} = \sigma_T.R_2.d\theta + \dot{w}.d\theta.sin(\theta)$$

$dS.d\theta \approx 0 \Rightarrow$ $$\frac{dN}{d\theta} - S = \sigma_T.R_2 + \dot{w}.sin(\theta) = u_N(\theta) \quad (2)$$

Equating moments about the centre of the arch gives:

$$(N + dN).(r + dr) - N.r = \sigma_T.R_2^2.d\theta + \dot{w}.d\theta.sin(\theta).R$$

$dN.dr \approx 0 \Rightarrow$ $$r.\frac{dN}{d\theta} + N.\frac{dr}{d\theta} = \frac{d}{d\theta}(N.r) = R_2^2.\sigma_T + R.\dot{w}.sin(\theta)$$

$let\ N.r = M \Rightarrow$ $$\frac{dM}{d\theta} = R_2^2.\sigma_T + R.\dot{w}.sin(\theta) = u_M(\theta) \quad (3)$$

The angle of resultant thrust T with respect to any radial cut in the arch is proportional to the ratio of the shear to normal components of the force acting on that radial cut. With reference to Figure 3.11:

$$\frac{d\bar{r}}{\bar{r}.d\theta} = -\frac{S}{N}$$

$\Rightarrow$ $$\frac{d\bar{r}}{d\theta} = -\frac{S}{N}.\bar{r} \quad (4)$$

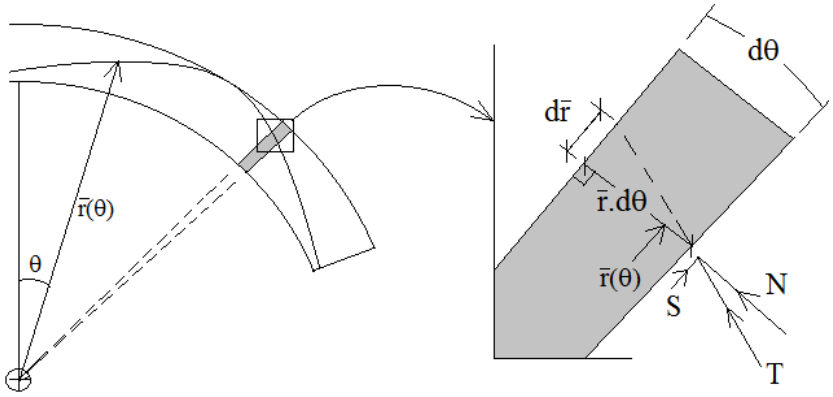

Figure 3.11 – relationship between Normal and Shear forces at a radial cross section with the radial gradient of the line of thrust

Conformity of the UDEC model to the governing differential equations

In order to test how well the UDEC model behaviour conformed to the proposed differential Eqs. (*1*), (2), (3) the state variables, S, N and r, their numerical derivatives and the pressures $\sigma_R$and σ_T were extracted from the UDEC simulation output for EP1. The left and right hand sides of each equation are plotted on the same axes (Figure 3.12). Since the contribution of external pressure exerted by the fill on to the arch at the yielding stage of loading is very large compared to that of the self-weight of arch element, the terms involving $\dot{w}$ are ignored.

The behaviour of the UDEC model when subjected to only self weight is compared with a particular solution of the governing differential equations for a well known problem of the minimum thickness required for an arch to remain stable under only self weight. This is demonstrated in the sections following the present section.

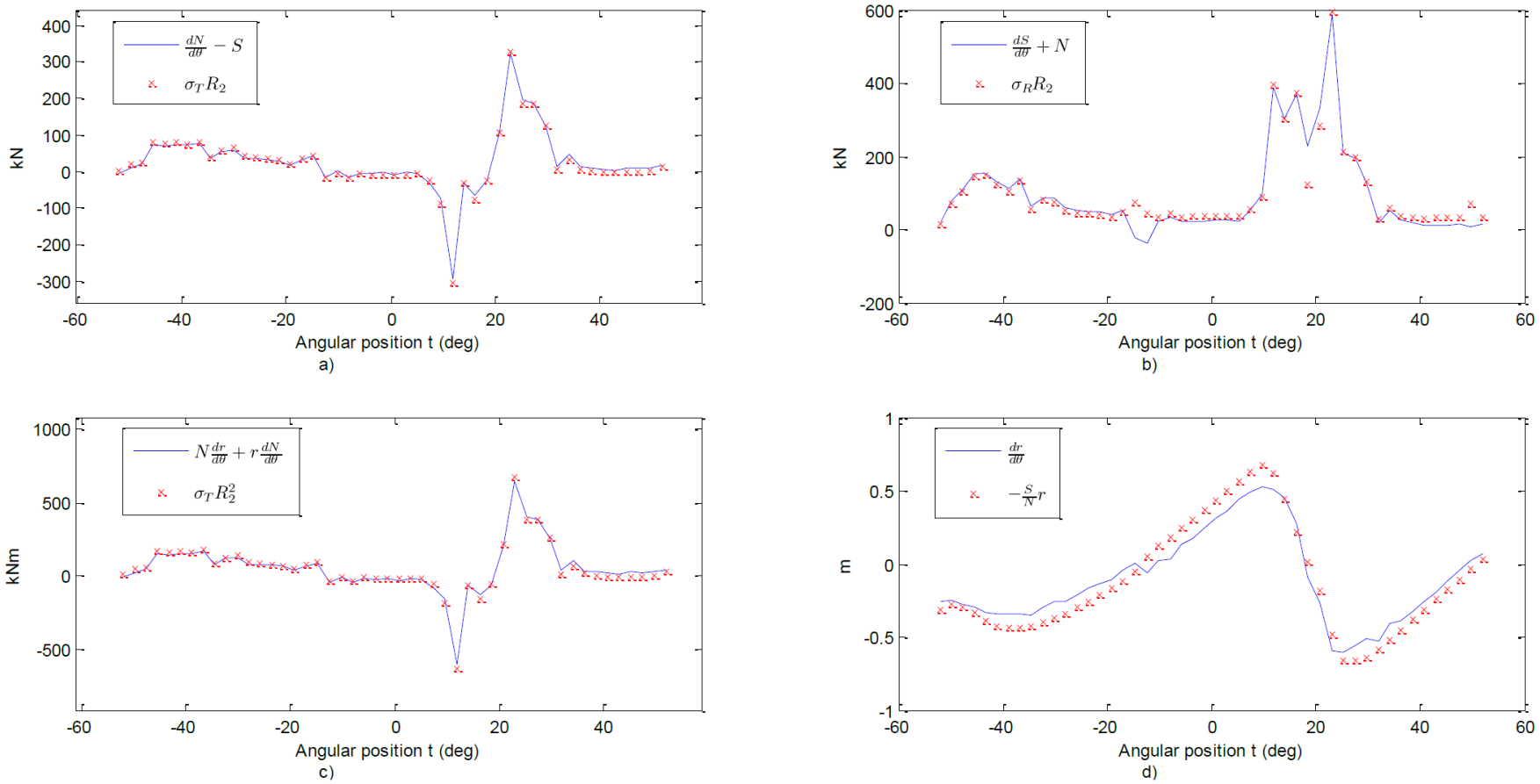

Figure 3.12 – Comparison of LHS and RHS of the governing differential equations of the proposed analytical model derived from output data from a UDEC simulation of a load test on the soil filled masonry arch., ,

a) Eq. (2) , b) Eq. (1), c) Eq. (3) d) Eq. (4)

3.3.1.2 Conformity of the UDEC model to a particular solution – minimum thickness under self weight

Eqs. (1), (2) and (3) are a coupled system of linear differential equations and may thus be solved simultaneously using Laplace transforms by writing them in the state space representation:

$$\begin{bmatrix} \dot{N} \\ \dot{S} \\ \dot{M} \end{bmatrix} = \begin{bmatrix} 0 & 1 & 0 \\ -1 & 0 & 0 \\ 0 & 0 & 0 \end{bmatrix} \begin{bmatrix} N \\ S \\ M \end{bmatrix} + \begin{bmatrix} u_N \\ u_S \\ u_M \end{bmatrix} \tag{5}$$

Where N, S and M are the internal normal force, shear force and moment as defined earlier and $\dot{N}$, $\dot{S}$ and $\dot{M}$ represent their derivatives with respect to θ. Eqn. (5) may be written in the compact matrix algebra form:

$$\dot{\boldsymbol{x}} = \boldsymbol{A}\boldsymbol{x} + \boldsymbol{u} \tag{6}$$

N, S and M, represented by $\boldsymbol{x}$ in Eq. (6) may be obtained by taking Laplace Transforms between the θ and s domains using Eq. (7), where a transformed function is denoted here by the subscript $\mathcal{L}$ and an inverse transform by $\mathcal{L}^{-1}\{\dots\}$

$$x(\theta) = \mathcal{L}^{-1}\{(s.\boldsymbol{I} - \boldsymbol{A})^{-1}\}x(0) + \mathcal{L}^{-1}\{(s.\boldsymbol{I} - \boldsymbol{A})^{-1}\boldsymbol{u}_{\mathcal{L}}\} \tag{7}$$

Where $$x(\theta) = \boldsymbol{x} = \begin{bmatrix} N(\theta) \\ S(\theta) \\ M(\theta) \end{bmatrix}, \qquad x(0) = \begin{bmatrix} N(0) \\ S(0) \\ M(0) \end{bmatrix}$$

$$\Rightarrow \qquad \mathcal{L}^{-1}\{(s.\boldsymbol{I} - \boldsymbol{A})^{-1}\} = \begin{bmatrix} cos\,\theta & sin\,\theta & 0 \\ -sin\,\theta & cos\,\theta & 0 \\ 0 & 0 & 1 \end{bmatrix}$$

$$\mathcal{L}^{-1}\{f_{\mathcal{L}}(s).g_{\mathcal{L}}(s)\} = f * g(t) = \int_{-\infty}^{\infty} f(t)\,.\,g(t-\tau)d\tau$$

$$\Rightarrow \qquad \mathcal{L}^{-1}\{(s.\boldsymbol{I} - \boldsymbol{A})^{-1}\boldsymbol{u}_{\mathcal{L}}\} = \mathcal{L}^{-1}\{(s.\boldsymbol{I} - \boldsymbol{A})^{-1}\} * \boldsymbol{u}$$

$$\Rightarrow \qquad \mathcal{L}^{-1}\{(s.\boldsymbol{I}-\boldsymbol{A})^{-1}\} * \boldsymbol{u} = \begin{bmatrix} \dot{w}.\theta\sin\theta + R_2(\sigma_R * \sin\theta + \sigma_T * \cos\theta) \\ \dot{w}.\theta\cos\theta + R_2(\sigma_R * \cos\theta - \sigma_T * \sin\theta) \\ R.\dot{w}.(1-\cos\theta) + R_2^2.\sigma_T * 1 \end{bmatrix}$$

$$\Rightarrow \qquad x(\theta) = \mathcal{L}^{-1}\{(s.\boldsymbol{I}-\boldsymbol{A})^{-1}\}x(0) + \mathcal{L}^{-1}\{(s.\boldsymbol{I}-\boldsymbol{A})^{-1}\} * \boldsymbol{u} =$$

$$\begin{bmatrix} N(\theta) \\ S(\theta) \\ M(\theta) \end{bmatrix} = \begin{bmatrix} \cos\theta\,.N(0) + \sin\theta.S(0) \\ \cos\theta.S(0) - \sin\theta\,.N(0) \\ r(0).N(0) \end{bmatrix} + \begin{bmatrix} \dot{w}.\theta\sin\theta + R_2(\sigma_R * \sin\theta + \sigma_T * \cos\theta) \\ \dot{w}.\theta\cos\theta + R_2(\sigma_R * \cos\theta - \sigma_T * \sin\theta) \\ R.\dot{w}.(1-\cos\theta) + R_2^2.\sigma_T * 1 \end{bmatrix} \qquad (8)$$

The general solution given in Eq. (8) may also be deduced directly from Figure 3.13.

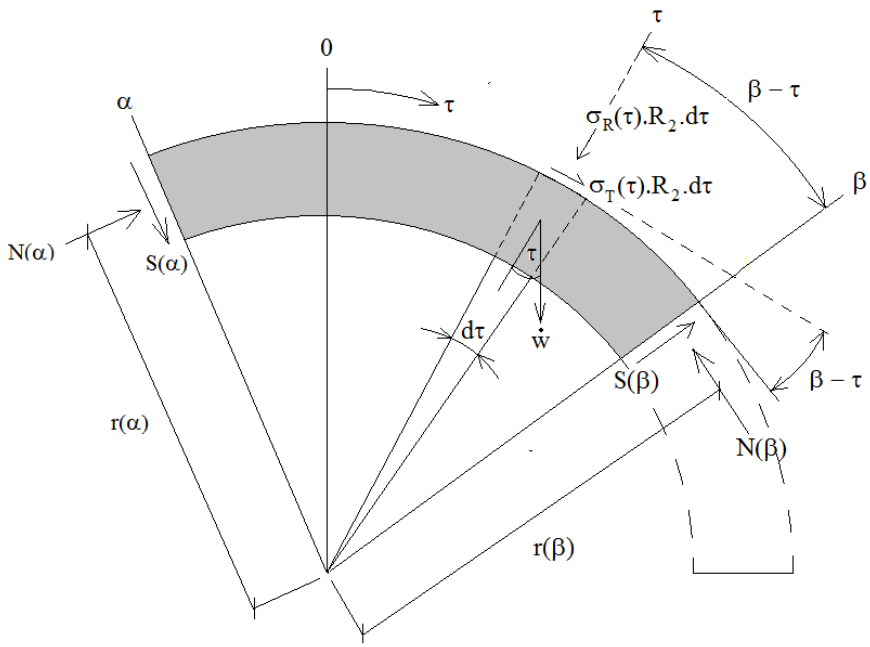

Figure 3.13 - Physical interpretation of the general solution

Consider the segment bounded by radii $\alpha = 0$ and $\beta = \theta$ in Figure 3.13, where $\alpha \leq \tau \leq \beta$

Resolving forces parallel to $N(\theta)$ results in $N(\theta)$ from Eq. (8):

$$\Rightarrow \quad N(\theta) = N(0).\cos\theta + S(0).\sin\theta + \int_0^\theta \dot{w}.\sin\theta\,.d\tau$$

$$+\int_0^\theta \sigma_R(\tau).sin(\theta-\tau).R_2.d\tau + \int_0^\theta \sigma_T(\tau).cos(\theta-\tau).R_2.d\tau$$

$$= N(0).\cos\theta + S(0).\sin\theta + \dot{w}.\theta\sin\theta + R_2(\sigma_R * \sin\theta + \sigma_T * \cos\theta)$$

Resolving forces parallel to $S(\theta)$ results in $S(\theta)$ from Eq. (7):

$$\Rightarrow \quad S(\theta) = N(0).\sin\theta - S(0).\cos\theta + \int_0^\theta \dot{w}.\cos\theta\,.d\tau$$

$$+\int_0^\theta \sigma_T(\tau).sin(\theta-\tau).R_2.d\tau - \int_0^\theta \sigma_R(\tau).cos(\theta-\tau).R_2.d\tau$$

$$= N(0).\sin\theta - S(0).\cos\theta + \dot{w}.\theta.\cos\theta + R_2(\sigma_R * \cos\theta - \sigma_T * \sin\theta)$$

Equating moments about the centre results in $M(\theta)$ from Eq. (8):

$$\Rightarrow \quad M(\theta) = r(\theta).N(\theta) = r(0).N(0) + R.\int_0^\theta \dot{w}.\sin\tau\,.d\tau + \int_0^\theta R_2.\sigma_T(\tau).R_2.d\tau$$

$$= r(0).N(0) + R.\dot{w}.(1-\cos\theta) + R_2^2.\sigma_T * 1$$

In light of the interpretation given above, we may express the solution in a more general form where the segment under consideration is bounded by two arbitrary radii, α and β rather than 0 and θ. Below, notation of the form $x(a) = x_a$ is introduced for N, S and r.

$$\Rightarrow \quad N_\beta = N_\alpha.cos(\beta-\alpha) + S_\alpha.sin(\beta-\alpha) + \dot{w}.(\beta-\alpha).sin(\beta)$$

$$+R_2.\int_\alpha^\beta \sigma_R(\tau).sin(\beta-\tau).d\tau + R_2.\int_\alpha^\beta \sigma_T(\tau).cos(\beta-\tau).d\tau \qquad (9)$$

$$S_\beta = S_\alpha.cos(\beta-\alpha) - N_\alpha.sin(\beta-\alpha) + \dot{w}.(\beta-\alpha).cos(\beta)$$
$$+R_2.\int_\alpha^\beta \sigma_T(\tau).sin(\beta-\tau).d\tau - R_2.\int_\alpha^\beta \sigma_R(\tau).cos(\beta-\tau).d\tau \quad (10)$$

$$r_\beta.N_\beta = r_\alpha.N_\alpha + R.\dot{w}.(cos\,\alpha - cos\,\beta) + R_2^2.\int_\alpha^\beta \sigma_T(\tau).d\tau \quad (11)$$

Thus if the state variables N, S and r are known at a known location, α, then they may be found at all other locations β using Eqs. (9), (10) and (11) for a given pressure distribution $\sigma_R(\tau)$ and $\sigma_T(\tau)$.

3.3.2 Particular solution of the equilibrium equations to the minimum thickness problem.

This particular load case has been chosen for elementary validation of the present model because the boundary conditions, $M(0)$, $N(0)$ and $S(0)$ can be readily deduced from the symmetry of the problem. It is thus possible to obtain a particular solution of Eqs. (8).

The general solution (8) may be applied to the same problem, where the line of thrust was assumed to be at the limiting state at which a hinge forms at the extrados of the crown. Thus $r(0)$, $N(0)$ and $S(0)$ may be prescribed as follows:

$$r(0) = R_2\,, \qquad \Phi = \gamma.R.t.\frac{\pi}{2} \quad , \quad \bar{x} = \frac{2R}{\pi}$$
$$N(0) = \frac{\Phi(r(0)-\bar{x})}{r(0)} = \gamma.R.t.\left(\frac{\pi}{2} - \frac{R}{R_2}\right)$$
$$S(0) = 0$$

Applying the conditions of the present case with no external pressure, the solution (8) reduces to:

$$\begin{bmatrix} N(\theta) \\ S(\theta) \\ M(\theta) \end{bmatrix} = \begin{bmatrix} \dot{w}.\theta\,sin\,\theta + cos\,\theta\,.N(0) \\ \dot{w}.\theta\,cos\,\theta - sin\,\theta\,.N(0) \\ R.\dot{w}.(1-cos\,\theta) + R_2.N(0) \end{bmatrix} \quad (12)$$

The line of thrust in the arch is defined by $r(\theta)$ may be obtained from $M(\theta)$ as follows:

$$r(\theta) = \frac{M(\theta)}{N(\theta)}$$

$$\Rightarrow \qquad r(\theta) = \frac{\gamma.R^2.t.(1-cos(\theta)) + R_2.N(0)}{N(0).cos(\theta) + \gamma.R.t.\theta.sin(\theta)}$$

$$\Rightarrow \qquad r(\theta) = \frac{R(1-cos(\theta)) + R_2.\frac{\pi}{2} - R}{\left(\frac{\pi}{2} - \frac{R}{R_2}\right).cos(\theta) + \theta.sin(\theta)} \qquad (13)$$

The above result may be verified from elementary Statics as shown in the following section

3.3.3 Location of centre of gravity on the vertical plane of an arch segment

For uniformly distributed weight, γ with respect to the central angle, θ (Figure 3.14(a)) the location, $\bar{x}$ of w may be obtained by considering moments about the centre a follows:

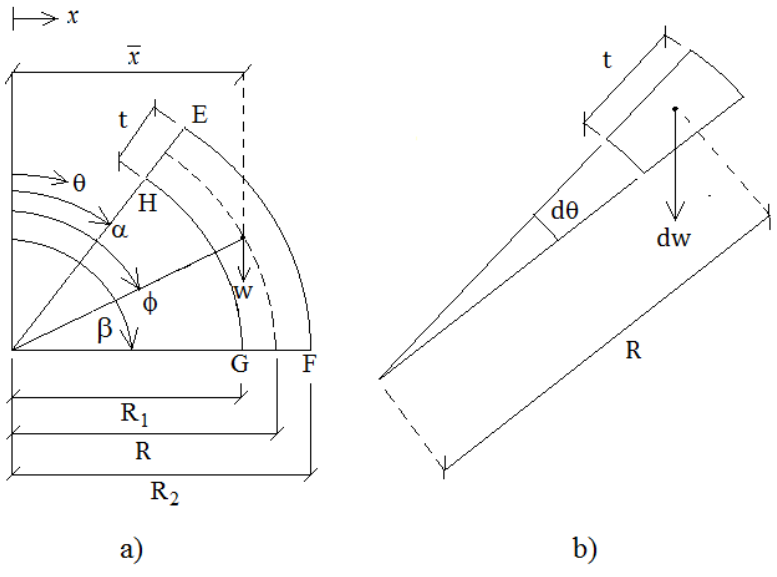

Figure 3.14 – Centre of gravity of an arch segment

$$\bar{x}w = \int_{\alpha}^{\beta} x dw \tag{14}$$

and $$w = \int_{\alpha}^{\beta} dw =$$

$\Rightarrow$ $$w = \frac{\gamma}{2}\int_{\alpha}^{\beta}(R_2^2 - R_1^2)d\theta \tag{15}$$

$\Rightarrow$ $$w = \gamma \int_{\alpha}^{\beta} \frac{1}{2}(R_2 + R_1)(R_2 - R_1)d\theta$$

From

$$dw = \gamma.t.R.d\theta \tag{16}$$

Figure 3.14 (b)

$R\ and\ t\ constant \Rightarrow$ $$w = \gamma.t.R\int_{\alpha}^{\beta} d\theta = \gamma.t.R(\beta - \alpha) \tag{17}$$

From $$x = R.sin\,\theta$$

Figure 3.14 (a) $$\bar{x} = R.sin\phi$$

$\Rightarrow$ $$\gamma.t.R^2(\beta - \alpha).sin\phi = \gamma.t.R^2\int_{\alpha}^{\beta} sin\,\theta\, d\theta$$

$\Rightarrow$ $$(\beta - \alpha).sin\phi = [-cos\,\theta]_{\alpha}^{\beta} = cos\,\alpha - cos\,\beta$$

$\Rightarrow$ $$sin\phi = \frac{cos\,\alpha - cos\,\beta}{(\beta - \alpha)} \tag{18}$$

$\Rightarrow$ $$\bar{x} = R.sin\phi = \frac{R(cos\,\alpha - cos\,\beta)}{(\beta - \alpha)} \tag{19}$$

3.3.4 Application of Coulomb's Statics to the minimum thickness problem for a cylindrical arch under self weight

Since the vertical joint Ga lies on the axis of symmetry of the arch, horizontal displacement is not possible at G. Therefore at the onset of rotation of $GaMm$, G will only be free to displace vertically downward and the hinge at M would thus begin to spread outward to the right. Since Mm is the only joint allowed to occur between Ga and Ee in Coulomb's analysis, this must therefore be accompanied by the onset of clockwise rotation of the rigid body $MmEe$ about e. We may therefore assume that the thrust passes through e at the onset of clockwise rotation of $MmEe$. The mechanism described above in which anti-clockwise rotation of $GaMm$ occurs simultaneously with clockwise rotation of $MmEe$ would be of the same form as in **Error! Reference source not found.** (c), half of which is shown in Figure 3.15(a) below, for which Couplet sought a minimum thickness to radius ratio in the case of a cylindrical arch. We can thus adapt the notation from Coulombs original geometry () to describe Coulomb's analysis, to the semicircular arch of constant thickness with no distinction between the peer and the rest of the arch at Bb, as shown in Figure 3.15(b).

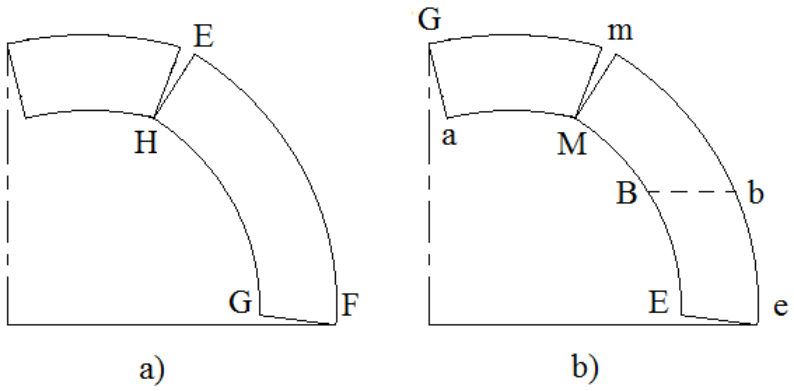

Figure 3.15

Coulomb gave a condition for rotational equilibrium of the whole structure $GaEe$ that the resultant of the horizontal thrust at G and that of the weight of $GaEe$ must pass through Ee and thus at the limiting state at the onset of clockwise rotation of $GaEe$, this resultant would pass through e. Although the limiting state at the onset of the rotational mechanism of Figure 3.15

implies the situation shown in Figure 3.16(a), in which Coulombs condition for rotational stability about e is at its limiting case, the same condition could also be satisfied without an intermediate hinge at M such that $GaEe$ is a the onset of rotation about e as shown in Figure 3.16 (b).

In the model shown in Figure 3.16(b), it is assumed that $GaEe$ is at a limiting state of equilibrium, at the onset of clockwise rotation about e, such that the line of thrust passes through G and e. We know this to be the case at the onset of the mechanism of Figure 3.16(a) but it is not necessarily the case in an arch that is not at this limiting state. Thus in order to find the critical thickness at which this limiting state will occur, we first consider the arch supported by pins at G and e as shown in Figure 3.16(b) and then find the critical thickness at which a hinge Mm required to induce the mechanism shown in Figure 3.16(a) will occur. Since the force-polyline in Figure 3.16(b) is sketched based on the geometry of the structure with reasonable accuracy, the thickness in Figure 3.16(a), which is only illustrative, is clearly too great for this mechanism to occur under uniform self weight.

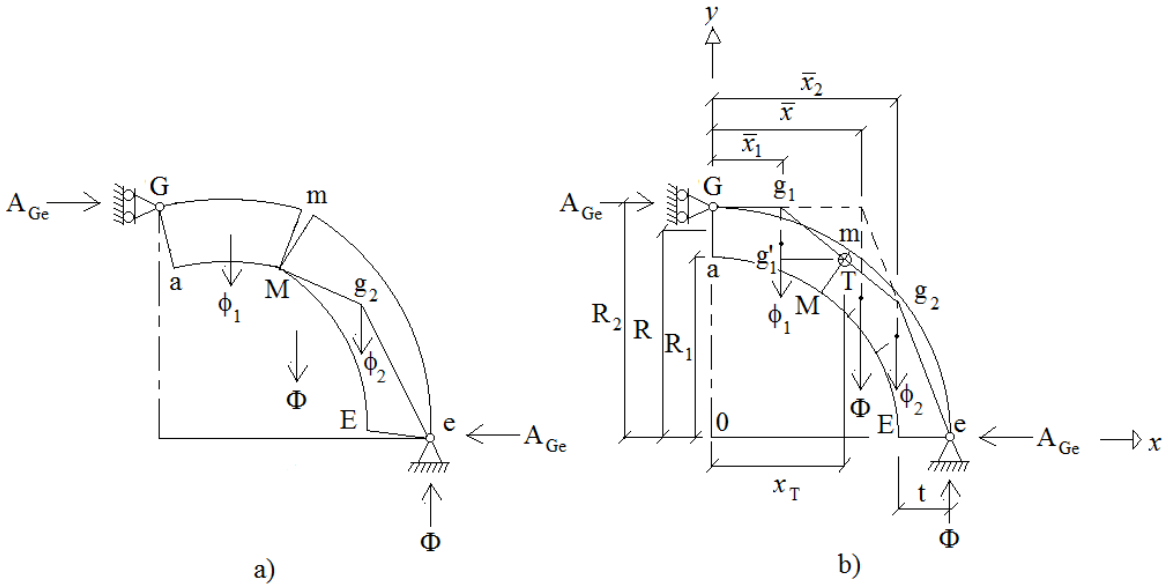

Figure 3.16

In the case shown in Figure 3.16 (b) the complete structure would be a three-pinned arch which is statically determinate and stable under the no-slip assumption. In order for $GaEe$ in Figure 3.16(b) to just become statically unstable, assuming no slip occurs, it must be just thin enough that at some location, Mm, the thrust through Mm acts at M, forming an intermediate hinge on the intrados between Ga and Ee. The geometric relationship between the location of Mm and the location of the thrust along Mm for a cylindrical arch may be observed in Figure 3.16(b), in which the solid polyline from G to e is the force-polyline, of the system in which ϕ_1 and ϕ_2 are modelled as point loads.

In Figure 3.16(b), we know that the thrust at Mm is the resultant of A_{Ge} and the weight $\phi_1$of $GaMm$. Thus the resultant of the thrust at Mm and the weight ϕ_2 of $MmEe$ is equal to the resultant of the thrust A_{Ge} at G and the total weight Φ of $GaEe$. Rotational equilibrium of each of the two segments requires that all forces acting on them are concurrent, thus if the lines of action of A_{Ge} and $\phi_1$intersect at g_1 and the lines of action of ϕ_2 and the total reaction at e intersect at g_2 then the line of action of the thrust through Mm must pass through both g_1 and g_2. The location T of the resultant force or thrust on Mm is thus at the intersection of the lines g_1g_2 and Mm. The location of T is plotted for various locations of Mm in.

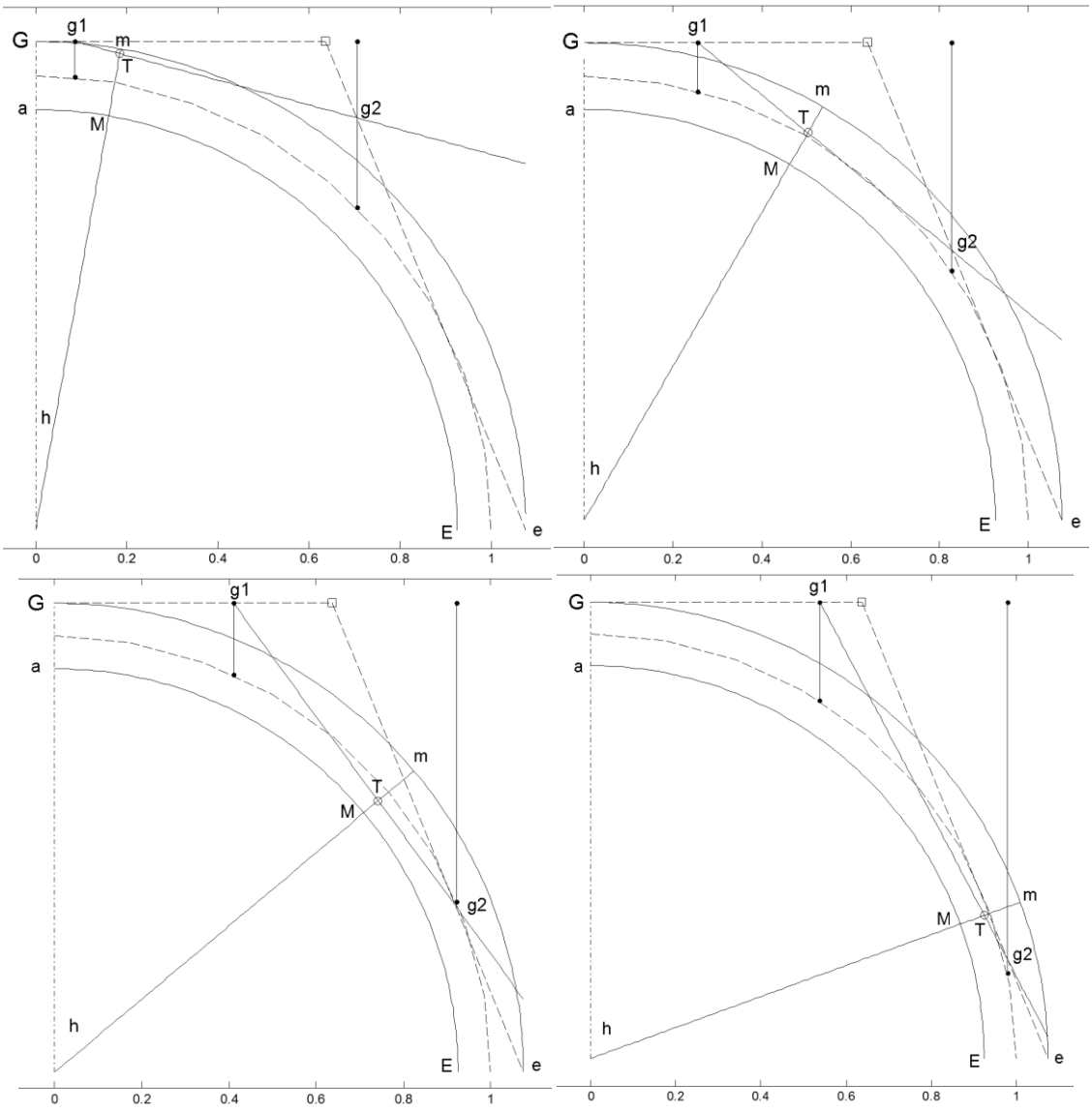

Figure 3.17

The locus of T is by definition the line of thrust in the arch. This may be found simply from the intersection of g_1T the line of action of the resultant of A_{Ge} and $\phi_1$with the line Mm.

A_{Ge} is found by equating its moment about e with that of Φ. Thus with reference to Figure 3.16(b), the radius R_T of T from the centre O may be found as follows:

$moments\ about\ e \Rightarrow$ $$A_{Ge} = \frac{\Phi.(\mathrm{R}_2 - \bar{x})}{\mathrm{R}_2}$$

Eq.**Error! Reference source not found.** $\Rightarrow$ $$\bar{x}_1 = \frac{R}{h}.(1 - cos(h)) \quad (20)$$

and $$\bar{x} = \frac{2R}{\pi}$$

Eq.**Error! Reference source not found.** $\Rightarrow$ $$\phi_1 = \gamma.R.t.h$$

and $$\Phi = \gamma.R.t.\frac{\pi}{2}$$

$\Rightarrow$ $$\frac{g_1 g'_1}{g'_1 T} = \frac{\phi_1}{A_{Ge}} = \frac{h}{\left(\frac{\pi}{2} - \frac{R}{R_2}\right)}$$

Thus the line $g_1 T$ may be defined in Cartesian coordinates by:

$$y - R_2 = -\frac{h}{\left(\frac{\pi}{2} - \frac{R}{R_2}\right)}(x - \bar{x}_1) \quad (21)$$

And the line Mm may be defined by:

$$y = x.cot(h) \quad (22)$$

Where x and y represent Cartesian coordinates from the origin O. Thus substituting $\bar{x}_1$ from Eq. (20) and y from Eq. (22) in to Eq. (21) the horizontal location x_T and thus the radius R_T of T from O may be obtained in terms of h, R and R_2:

$$\Rightarrow \qquad x_T = \frac{R(1-cos(h)) + R_2.\left(\frac{\pi}{2} - \frac{R}{R_2}\right)}{\left(\frac{\pi}{2} - \frac{R}{R_2}\right).cot(h) + h} \tag{23}$$

$$\Rightarrow \qquad R_T = \frac{x_T}{sin(h)} = \frac{R(1-cos(h)) + R_2.\frac{\pi}{2} - R}{\left(\frac{\pi}{2} - \frac{R}{R_2}\right).cos(h) + h.sin(h)} \tag{24}$$

The line of thrust may thus be obtained for a given radius and thickness. The line of thrust for $\frac{t}{R} = 0.15$ for the arch in Figure 3.17 as well as an arch at the critical thickness $\frac{t}{R} = 0.1075$ found by Ochsendorf, followed by a thinner arch at $\frac{t}{R} = 0.05$, are given in Figure 3.18 (a), (b) and (c) respectively.

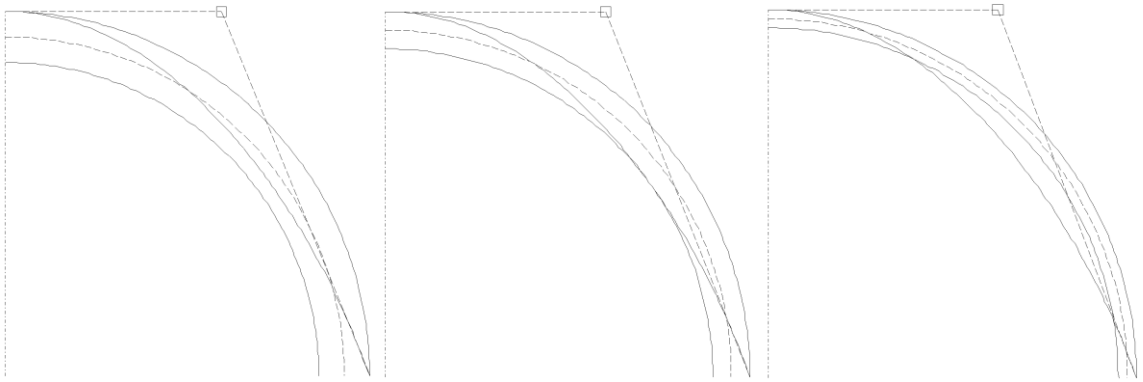

a) b) c)

Figure 3.18

We may determine the minimum thickness to radius ratio at which the thrust will first intersect the intrados by letting:

$$R_T = R - \frac{t}{2}$$

$$R_2 = R + \frac{t}{2}$$

$$and \qquad R = 1$$

$$\Rightarrow \qquad \frac{t}{R} = t$$

This results in an implicit equation that relates the thicknesses t to the values of h where the line of thrust intersects the intrados at those thicknesses. The graphical solution is given in Figure 3.19. The limiting ratio $\frac{t}{R} \approx 1.1074$ is where the arch becomes just thin enough that the line if thrust first touches the intrados and corresponds to a single value of $h \approx 0.95$ radians or 54.43°.

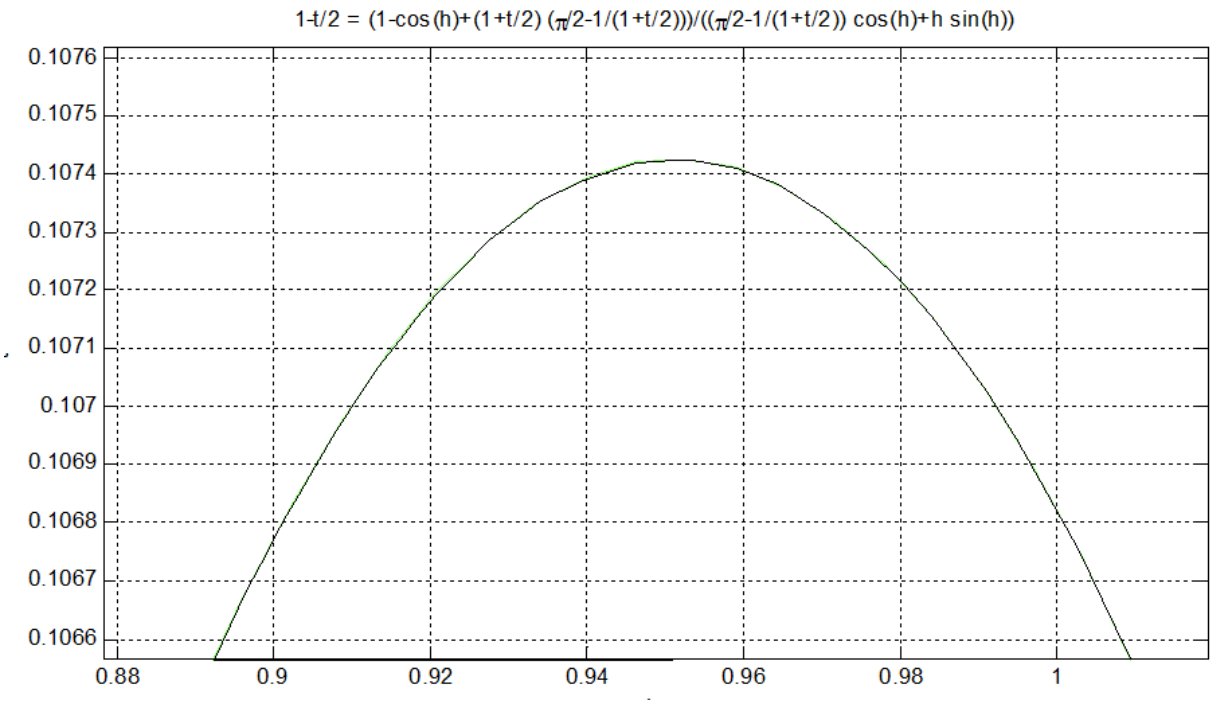

Figure 3.19

The Spanish engineer Joaquin Monasterio wrote a "New theory on the thrust of vaults" between 1805-1810, which was recently discovered and reviewed by (Albuerne and Huerta, 2010). It is the earliest known record of the application of Coulombs theory to masonry arch analysis and he was the first to correctly determine the minimum thickness to lie between $1/8^{th}$ and $1/9^{th}$ of the intrados radius by trial and error, finding the intrados hinge to the nearest integer degree to be 55°.

Table 3.2 compares the present solution (Ahmad, 2015) with those obtained by others for the minimum thickness of a semi-circular, cylindrical arch under self weight as follows:

Table 3.2 – Historical Developments leading to the present solution

	$\frac{t}{R}$	h (degrees)
Couplet (1730)	1.010	45
Monasterio (1805-1810)	1.053 - 1.117	54 - 56
Milankovich (1907)	1.075	54.5
Heyman (1997)	1.060	58.8167
Ochsendorf (2002)	1.075	54.5
Ahmad (2015)	1.074 – 1.075	54.43

3.3.4.1 UDEC solution to the minimum Thickness Problem

A semicircular arch was modelled using UDEC, and gradually reduced in thickness by repeated trials until the thinnest possible arch was found which would not collapse under its own weight. This occurred at $t/R \approx 0.1085$. The discrepancy may be due to the small amount of kinetic energy released after deletion of the material beneath the arch in UDEC that may have prematurely induced collapse. Both the analytical solution from Eqs. (12) and (13), and the UDEC solution are plotted for comparison in Figure 3.20 and Figure 3.21

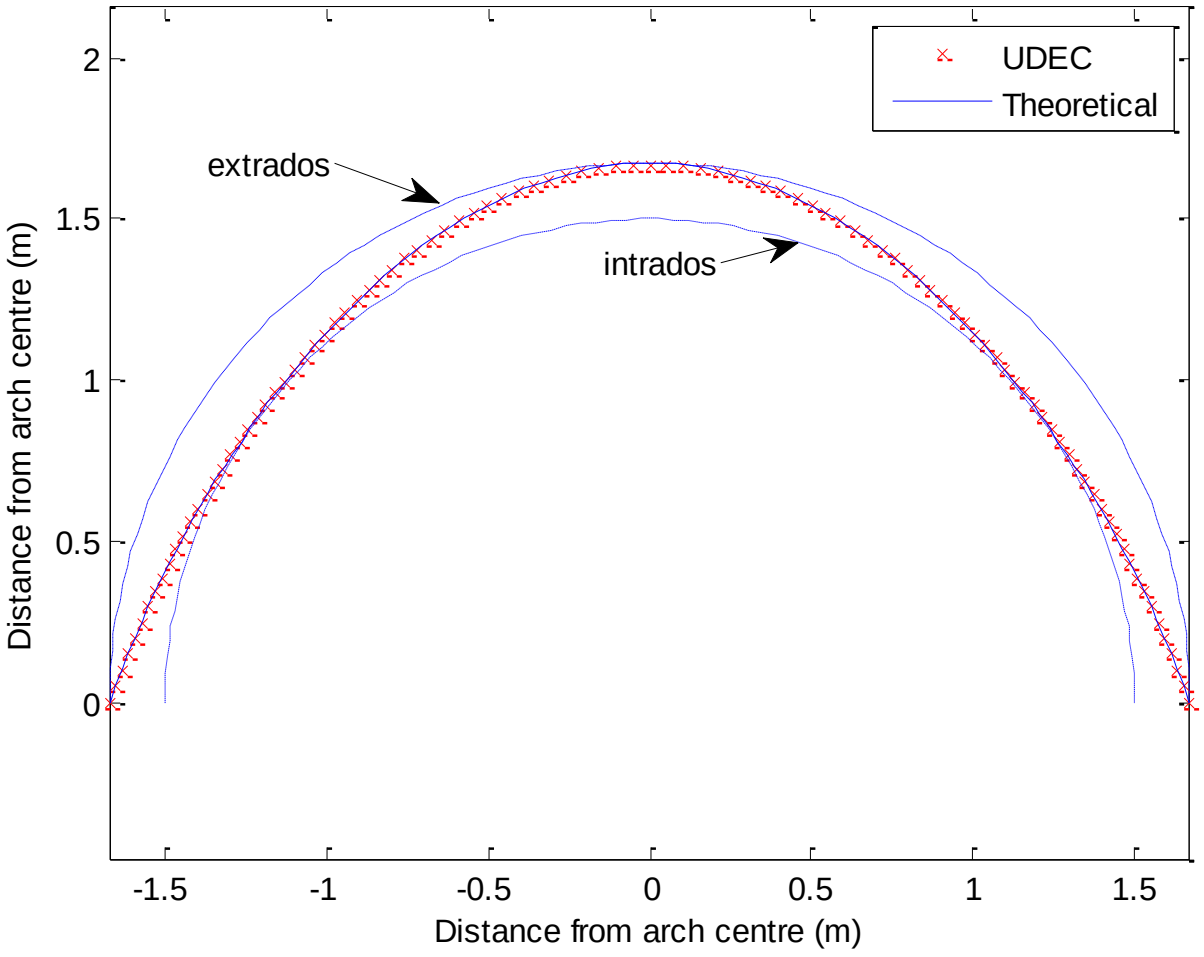

Figure 3.20 – Line of thrust from analytical model

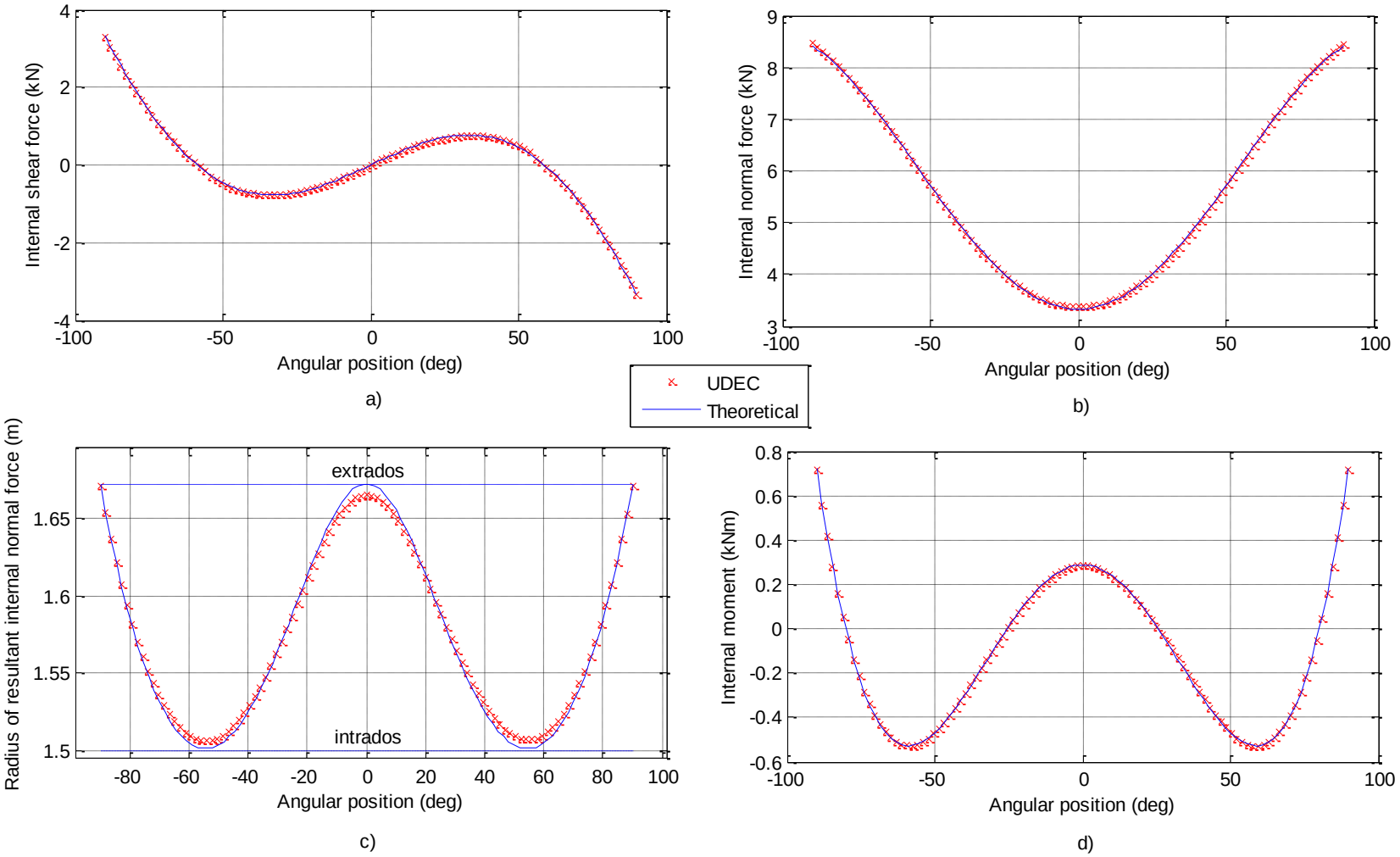

Figure 3.21 - comparison of the internal state of the arch given by the UDEC and theoretical models.
a) Internal shearing forces (S). b) Internal normal forces (N) c) Radius of line of thrust w.r.t. angular position(r).
d) Internal moment ($N.(r-R)$)

3.3.5 Experimental Validation

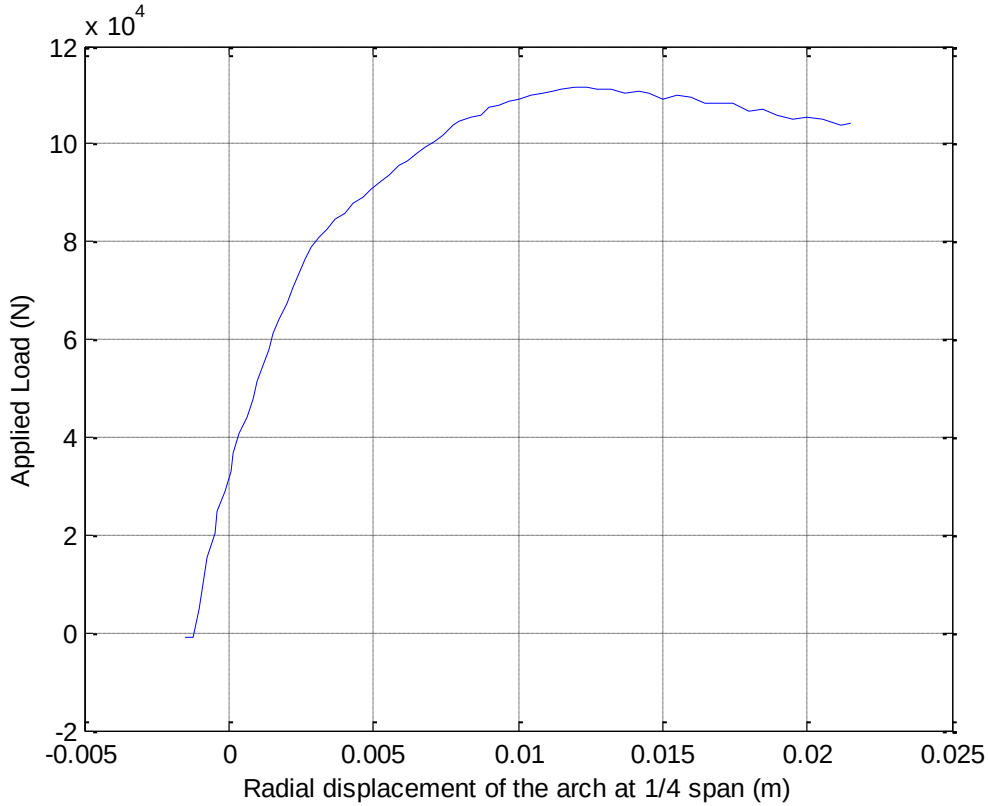

Figure 3.22 – Load vs Arch displacement at quarter span for test EP3 PH3

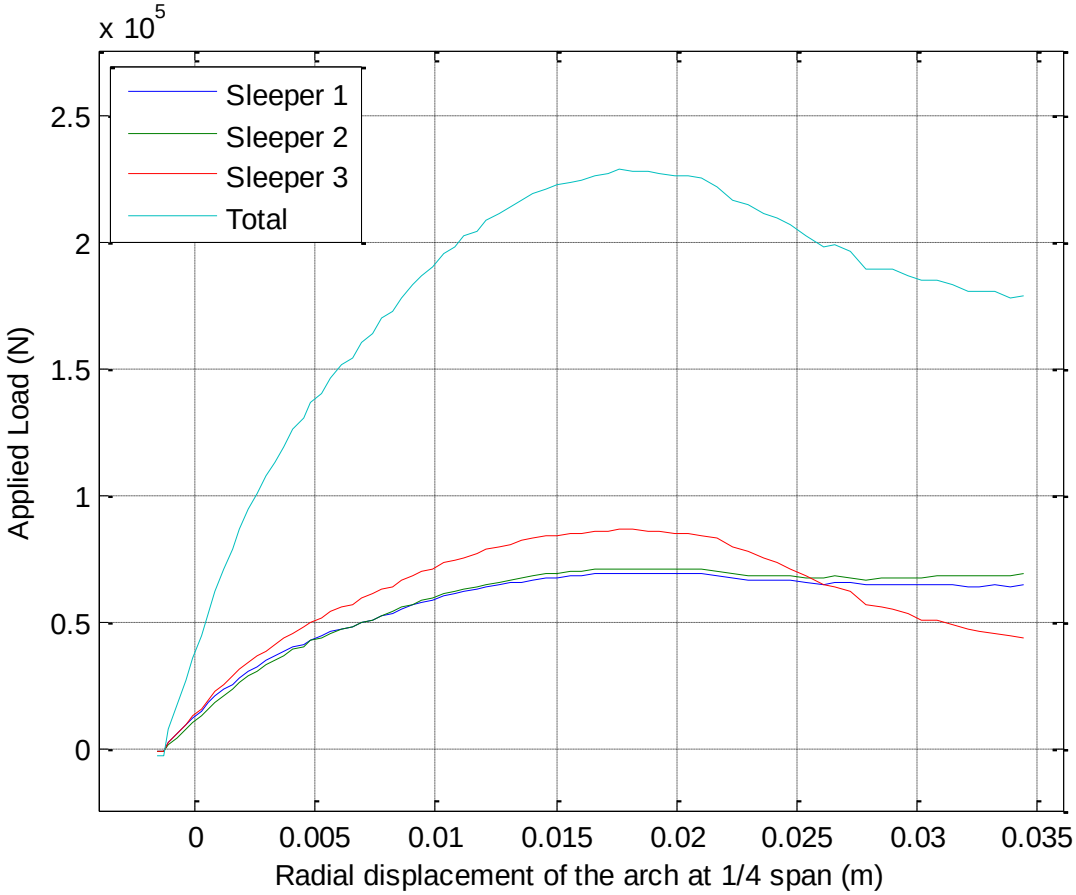

Figure 3.23 – Load vs Arch displacement at quarter span for test EP3 PH3

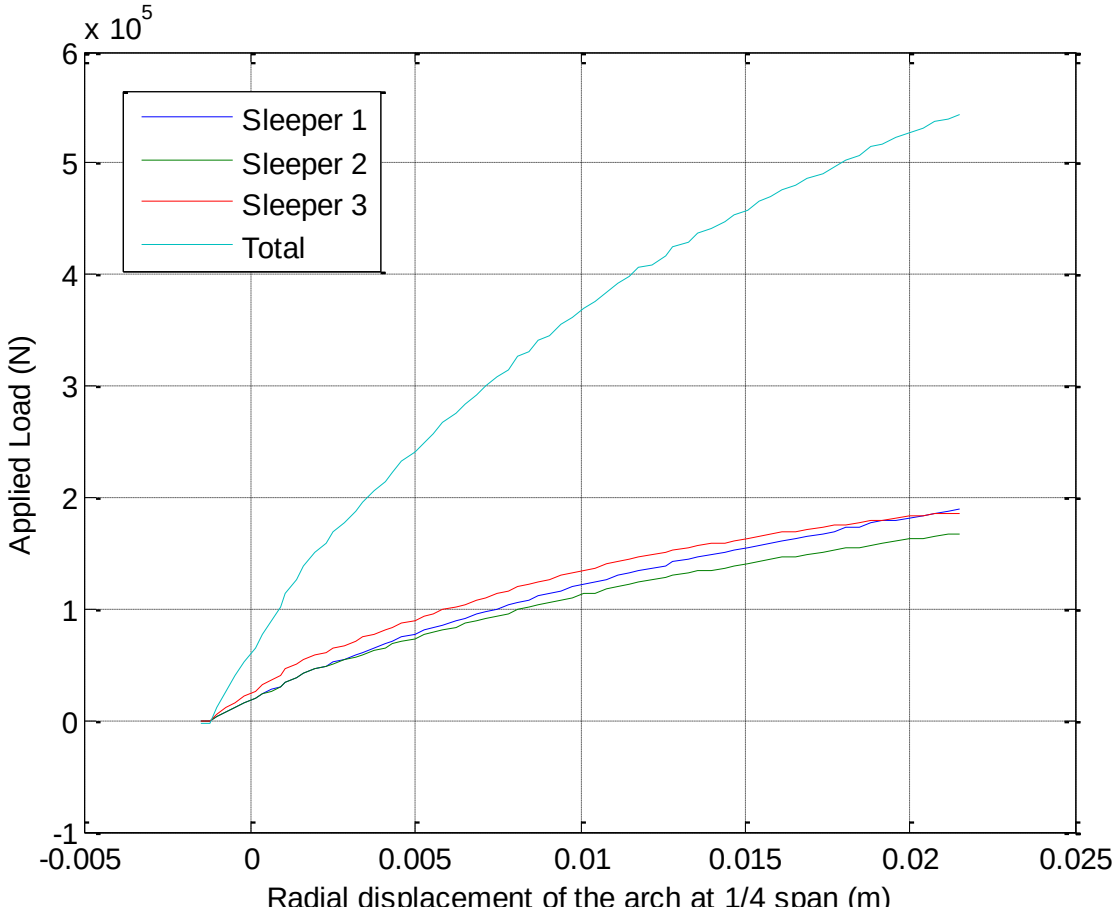

Figure 3.24 – Load vs Arch displacement at quarter span for test EP3 PH3

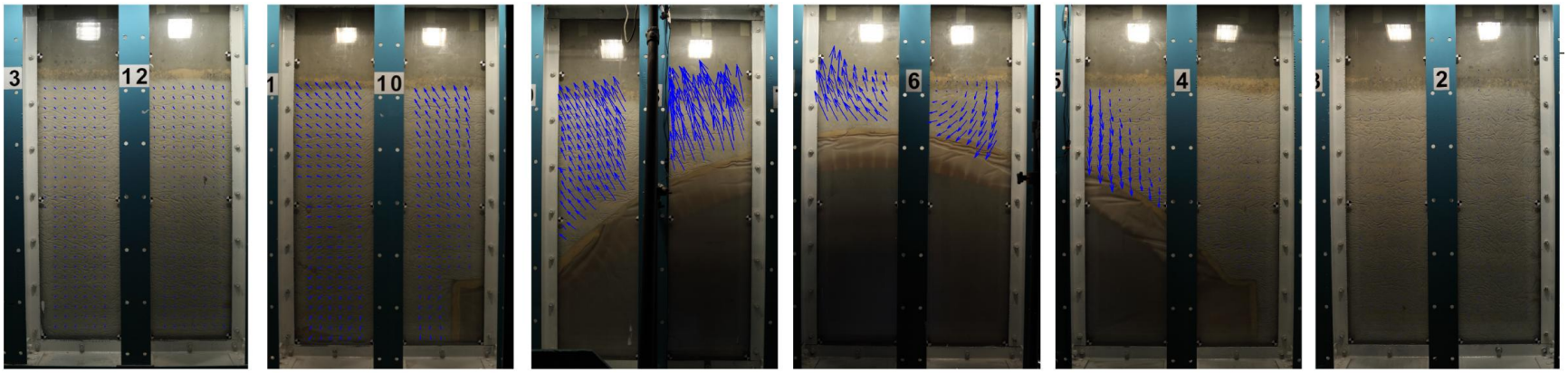

Figure 3.25 – PIV results from the physical model during EP1

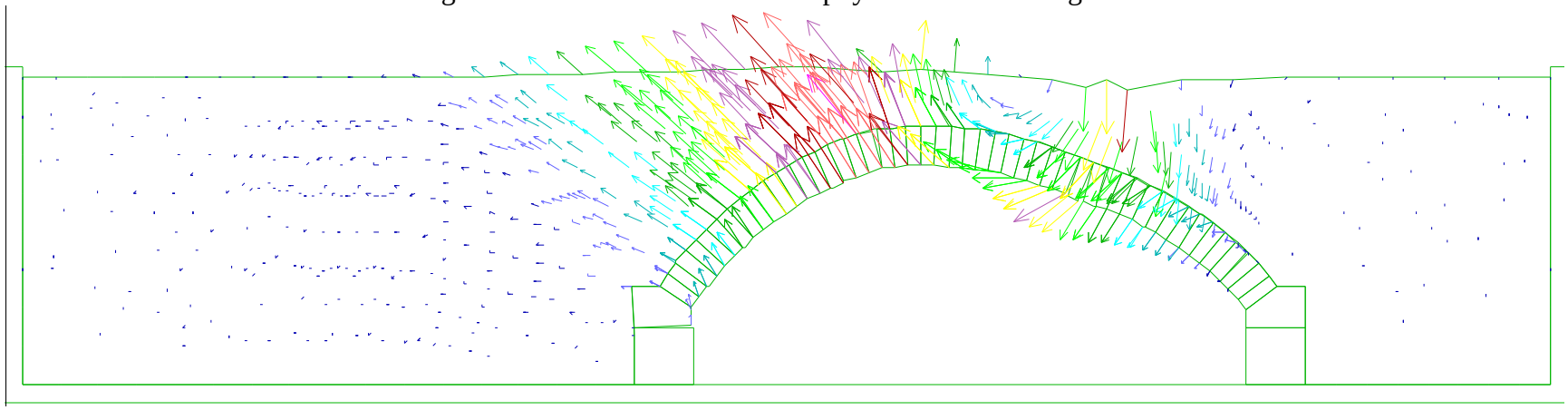

Figure 3.26 – Displacement vectors from UDEC simulation of EP1

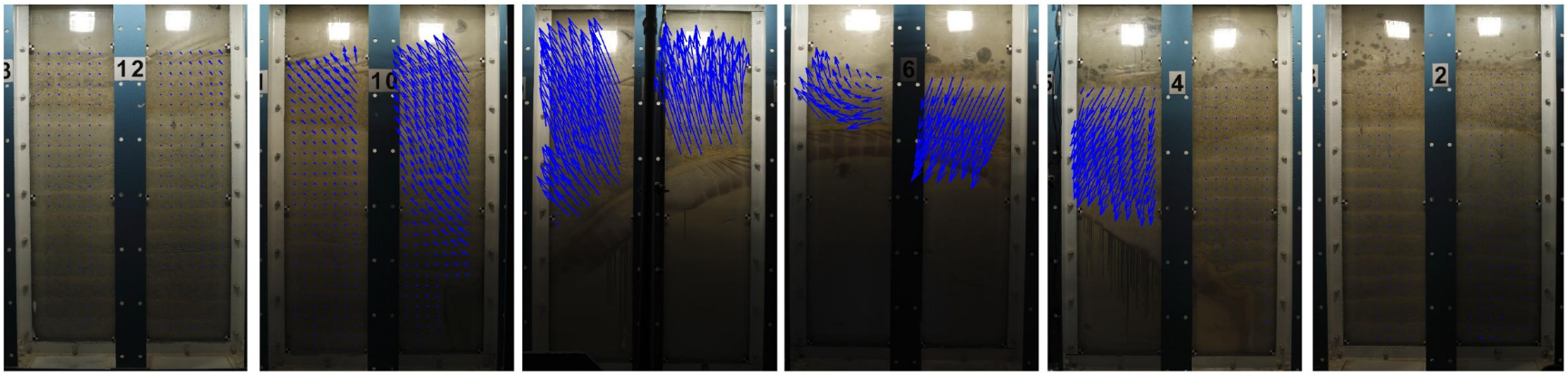

Figure 3.27 – PIV results from the physical model during EP3 PH3

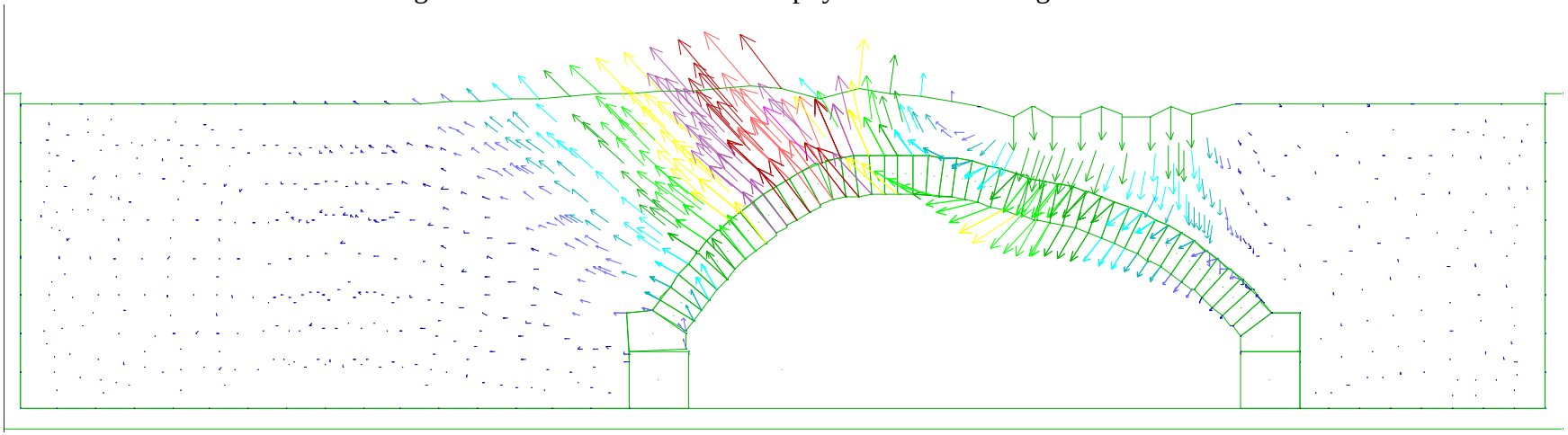

Figure 3.28 – Displacement vectors from UDEC simulation of EP3 PH3

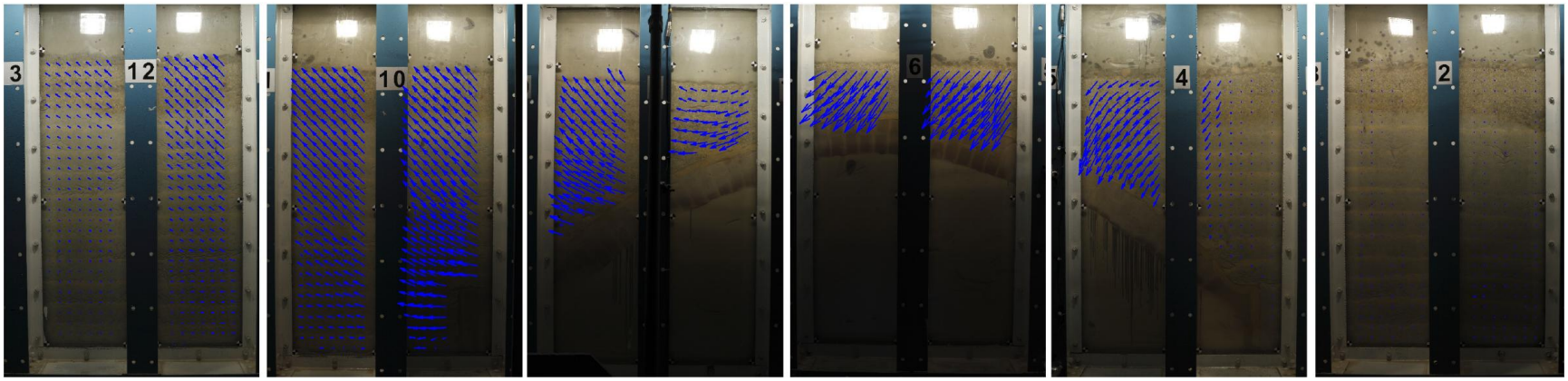

Figure 3.29 – PIV results from the physical model during EP3 PH1

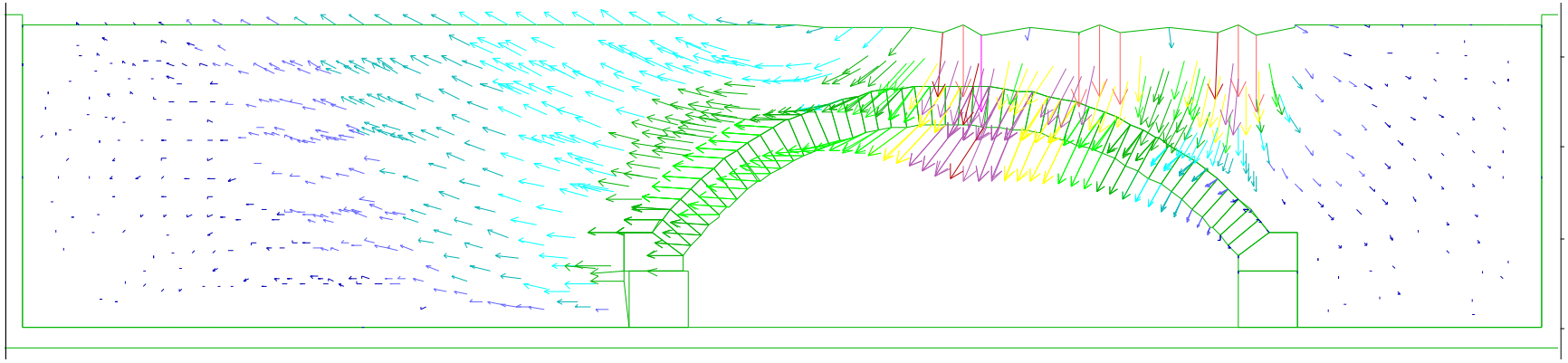

Figure 3.30 – Displacement vectors from UDEC simulation of EP3 PH1 or PH2

3.3.6 Parametric Studies

3.3.6.1 Fill Dilatancy

Although the angle of dilation was not obtained through laboratory testing, an indication from the vertical and horizontal displacements during the Direct Shear box tests was of approximately 5°. However from the parametric study of this property for EP1, the system capacity appears to reach a limit at and angle of 20°, after which increasing the dilatancy does not increase the capacity. This limiting capacity is actually closer to the experimental capacity observed in EP1.

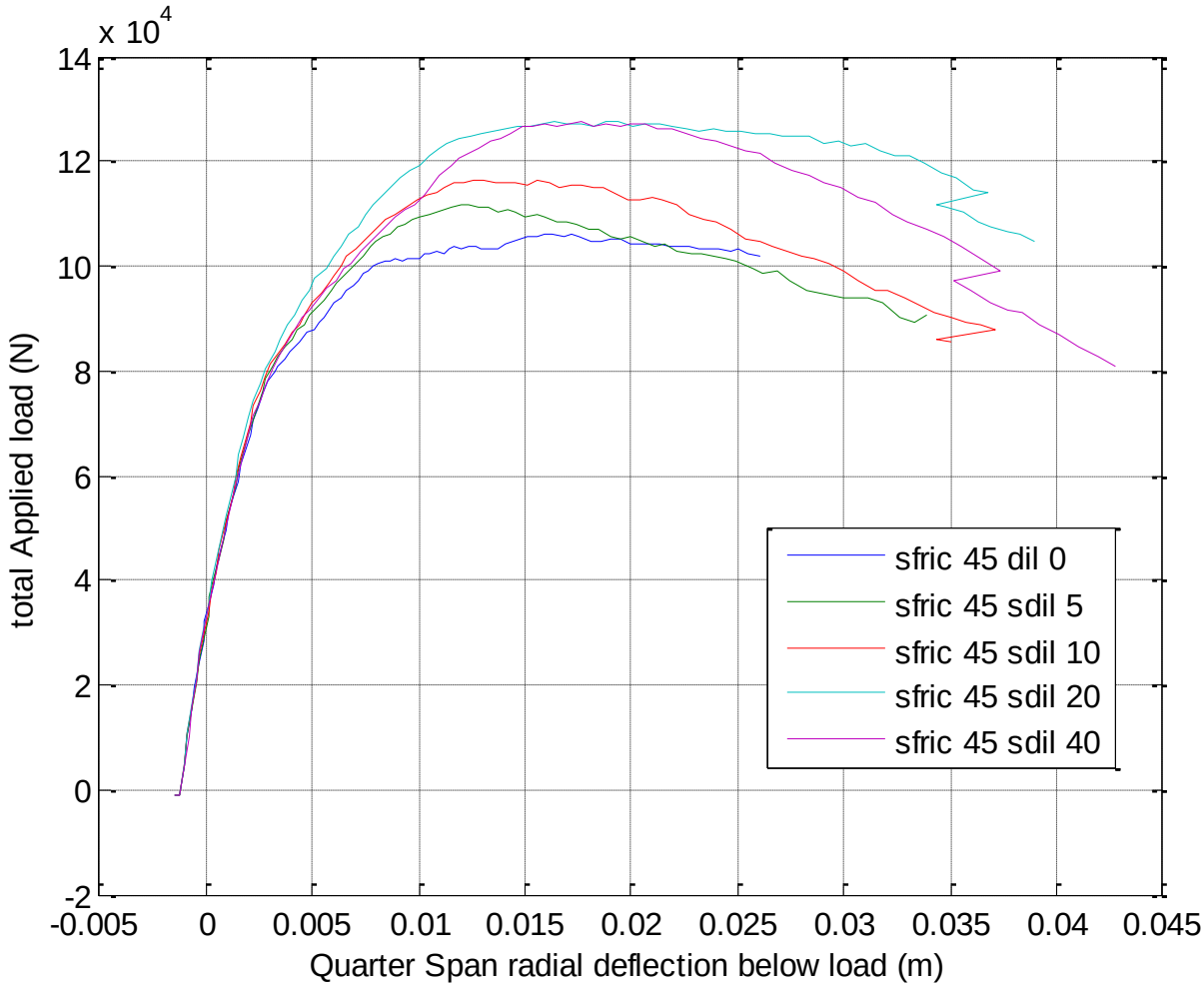

Figure 3.31 – Effect of fill dilatancy on the system load bearing capacity

3.3.6.2 Internal angle of friction of the fill

As the masonry arch element was modelled by the rigid-block assumption, the two most influential material parameters affecting the arch-fill interaction were considered to be the internal soil friction and the coefficient of friction at the arch-fill interface. The results for internal soil friction angle and extrados friction are shown in Figure 3.32 and Figure 3.33 respectively.

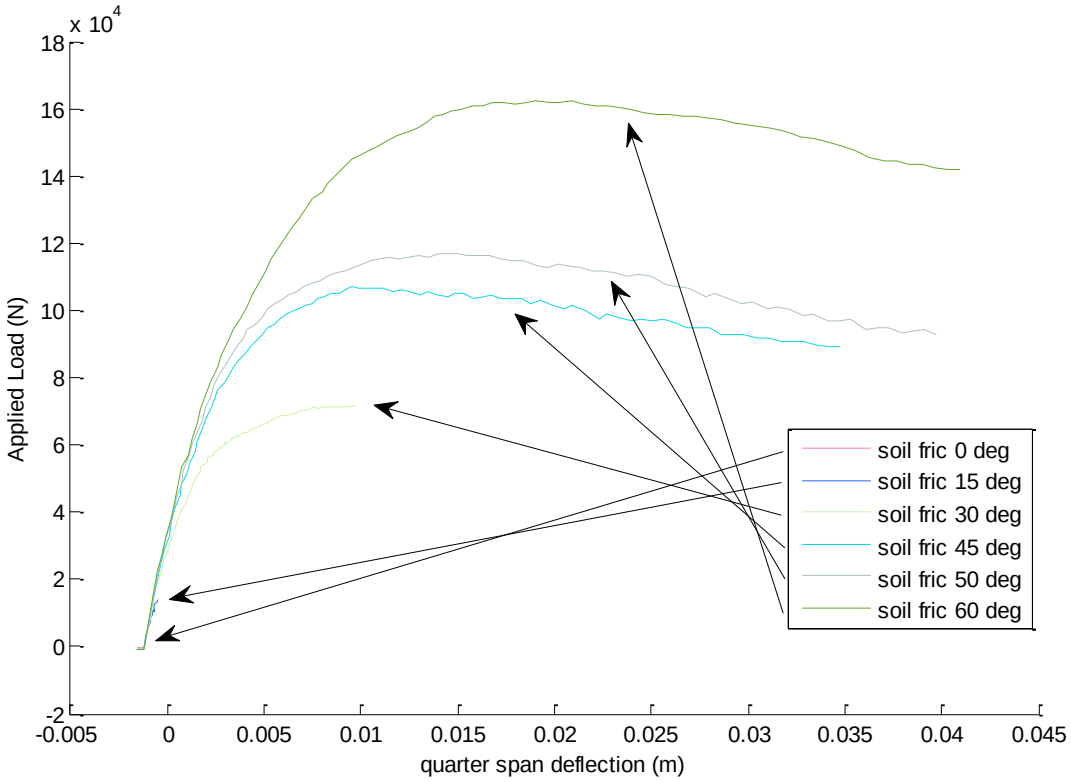

Figure 3.32 – Influence of internal angle of soil friction on the soil-arch interaction in the UDEC model

From the results of the study of the influence of internal soil friction, it is apparent that the graphs of the lower angles of friction terminate early. The cause of the is explained in detail in §**Error! Reference source not found.** where it is demonstrated with plots of UDEC kinematics

for various angles of soil friction. This is that for lower angles, the bearing capacity of the fill surface is reached before sufficient destabilising stress can reach the arch in order to cause a mechanism. The 45 and 50 degree results are very similar, followed by a dramatic increase from 50 to 60.

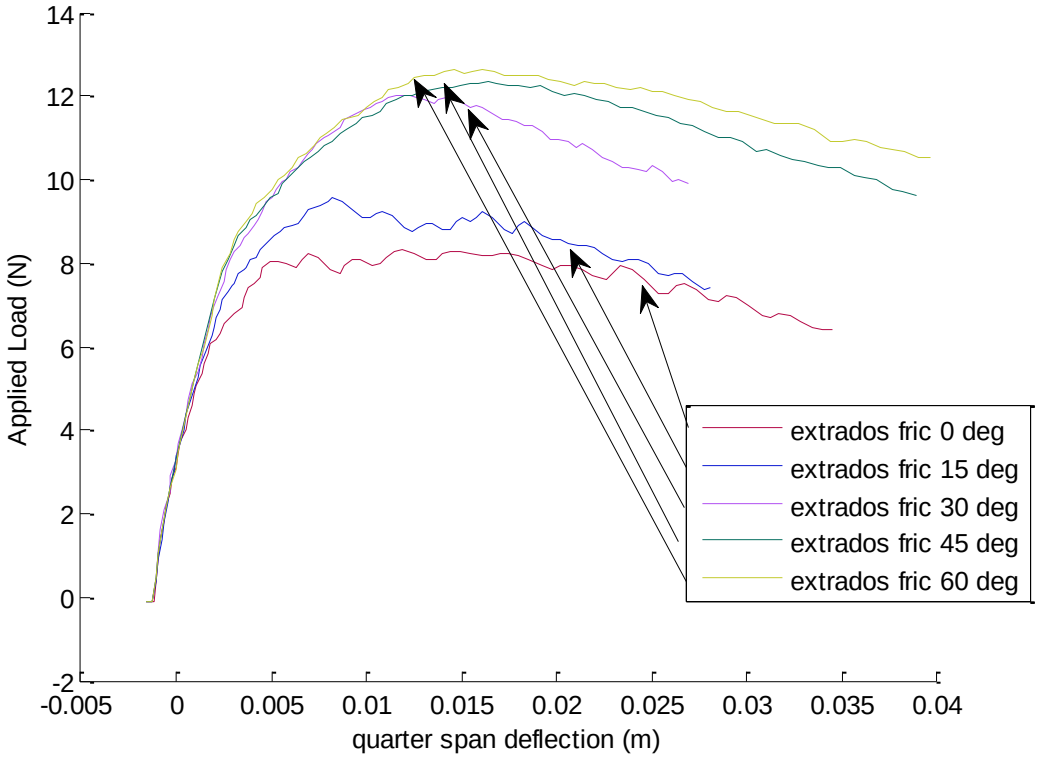

Figure 3.33– Influence of interface angle of friction on the soil-arch interaction in the UDEC model

From the results of the extrados interface friction angle it is clear that there is a limiting behaviour around 45 degrees. Higher angle of friction do not appear to result in any significant increase in capacity beyond 45 degrees. These is also a clear separation in behaviour between 0 – 15 degrees and 30 – 60 degrees. This is likely to be due to a change in behaviour from slip to stick, based on the loading and geometry of the model.

Chapter 4 Theoretical Modelling

4.1 General approach

The general approach adopted in the present section is of primary importance to the thesis and forms the core logic behind theoretical contributions of the present research.

Consider a two-dimensional system of the type illustrated in Figure 4.1. The applied load $q(x)$ may be any vertical pressure distribution, which may be expressed as a one-dimensional function of the abscissa x and contributes to the pressure distribution $p(\theta)$ over the arch extrados.

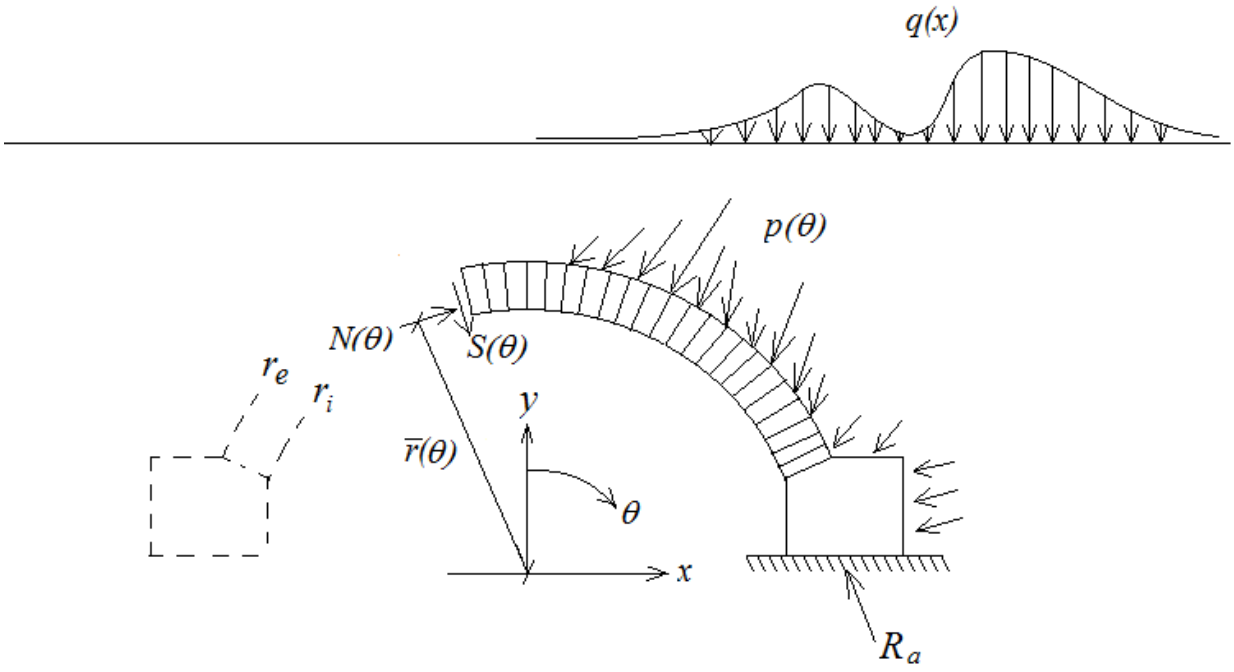

Figure 4.1 – Variables associated with the general model

4.1.1 Transmission of the surcharge to the arch-fill interface

The arch-fill interface or extrados profile will be some shape, typically a curve that may be defined in polar coordinates by $r_e(\theta)$, where r_e is measured from a central point and is in general a variable dependant on θ. If $\theta = 0$ at the crown, this shape would be defined over some angular interval $\Omega_1 \leq \theta \leq \Omega_2$ that spans from one abutment to the other. For an arch of constant radius of curvature, i.e. a circular segment, $r_e(\theta) = constant$.

$q(x)$ will be dispersed through the fill by a particular dispersal function, such as the Boussinesq equations or others of that class. This dispersal function will define the stresses (b_x, b_y) within the fill due to $q(x)$, where $b_x(x, y)$ and $b_y(x, y)$ would generally be two-dimensional functions, such that the pressure acting at some point (x_1, y_1) within the domain of the fill would be a function of two coordinates defining the position of that point, such as x and y.

The dead weight of the fill will also result in pressures (g_x, g_y) within the fill. Apart from the unit weight and depth, these would also generally be dependent on the state of strain within the fill. The aforementioned pressures all contribute to the overall pressures $\vec{p}(\theta)$ with components (σ_x, σ_y) occurring within the fill.

The pressures (b_x, b_y) may then be evaluated over the extrados profile expressed in Cartesian coordinates x_e, y_e . Since the horizontal pressures are dispersed from the location of the applied load, the horizontal component b_x must act in a direction so as to push away from the location of application of the load at the fill surface as shown in Figure 4.2a. This does not necessitate a tensile crack at the extrados where the stresses act away from the arch, the black lines in Figure 4.2b illustrate the orientation of total pressures including the vertical component that may typically occur from a dispersal model.

The orientation of resultant pressures $\overrightarrow{\binom{b_x}{b_y}} + \overrightarrow{\binom{g_x}{g_y}}$ will also be modified by the properties of the arch extrados. For example if the angle of friction at the arch-fill interface is not sufficient for full transmission of some pressures at their incident angles, part of the traction component would be dropped to limit the angle of incidence to the angle friction at the interface. The grey lines in

Figure 4.2b illustrate the resultant pressures if the extrados were completely smooth, i.e. angle of interface friction = 0.

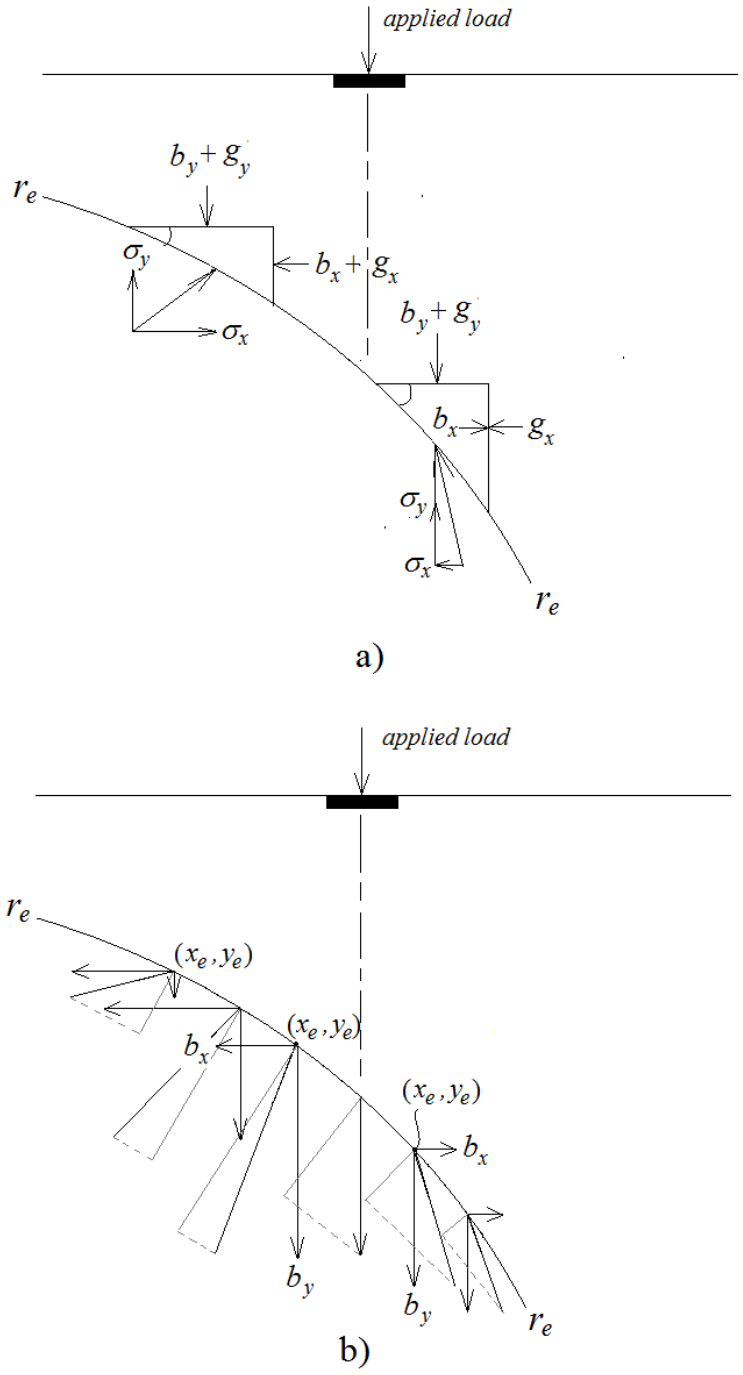

Figure 4.2 – a) Stresses contributing to the stresses acting on the arch extrados b) vertical and horizontal components of area upon which horizontal and vertical components of stress act respectively.

4.1.2 Resultant force due to a region of pressure acting on the extrados

For a segment of the arch over a defined interval $\theta_1 \leq \theta \leq \theta_2$, the resultant force ${}^{\theta_2}_{\theta_1}\vec{P}$ due to pressures acting on the extrados over that interval may be computed as follows:

$$ {}^{\theta_2}_{\theta_1}\vec{P} = \begin{pmatrix} {}^{\theta_2}_{\theta_1}P_x \\ {}^{\theta_2}_{\theta_1}P_y \end{pmatrix} $$

Where:

$$ {}^{\theta_2}_{\theta_1}P_x = \int_{\theta_1}^{\theta_2} \sigma_x . dy \qquad {}^{\theta_2}_{\theta_1}P_y = \int_{\theta_1}^{\theta_2} \sigma_y . dx $$

And:

$$ dx = ds.cos(\theta) = r_e.d\theta.cos(\theta) = y_e.d\theta $$

$$ dy = ds.sin(\theta) = r_e.d\theta.sin(\theta) = x_e.d\theta $$

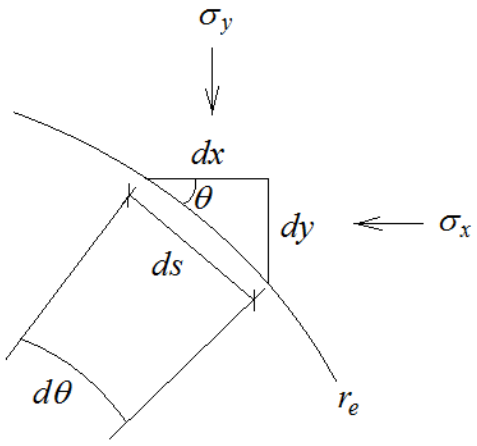

Figure 4.3 – Horizontal and vertical components of area on which vertical and horizontal components of stress act on the extrados respectively.

4.1.3 Line of action of the resultant force due to a region of pressure on the extrados

In order to satisfy rotational equilibrium, the line of action of ${}^{\theta_2}_{\theta_1}\vec{P}$ must pass through the point of intersection of ${}^{\theta_2}_{\theta_1}\vec{P}_x$ and ${}^{\theta_2}_{\theta_1}\vec{P}_y$ as illustrated in Figure 4.4. The orientation of ${}^{\theta_2}_{\theta_1}\vec{P}$ is defined by the respective magnitudes of the two components ${}^{\theta_2}_{\theta_1}\vec{P}_x$ and ${}^{\theta_2}_{\theta_1}\vec{P}_y$ resulting in ${}^{\theta_2}_{\theta_1}\vec{P}$. Thus the angle of ${}^{\theta_2}_{\theta_1}\vec{P}$ measured from the vertical will be simply obtained by $atan\left(\frac{\left|{}^{\theta_2}_{\theta_1}\vec{P}_x\right|}{\left|{}^{\theta_2}_{\theta_1}\vec{P}_y\right|}\right)$, uniquely defining the line of action.

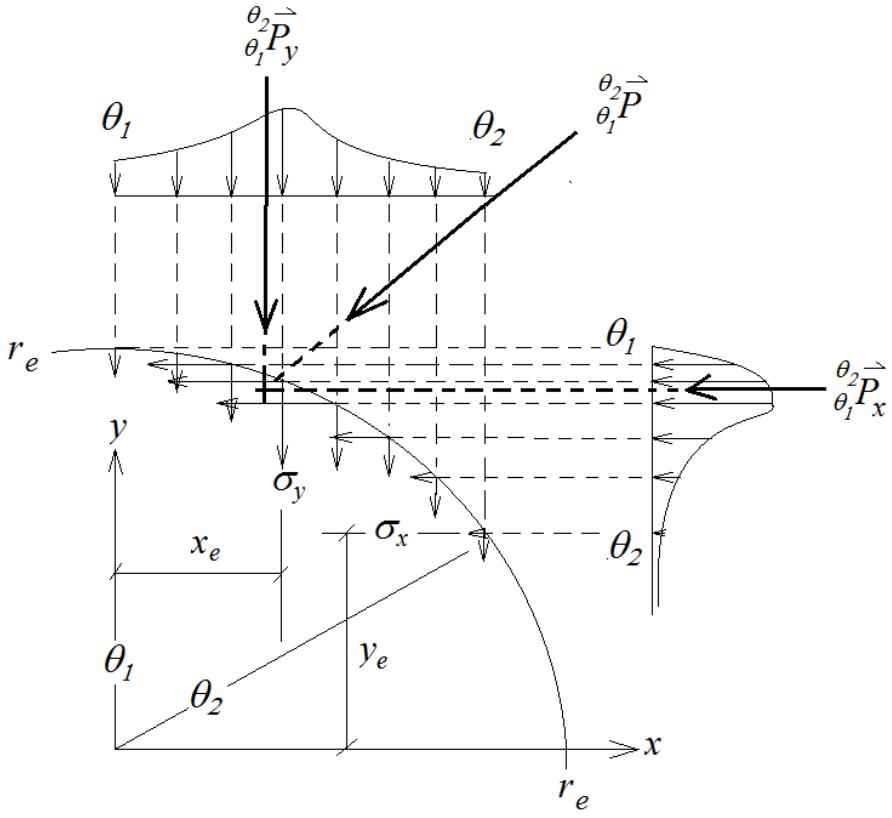

Figure 4.4 – Illustrating the means of identifying the line of action of the resultant force due to pressure acting on a region of the arch extrados

4.1.4 Definition of the Line of Thrust

Consider equilibrium of a thin radial slice of the arch barrel at angular location θ (Figure 4.5a). The compressive stress distribution σ_θ acting normal to the cut exerts a resultant force $N(\theta)$. The radial location $\bar{r}(\theta)$ is the centre of pressure, where the compressive stress profile on one side of the slice could be substituted by a point load of magnitude $N(\theta)$ while maintaining moment equilibrium (Figure 4.5b). The line of thrust in some angular interval $\theta_1 \leq \theta \leq \theta_2$ is then defined as the trace of $\bar{r}(\theta)$ over that interval.

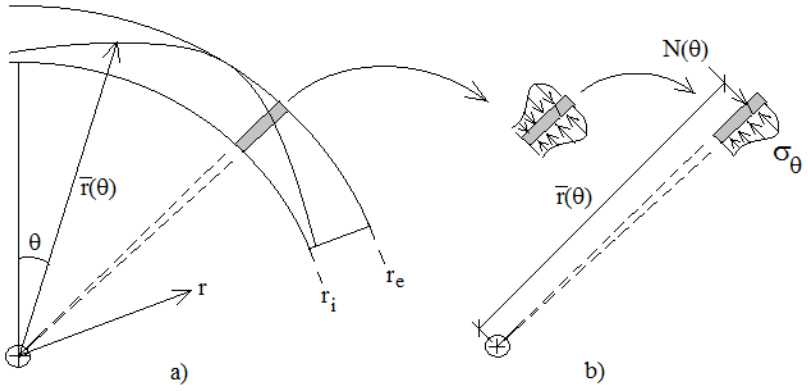

Figure 4.5 – Interpretation of the line of thrust

$$\bar{r} = \frac{1}{N}\int_{r_i}^{r_e} \sigma_\theta . r . dr \qquad (25)$$

4.1.5 Relationship between pressure concentration and geometry of the line of thrust

For any segment $\alpha \leq \theta \leq \beta$ to be in equilibrium, the total force or thrust at the end cross sections $\vec{T}_\alpha$ and $\vec{T}_\beta$ must also intersect at a point ${}^{\beta}_{\alpha}\vec{I}$ that lies along the line of action of ${}^{\beta}_{\alpha}\vec{P}$ (Figure 4.7 a and b). Where ${}^{\beta}_{\alpha}\vec{I} = \begin{pmatrix} {}^{\beta}_{\alpha}I_x \\ {}^{\beta}_{\alpha}I_y \end{pmatrix}$.

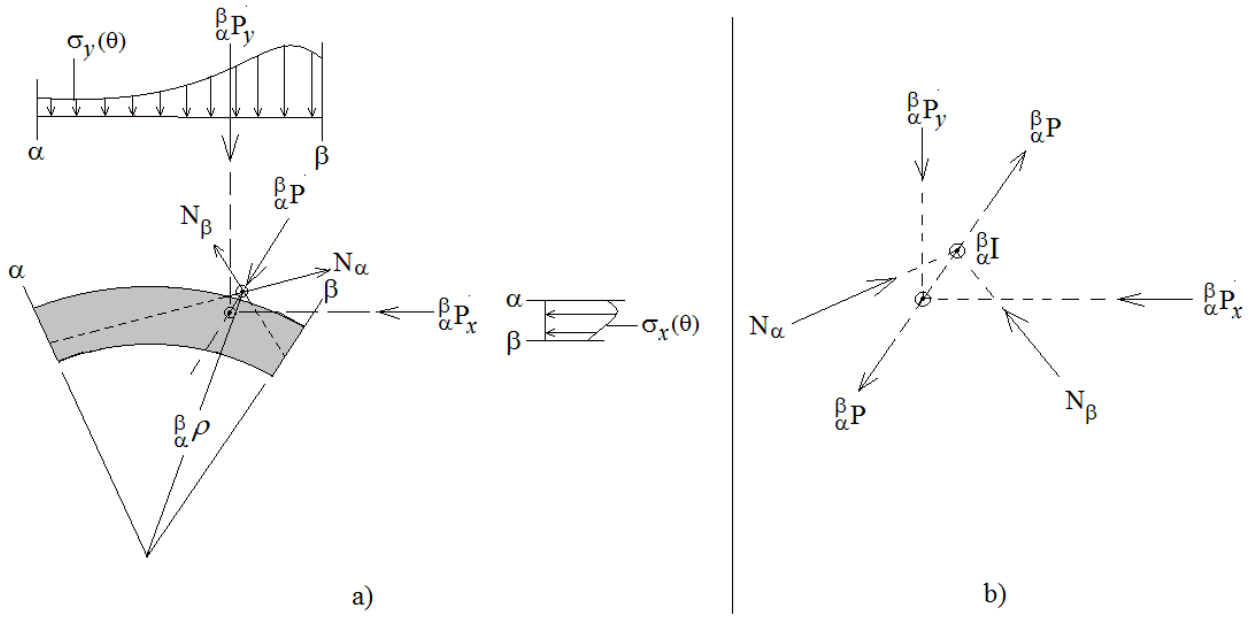

Figure 4.6 – Illustrating the geometric derivation of the location of the line of action of ${}^{\beta}_{\alpha}\vec{P}$ from, $\sigma_x(\theta)$ and $\sigma_y(\theta)$

The angular position of the radius from the arch centre passing through ${}^{\beta}_{\alpha}\vec{I}$, measured clockwise from the crown is defined as ${}^{\beta}_{\alpha}\rho = atan\left(\frac{{}^{\beta}_{\alpha}I_x}{{}^{\beta}_{\alpha}I_y}\right)$, or simply ρ for the present discussion.

If the two segments either side of ρ are considered, $\alpha \leq \theta \leq \rho$ and $\rho \leq \theta \leq \beta$ (See Figure 4.7), they must each be in equilibrium with T_α and T_β respectively as well as the thrust, T_ρ at their mutual interface ρ. For each of these segments to satisfy rotational equilibrium, the thrust either end of each segment must intersect at a point along the line of action of the forces on their extrados, i.e. T_α and T_ρ must intersect at a point along ${}^{\rho}_{\alpha}\vec{P}$ and T_ρ and T_β must intersect at a point along ${}^{\beta}_{\rho}\vec{P}$ respectively.

This implies that in order for forces on each of the two sub-segments to be concurrent, the line of action of the thrust T_ρ at ρ must pass through both of the aforementioned intersection points as indicated by the tangent to the line of thrust at ρ in Figure 4.7a. As $p(\theta)$ becomes more concentrated, by definition ${}^{\rho}_{\alpha}P$ and ${}^{\beta}_{\rho}P$ become closer to ${}^{\beta}_{\alpha}P$ until $p(\theta)$ reaches a singularity at ρ

and becomes a point load of magnitude P, described in Figure 4.7c as the product of P and the Dirac Delta function at ρ.

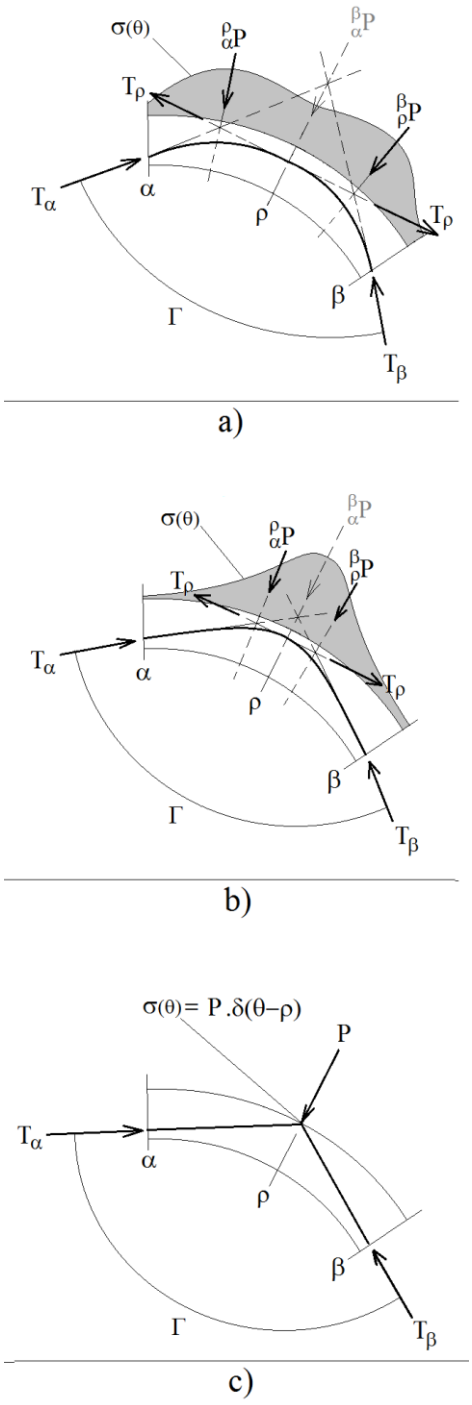

Figure 4.7 – Illustrating the relationship between extrados pressure concentration on the line of thrust.

4.1.6 Criteria for failure mechanisms in the longitudinal plane

In order for the arch-fill system to lose stability, a mechanism must be formed whereby indefinite or excessive displacement of the supported loads is able to occur without further increase in the applied load.

It is recognised that the masonry from which the arch is constructed will be of finite strength, however the present theoretical model does not directly include the effects of masonry crushing. The effects of crushing may be accounted for to some extent by assuming a reduced arch thickness based on a particular constitutive model. However this would not account for the additional moment resistance that would be introduced due to the existence of a zone of plasticity where material strength is exceeded, rather than simple rigid hinge rocking about a point of contact. The scheme by which the thickness reduction would be determined would depend on the constitutive crushing model adopted that defines the stress distribution in the arch cross section where material is expected to yield in compression. Also, tensile strength of mortar joints is not explicitly accounted for. Therefore in the present theoretical model, masonry joints are free to open and undergo rigid body rotation if permitted by external forces. Thus the present theoretical model is limited to two modes of rigid body failure within the masonry, i.e. rotation and sliding.

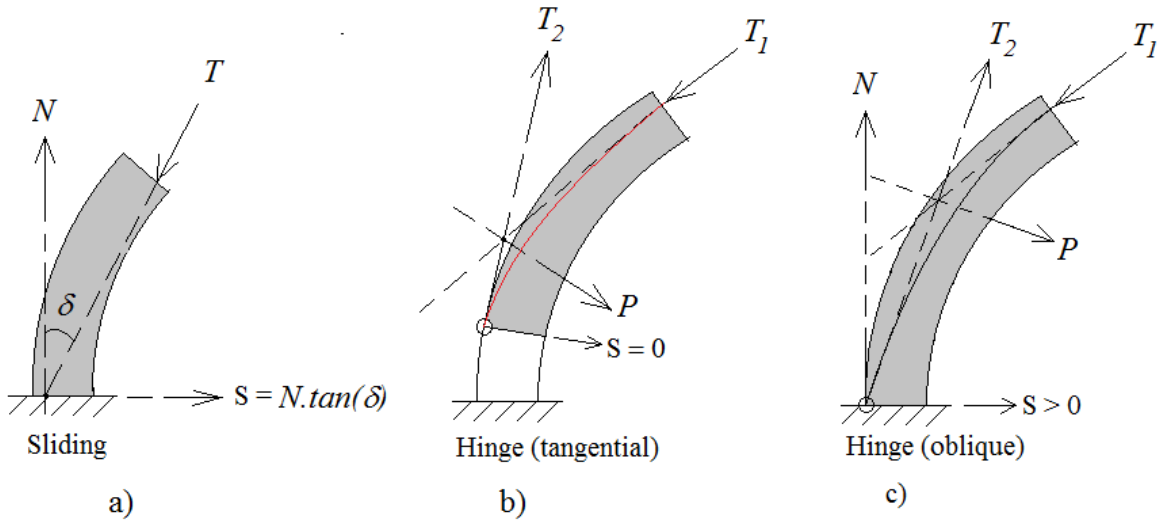

Figure 4.8 – Two modes of masonry failure under the rigid block, no bond strength model. a) Frictional sliding. b) Hinged rotation

In order for frictional sliding to occur, the thrust T passing through the masonry element must intersect a fixed boundary at an angle equal to the angle of friction of the interface of the masonry with that boundary as illustrated in Figure 4.8a.

In order for rotational failure to occur within the masonry when modelled as perfectly rigid, a limiting equilibrium condition must be reached for incipient rotation about an edge. Since the masonry is modelled as having no bond strength, this hinge may occur anywhere in the masonry arch dictated purely by external restraining forces acting on that segment..

In the case of masonry arch bridges, these restraining forces would be resistance from the fill acting on the extrados and self weight of the masonry. These forces are generally distributed, i.e. these would act over a finite area. Therefore the trajectory of the line of thrust, which represents internal forces and is consequential to external forces, would change gradually depending on the pressure concentration as described earlier with reference to Figure 4.7.

In order for the thrust to be transmitted by the masonry material to the fixed abutments, the line of thrust must remain within the masonry. Therefore if the line of action of the thrust at one end of a segment is not parallel to the thrust at the other end of the segment, the external force on the extrados must equilibrate these, acting through their intersection point as illustrated in Figure 4.8b. In order for the line of thrust to intersect the extrados or intrados while remaining within the arch, a turning point must occur in the line of thrust with respect to θ, such that: $\frac{dr}{d\theta} = 0$.

In order for the line of thrust to intersect the extrados or intrados obliquely, an instantaneous turning point, i.e. a discontinuity in $\frac{dr}{d\theta}$ would be required at the point of intersection to divert the line of thrust such that it remains within the arch. This would require a point load to equilibrate the oblique thrust with an opposing thrust tangential to the arch as illustrated in Figure 4.8c. Such a point load may occur in the form of the shearing reaction at a fixed abutment. This shearing force may either be sufficient or insufficient but cannot be more than sufficient. This implication of the latter statement is that this point of contact may either slide or support rotation but the line of thrust cannot be diverted by a greater angle than that required to make it tangential to the arch, i.e. normal to the radial cross section or joint.

4.1.7 Masonry Arch failure mechanisms in the longitudinal plane

Under asymmetric loading considered in the present research, two primary types of failure mechanism, or a combination thereof, may occur in the longitudinal plane under the aforementioned modelling constraints. These are illustrated in Figure 4.10.

Common to both of these mechanisms is the formation of hinges 1, 2 and 3. The location of these three hinges will be dependent on the pressure distribution acting over the region $\alpha \leq \theta \leq \beta$.

An arch consisting of only three hinges is stable, i.e. cannot escalate to a failure mechanism without formation of a fourth hinge, abutment spread or material failure.

For a three-hinged system consisting of two segments, if no more than one of the end hinges are of the oblique type, described in the previous section (Figure 4.8) then the system will also be statically determinate as shown in Figure 4.9.

The existence and/or location of the fourth hinge will be dependent on the location of the hinge 3 and the magnitude and position of the pressure distribution over the region $\beta_2 \leq \theta \leq \alpha$.

Here β_2 is where the line of thrust intersects the interface between the masonry structure and the fill and $\beta_2 \leq \Omega_1$, where Ω_i is the angular location where the interface intersects a fixed boundary.

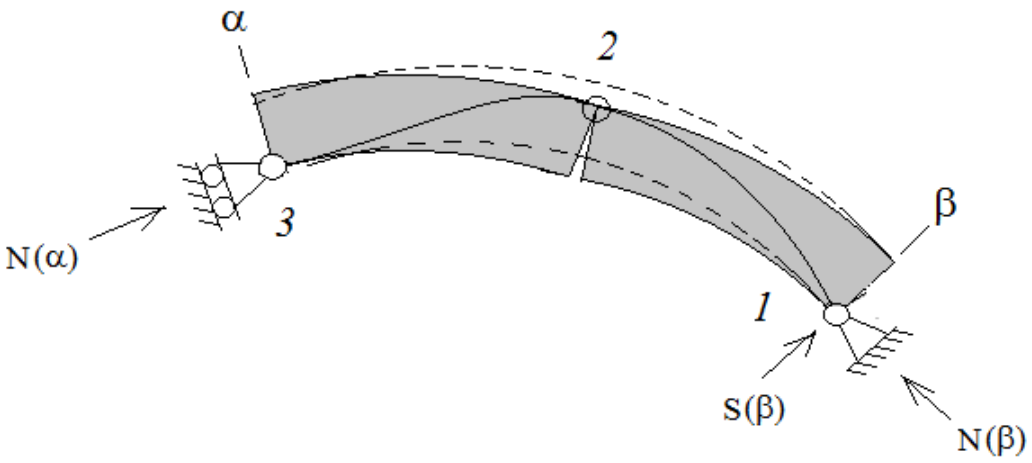

Figure 4.9 – Illustrating a statically determinate three hinged system

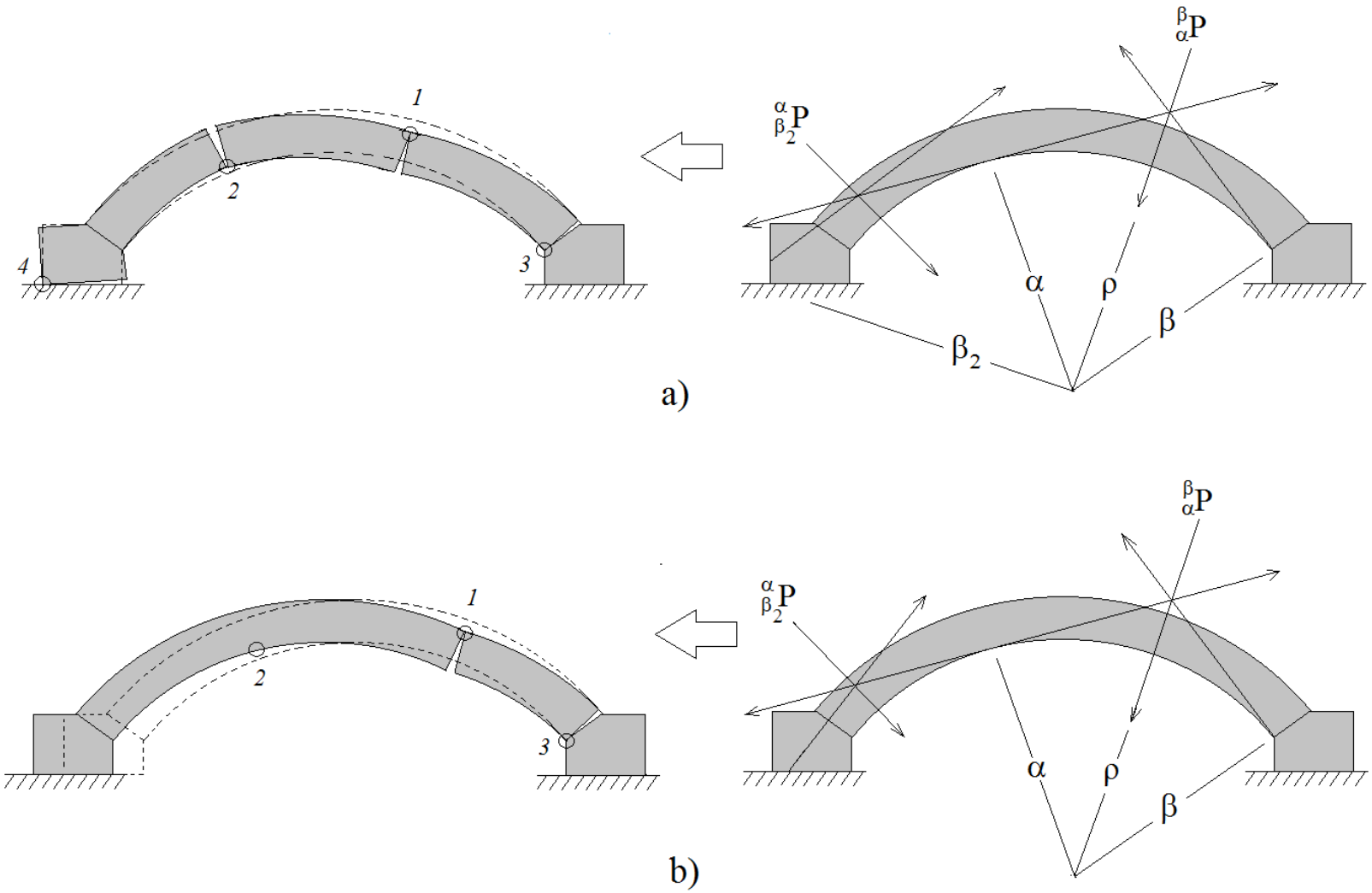

Figure 4.10 – The two primary types of failure mechanism that may occur in the longitudinal plane under asymmetric loading. a) Four-hinged rotation. b) Three-hinged spread

4.1.8 Distinction between destabilising pressures and stabilising pressures

In the previous section, the pressures acting in the arch were divided into distinct regions related to the failure mechanism of the arch, particularly hinge locations. In the present section another important distinction if made related to the causality of pressures.

In the failure mechanisms described in the previous section, part of the arch displaces away from the fill and part of the arch displaces towards the fill. This is illustrated more clearly in the semicircular arch in Figure 4.11. Where the arch displaces away from the fill, the scalar product of pressure exerted on the arch from the fill, with respect to the velocity of the arch-fill interface, will assume a positive value. Where the arch displaces toward the fill, this scalar product would assume a negative value.

The region of the arch extrados on which the aforementioned scalar product has a positive value, will be a region of destabilising pressure. Pressures on this region do work to cause displacement. The region on which the scalar product is negative, will be a region of stabilising pressure. Pressures on this region do work to arrest displacement and themselves arise as a result of displacement.

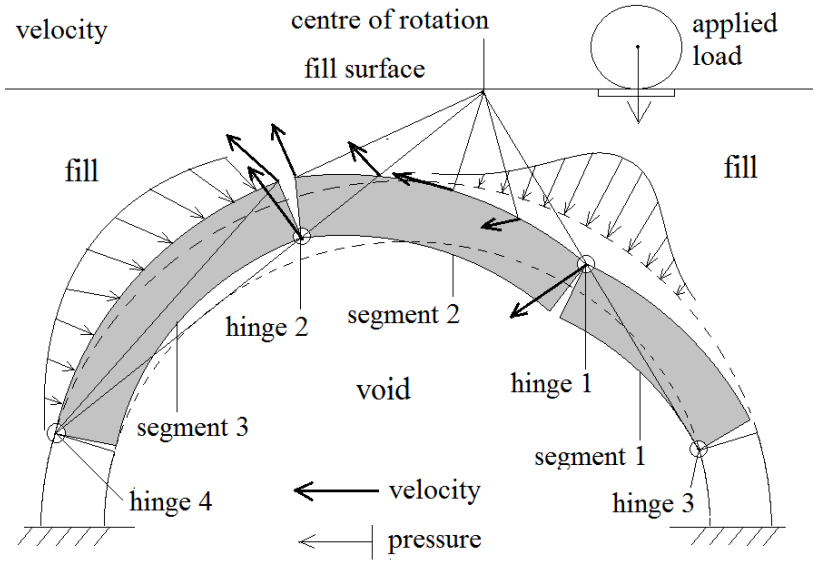

Figure 4.11 – Illustrating the respective directions of pressure from the fill and velocity of the masonry interface, distinguishing destabilising from stabilising pressures in a four-hinged rotational failure mechanism.

4.1.9 The boundary between destabilising and stabilising pressures

From the previous section it is apparent that under the rigid, non-tensile assumption, the locations of the hinges define the centres of rotation of the segments between them. Of particular interest is that of segment 2. On this segment the scalar product of the velocity changes sign with respect to the normal to the arch extrados. For a smooth arch, where no traction component would be transmitted at the interface, all pressures would act normal to the arch extrados. Therefore for a smooth arch extrados, it is apparent from Figure 4.12 that the unique line at angular position η passing through the centre of rotation of segment 2 that is also normal to the arch extrados, will mark the boundary between the destabilising and stabilising pressures. In the presence of traction components to the pressures of the extrados, this boundary would occur where the velocity become perpendicular to the total pressure vectors acting on the extrados. This boundary would still be on segment 2 and from practical considerations and numerical simulations as will be discussed in the present section; this boundary would be close to that of the smooth case.

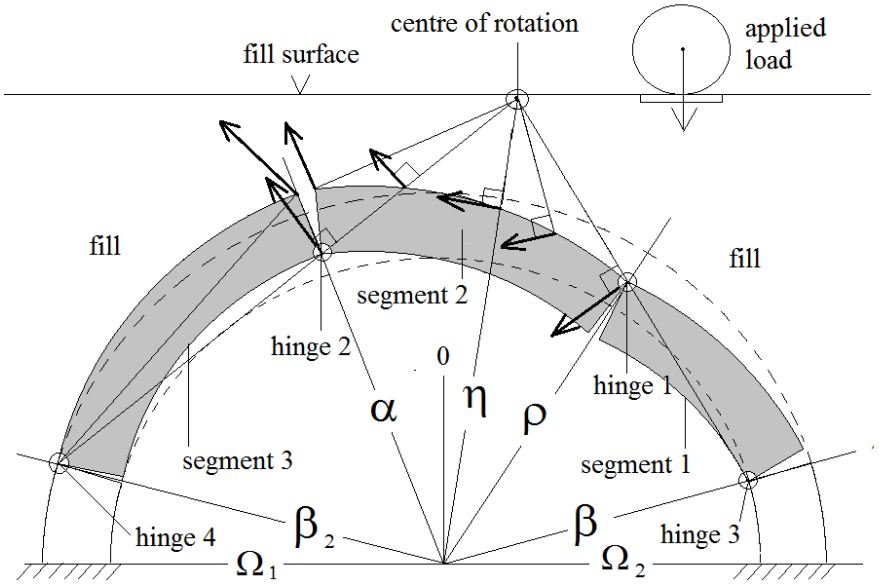

Figure 4.12 – For-hinged rotational sway mechanism with critical angular locations labelled

It is also apparent from Figure 4.11 that the location of the centre of rotation of segment 2 may be deduced directly from the locations of hinges 1, 2, 3 and 4. Namely, it is the point of

intersection between the line drawn through hinges 1 and 3 and the line drawn through hinges 4 and 2. This type of geometric relationship is used in the plastic analysis of steel portal frames when the instantaneous centre of rotation is determined. It is derived from the fact that velocities at all points within the material of a rigid body must instantaneously be perpendicular to the centre of rotation of that body.

4.1.10 Decoupling applied pressures from deformation dependant pressures

In order for an assessment of the ultimate limit state capacity of an arch-fill system to be carried out from statics, sufficient information must be available from the outset to solve the equations of equilibrium. The present section discusses the distinction between applied pressures and deformation dependant pressures.

In addition to dead loads, pressures acting on the arch will in general receive some contribution from the dispersal of live loads and some contribution as a response of the fill to the displacement of the arch. Dead loads and live loads are both based on predetermined, known quantities, such as the pressure profile applied at the fill surface, properties of the fill material and the dispersal model used to compute pressures reaching the arch from the surface. The other contribution to pressures on the arch are displacement dependent. These are unknown from the outset and can only be computed for a known mode of deformation based on a fill resistance model.

Initially, it cannot be assumed that these two contributions to pressures on the arch may be separable and both components may be subject to modification depending on the induced strain state of the fill due to deformation of the system. In retaining wall theory, the latter effect is accounted for by application of lateral earth pressure coefficients, however the active and passive sides of the wall are clearly separated. This is not the case in masonry arch bridges.

Some observations from the physical and numerical modelling results are noted when considering the arch fill system loaded asymmetrically, resulting in the four-hinged rotational sway mechanism. These observations suggest favourable circumstances exist for de-coupling the system by simplifications that may be expected to result in very small discrepancies from the true system. These are set out as follows:

i. The region of fill above segment 2 between α and ρ rotates about the same centre of rotation as the rigid masonry segment between hinges α and ρ. The velocity field above segment 2 is aligned with that of the masonry segment with no discontinuity in the velocity field across the extrados interface on this segment. This suggests no power is dissipated at the interface and the arch does not cause any shear strain on this region of fill but moves in unison with it (e.g. Figure # and Figure #). The fill above segment 2 is separated from the fill above segment 3 because the centre of rotation changes at hinge 2. This causes the velocities at the arch extrados either side of hinge 2 to act away from each other as illustrated in Figure 4.12 such that no shear stress may be transmitted across the fill above hinge 2. Therefore it may be assumed that the shear strength of the fill does not contribute to the pressure acting on segment 2 and pressures on this segment are only due to the dead weight of the fill and pressure reaching it from the applied load. These pressures are thus determinable prior to knowledge of the location of hinge 4. Only the arch beyond α (i.e. segment 3, $\theta < \alpha$) experiences resistance due to mobilisation of shear strength of the fill and the estimated location of hinge 4 will depend on the fill resistance model.

ii. For load cases that are sufficiently concentrated that they have the potential to destabilise the system, pressures from the applied load reaching the arch between α and η are relatively negligible relative to those between η and ρ and are mainly due to the dead load of the fill above which is typically shallow above segment 2. Therefore the approximations shown in Figure 4.13(c) where the angular locations $\rho, \rho_\alpha, \rho_\beta$ of the resultant forces ${}^{\beta}_{\alpha}\vec{P}, {}^{\rho}_{\alpha}\vec{P}, {}^{\beta}_{\rho}\vec{P}$ are estimated by the forces due to the loads reaching the arch ${}^{90}_{0}\vec{P}, {}^{\rho}_{0}\vec{P}, {}^{90}_{\rho}\vec{P}$ respectively (Figure 4.13 (a) and (b)) is reasonably accurate

because the neglected contribution of pressures between α and 0 are very small relative to pressure between 0 and ρ for destabilising loads as discussed above, similarly, the pressure in the region between hinge 3 and the horizontal ($\theta = 90°$) will be very small relative to the pressure over the region $0 \leq \theta \leq 90$ (Figure 4.13 (c, d)).

iii. Hinge α will occur at the unique tangent to the intrados that passes through the point of intersection of the tangent at ρ and the line of action of ${}^{\rho}_{\alpha}\vec{P}$ (Figure 4.13(c)). Hinge β will either occur at the tangent (Figure 4.13 (c)) or at the restrained abutment Ω (Figure 4.13 (d)) whichever of these is closer to ρ. However of primary importance is the location of hinge α as this is the point through which applied loads are ultimately transmitted to segment 3 as described in section 4.1.11.

iv. Numerical modelling of the arch formed of rigid blocks and the fill modelled as Mohr-Coulomb continuum, shows very little variation in the pressure profile and line of thrust in segments 1 and 2 as loading increases. Whereas segment 3 shows significant changes in the pressure distribution, line of thrust and position of hinge 4, which may be attributed to the progressive mobilisation of shear strength of the fill. Figure 4.14 shows a series of superimposed plots from UDEC simulation in which a load applied as a rectangular strip at the fill surface is gradually increased by displacement control. The resulting pressures in the arch extrados and the corresponding lines of thrust through the arch are plotted successively. Pressures gradually increase to a peak capacity. The line of thrust through segments 1 and 2 remains within a narrow band and the intersections with the arch extrados and intrados at hinges 1, 2 and 3 remain a the same positions throughout with only minor fluctuations. In contrast, the line of thrust through segment 3 steadily changes trajectory as loading increases and position of hinge 4 moves from the end on the arch to it's final position significantly further up where it remains as loading increases beyond the peak load. The figure also indicates the location of ρ based on the Boussinesq dispersal model.

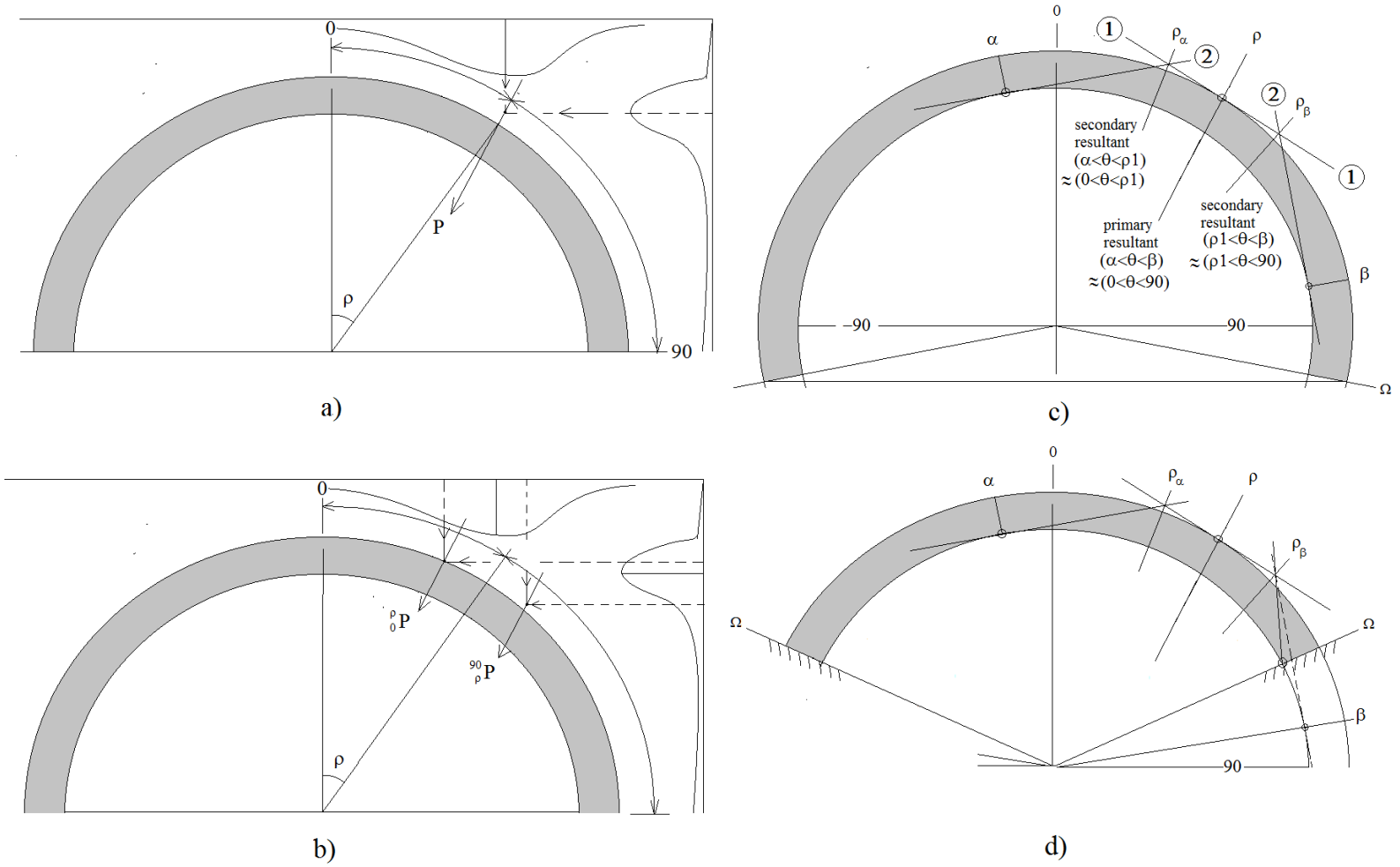

Figure 4.13 – Illustrating the proposed method of decoupling the arch-fill system to facilitate static stability analysis

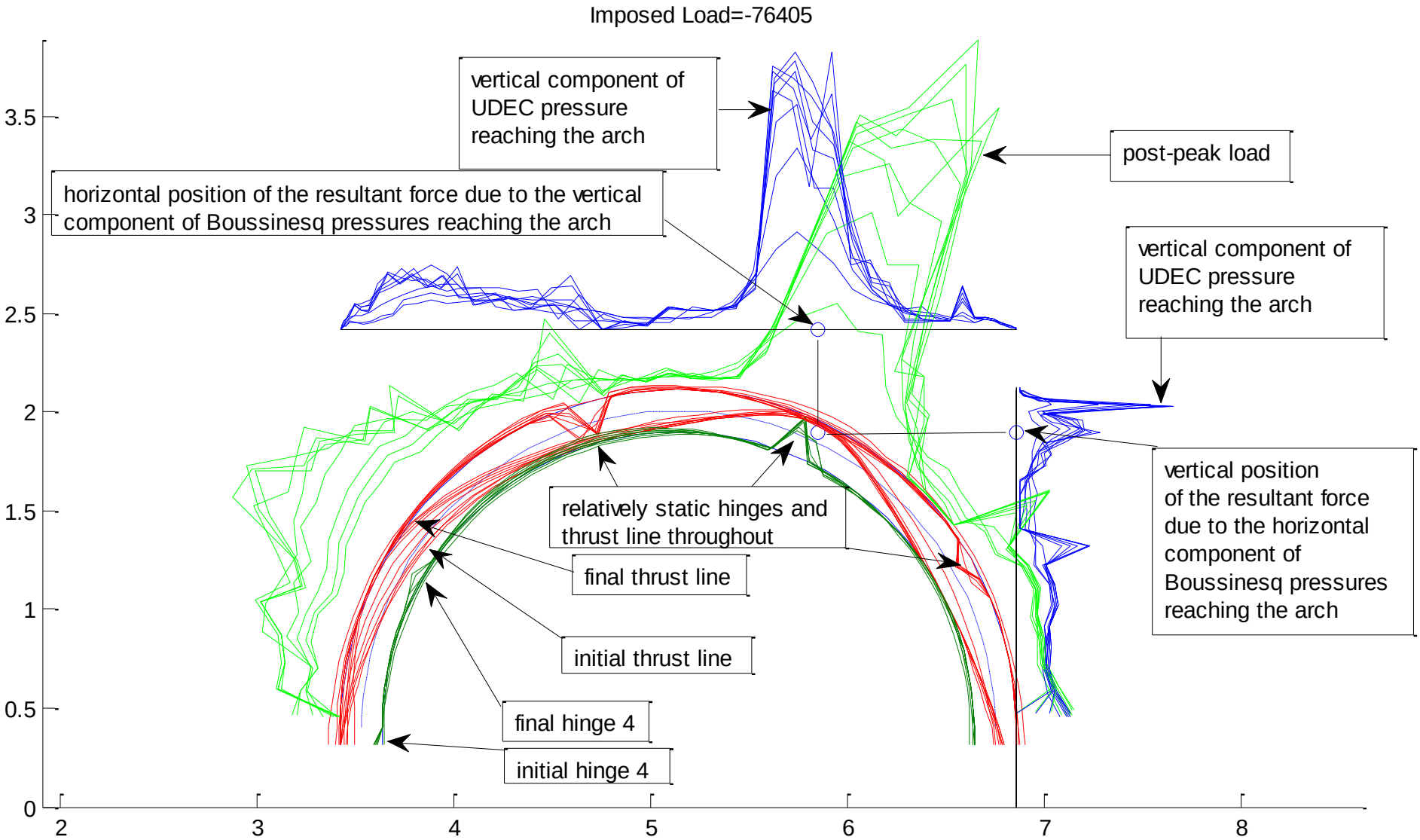

Figure 4.14 – Evolution of external and internal statics. Comparison between the location of the resultant applied pressure obtained from the UDEC model output, with that obtained from the Boussinesq equations,

4.1.11 Analysis of segments 1 and 2 to determine α and $N(\alpha)$

When the applied loading increases in magnitude and concentration, the curvature of the line of thrust over the loaded region of the arch will become more acute as was illustrated in Figure 4.7c. As the magnitude of the applied load increases, this may be equilibrated by the thrust either by increased magnitude of thrust or decrease of the angle Γ in Figure 4.7c. until the line of thrust becomes tangential to the arch intrados at which point hinges are formed. The present model assumes that the arch material is sufficiently rigid that only small strain deformation is required in order for the first three hinges to form. These occur at angular locations ρ at the extrados, α and β at the intrados. Where the locations of α and β would be determined by the method described in the present section. This limiting equilibrium state is illustrated in Figure 4.15.

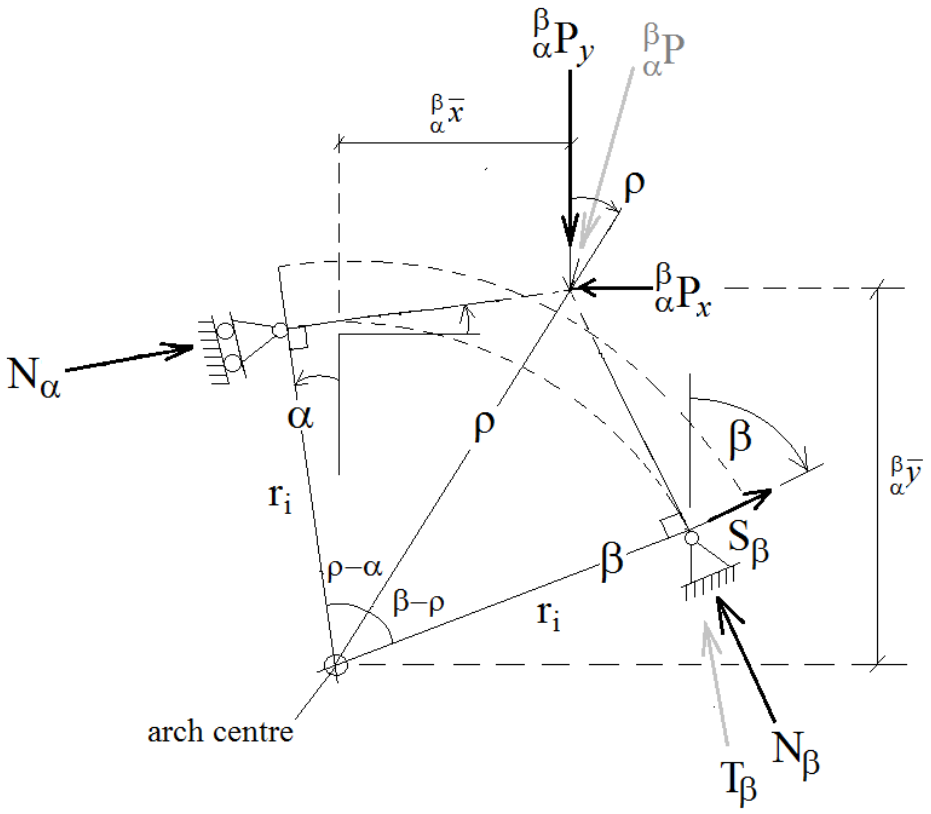

Figure 4.15 – Limiting equilibrium state at the formation of hinges 1, 2 and 3

In this state, N_α, N_β and S_β may be related to $\alpha, \beta, \rho, {}^{\beta}_{\alpha}P_x,\ {}^{\beta}_{\alpha}P_y$ by resolving forces in the *x* and *y* directions and taking moments about the arch centre:

in *x* direction: $$N_\alpha.\cos(\alpha) - N_\beta.\cos(\beta) + S_\beta.\sin(\beta) = {}^{\beta}_{\alpha}P_x \quad (26)$$

in *y* direction: $$N_\alpha.\sin(\alpha) + N_\beta.\sin(\beta) + S_\beta.\cos(\beta) = {}^{\beta}_{\alpha}P_y \quad (27)$$

About the centre: $$N_\alpha.r_i - N_\beta.r_i = {}^{\beta}_{\alpha}P_y.\sin\rho - {}^{\beta}_{\alpha}P_x.\cos\rho \quad (28)$$

$$\Rightarrow \quad \begin{bmatrix} N_\alpha \\ N_\beta \\ S_\beta \end{bmatrix} = \begin{bmatrix} \cos(\alpha) & -\cos(\beta) & \sin(\beta) \\ \sin(\alpha) & \sin(\beta) & \cos(\beta) \\ r_i & -r_i & 0 \end{bmatrix}^{-1} \begin{bmatrix} {}^{\beta}_{\alpha}P_x \\ {}^{\beta}_{\alpha}P_y \\ {}^{\beta}_{\alpha}P_y.\sin\rho - {}^{\beta}_{\alpha}P_x.\cos\rho \end{bmatrix} \quad (29)$$

For a load acting at the fill surface, the quantities $\rho, {}^{\beta}_{\alpha}P_x,\ {}^{\beta}_{\alpha}P_y$ may be modelled by evaluating the dispersal model at the arch-fill interface for the applied load using moment equilibrium to determine ${}^{90}_{0}P_x,\ {}^{90}_{0}P_y$ and ρ may be estimated at their point of intersection ${}^{\beta}_{\alpha}\bar{x}, {}^{\beta}_{\alpha}\bar{y}$.

Where: $${}^{\beta}_{\alpha}\bar{x} = \frac{\int_\alpha^\beta \sigma_y.x\,.dx}{{}^{\beta}_{\alpha}P_y}, \quad {}^{\beta}_{\alpha}\bar{y} = \frac{\int_\alpha^\beta \sigma_x\,.y.dy}{{}^{\beta}_{\alpha}P_x}$$

And from Figure 4.3 and Figure 4.2:

$$\sigma_x = b_x + g_x$$
$$\sigma_y = b_y + g_y \quad (30)$$

$$x = r_e.sin(\theta)\,, \qquad y = r_e.cos(\theta), \qquad ds = r_e.d\theta$$

$$dx = ds.cos(\theta) = r_e.cos(\theta).d\theta = y.d\theta$$

$$dy = ds.sin(\theta) = r_e.sin(\theta).d\theta = x.d\theta$$

Thus for Eq. (29):

$$\Rightarrow \quad {}^{\beta}_{\alpha}P_x = \int_{\alpha}^{\beta} \sigma_x \,.\, dy = \int_{\alpha}^{\beta} \sigma_x \,.\, x.\, d\theta$$

$$\Rightarrow \quad {}^{\beta}_{\alpha}P_y = \int_{\alpha}^{\beta} \sigma_y \,.\, dx = \int_{\alpha}^{\beta} \sigma_y \,.\, y.\, d\theta$$

Similarly, ρ_α is defined as the angular location of the point where the line of action of ${}^{\rho}_{\alpha}\vec{P}$ intersects the tangent to the arch extrados at ρ which must also pass through the point $\left({}^{\rho}_{\alpha}\bar{x}, {}^{\rho}_{\alpha}\bar{y}\right)$ and will be inclined at an angle $tan^{-1}\left(\frac{{}^{\rho}_{\alpha}P_x}{{}^{\rho}_{\alpha}P_y}\right)$ to the vertical.

With reference to Figure 4.16, the angular location α of hinge 2 may be found as follows:

$$\frac{r_i}{cos(\rho_\alpha - \alpha)} = \frac{r_e}{cos(\rho - \rho_\alpha)}$$

$$\Rightarrow \quad \alpha = \rho_\alpha - cos^{-1}\left(\frac{r_i}{r_e}.cos(\rho - \rho_\alpha)\right) \tag{31}$$

In fact, the only output that is required from equations (29) for determining the stability of the system is N_α as will become clear later. The line of thrust in the arch will be tangential to the arch at α and ρ because at hinges 1 and 2, there is no external means of supporting a discontinuity in radial shear for the line of thrust to intersect the arch obliquely. Therefore there will be no radial shear force at α and ρ. This enables N_α to be obtained simply by modelling segment 2 as shown in Figure 4.16b, taking moments about hinge1:

$$\Rightarrow \quad N_\alpha = \frac{{}^{\rho}_{\alpha}P_y.\left({}^{\beta}_{\alpha}\bar{x} - {}^{\rho}_{\alpha}\bar{x}\right) + {}^{\rho}_{\alpha}P_x.\left({}^{\rho}_{\alpha}\bar{y} - {}^{\beta}_{\alpha}\bar{y}\right)}{\left(r_i - r_e.cos(\rho - \alpha)\right)} \tag{32}$$

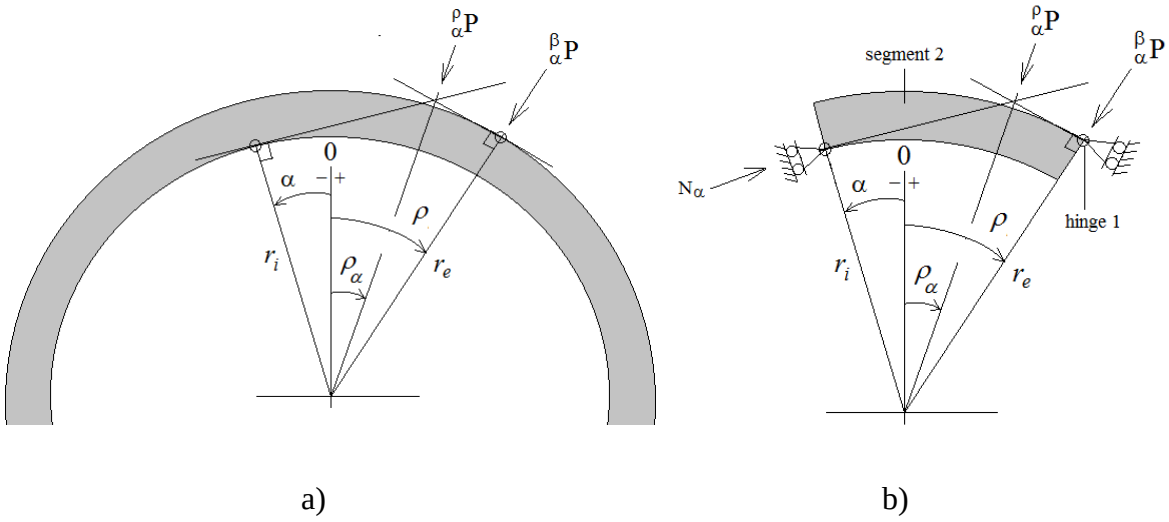

a) b)

Figure 4.16 – geometric relationship between destabilising forces and hinges 1 and 2

4.1.12 Bearing capacity failure vs. Arch-fill system failure

The fill in the region between the applied load at the fill surface and the arch extrados may fail in two ways; by loss of stability of the arch-fill system, or by bearing failure at the fill surface at a load lower than that required to destabilise the arch. This will depend on the proximity of the applied loads to the arch or the position of the load over the arch and the strength parameters of the fill.

If the load is it is positioned such that there is poor transmission from the applied load to the arch failure mechanism, then very large stresses would be need to be setup between the applied load and the fill in order to cause a failure mechanism of the arch-fill system. In order for failure of the arch-fill system to occur, the lateral pressures in the adjacent fill would need to be sufficient to confine the stress field transmitting the applied load to the arch. If the lateral restraint of the adjacent fill is not sufficient to confine this stress field, then the alternative path for the applied load to take would be through a bearing failure mechanism.

This was noticed from numerical model simulations when low strength parameters were applied to he fill material. At a particular loading position the failure mode switched to arch-fill system failure, i.e. a bifurcation point was observed. (Figure 4.17)

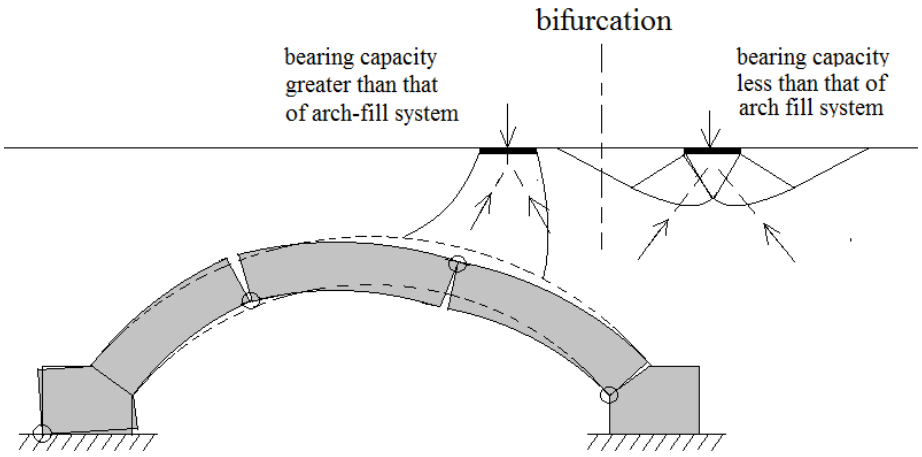

Figure 4.17 – Illustrating the bifurcation between two failure modes of the system: bearing failure of the fill and arch-fill system failure

The problem studied in the present research is the former case, where the applied load is positioned over the arch such that bearing failure does not occur before failure of the arch. This case may be checked for an assessment using existing bearing capacity theory when investigating the most onerous load cases for a bridge. Therefore the 'non-trivial' problem is studied in the present research.

4.1.13 Use of the Boussinesq equations as a Dispersal Model

The Boussinesq equations are a well known and widely used model for evaluating stresses within a medium subjected to some external force applied at the surface of the medium. However the applicability of this model is limited by assumptions under which it holds. These are:

i. The medium occupies an infinite half space, i.e the surface in a straight line that extends infinitely and the medium also extends infinitely in area on one side of the surface.

ii. The stresses are consequential to an applied load that acts on the free surface and normal to it. This means that there will be not traction component at the point of application of the load at the surface.

iii. The medium is linear, i.e there is a linear relationship between the load applied at the surface and the consequential stresses evaluated within the medium.

iv. The medium is homogeneous and isotropic, i.e. there is no spatial variation of the constitutive properties of the medium throughout.

The fill in an arch bridge will generally be none of these. The medium, rather than being an infinite half space, contains a masonry arch which supports a void beneath it, the arch also being close to the surface. The fill may consist of various strata which may or may not have been compacted uniformly and may have suffered various forms of degradation during their life.

However under specific conditions, the loading and confinement of the fill may constrain part of the arch such that it's behaviour may be reasonably modelled as linear elastic. The fill will depart from linear elastic behaviour when subjected to sufficient deviator stress to cause large shear strains to occur. Under confined compressive stress, resembling the conditions within an Oedometer test, the fill may be expected to conform reasonably well to a linear elastic model until stresses exceed the linear range in compression.

During a static load test in which the load is gradually increased, prior to failure of the arch-fill system, the pressure acting on segments 1 and 2 over hinge 1 will gradually increase. As the load increases, the force N_α will also increase. This will progressively mobilise the restraining pressure from the fill adjacent to segment 3. As long as the capacity of the fill adjacent to segment 3 has not been full mobilised and remains stable, the arch will be constrained to small displacements. Once a failure mechanism is formed in the fill adjacent to segment 3 and a stability of that body of the fill is lost, the arch will also loose stability begin to displace excessively if not indefinitely.

Before destabilisation, the region of fill between the applied load and hinge 1 may only undergo compression and volumetric strain. Masonry arch bridges currently in use and subject to assessment will most likely have been in service for at least 100 year. Therefore it may be

expected that the stress strain behaviour within this region of the fill may conform reasonably to linear elastic behaviour up to the maximum service load. Some departure from the linear compression curve may occur at very high loads leading up to system failure.

4.1.14 The arching effect over hinge 1

The effect of the presence of the arch on the applicability of the Boussinesq equations is not clear, however as hinge 1 begins to articulate, the soil arching effect may be expected over the yielding hinge. This effect was investigated by Terzaghi () in his well known trap-door experiment. According to the literature on the soil arching effect, the loss of support beneath the body of soil due to displacement of hinge 1 would be supported by shearing stress in adjacent fill. This shearing stress would be transmitted down to the arch extrados, either side of the displaced hinge, resulting in a redistribution of pressure. The resultant over the segments however, should remain unchanged (Figure 4.18).

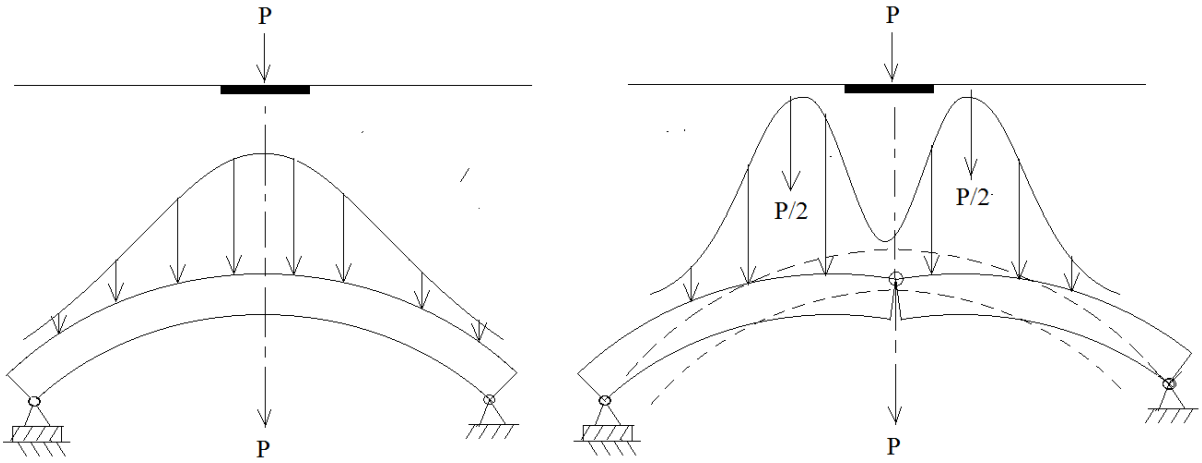

Figure 4.18 – Illustrating the expect3ed arching effect due to articulation of an extrados hinge below an applied load.

Thus for a specific load shape such as a strip load, the relevant Boussinesq Equations (33) may evaluated at the extrados surface and together with dead loads from the fill, may be substituted in to equations (30 - (32), to obtain N_α. Based on the above discussion, the K_0 coefficient of lateral earth pressure is considered appropriate for this region of the fill for computing the horizontal

component of the dead loads from the fill and is used in the quantitative analysis of the physical model tests for demonstration of the analysis procedure described in the present chapter.

Thus for load acting at the fill surface, the quantities required for obtaining α and N_α may be computed by evaluating the Boussinesq equations at the arch-fill interface for the applied load using moment equilibrium to determine the lines of action of the resultants of pressures. In the physical model tests in the research, loads have been applied to the fill surface by means of steel beams, spanning the width of the arch-fill system, to simulate loads applied to railway sleepers.

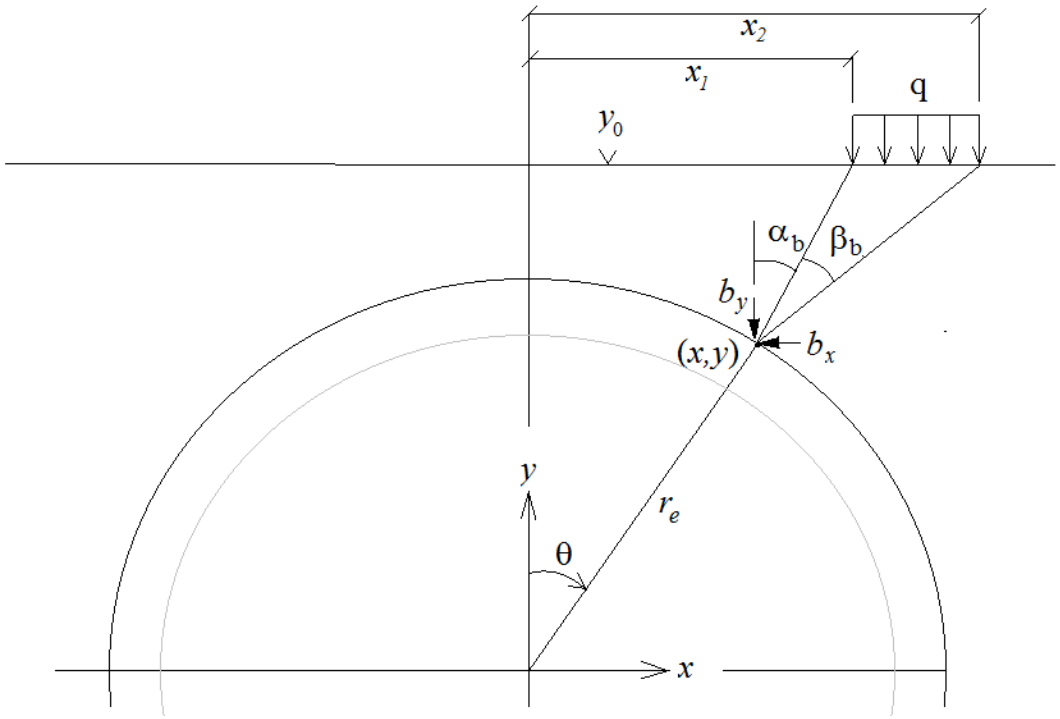

Figure 4.19

$$b_y = \frac{q}{\pi}[\alpha_b + sin(\alpha_b).cos(\alpha_b + 2\beta_b)]$$

$$b_x = \frac{q}{\pi}[\alpha_b - sin(\alpha_b).cos(\alpha_b + 2\beta_b)] \qquad (33)$$

$$g_y = \gamma.(y_0 - y), \qquad g_x = K_0.\gamma.(y_0 - y)$$

Where: $$\beta_b = tan^{-1}\left(\frac{x_1 - x}{y_0 - y}\right), \qquad \alpha_b = tan^{-1}\left(\frac{x_2 - x}{y_0 - y}\right) - \beta_b \tag{34}$$

4.1.15 Analysis of segment 3

This segment is where the restraint from the arch fill comes in to play, which is the primary restraint of the arch-fill system; destabilisation of segment 3 will result in destabilisation of the arch-fill system. Thus the value of N_α required to destabilise segment 3 provides the final link between applied loads and the ultimate capacity of the arch-fill system. The observations so far, regarding the part of the mechanism dominated by destabilising pressures, provide a good means of estimating the location of α and the thrust N_α acting at the hinge. Since this hinge is a turning point in the thrust line with respect to the arch axis, there will be no shear force at this hinge. This provides a statically determinate problem for analysis of segment 3 illustrated in Figure 4.20

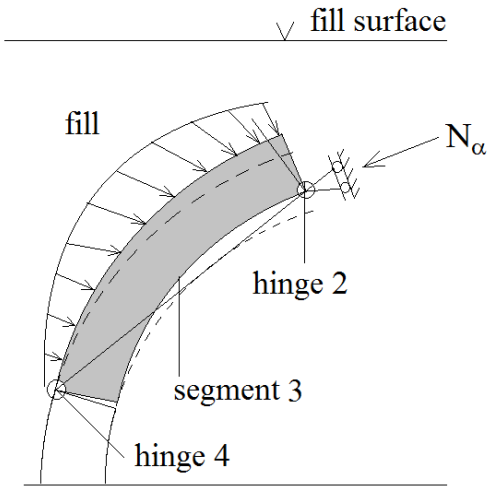

Figure 4.20 – Modelling limiting rotational equilibrium of segment 3 about hinge 4

As N_α approaches the ultimate value, the stabilising pressures on segment 3 increase in magnitude due to progressive mobilisation of the soil strength of the fill. In general, the stabilising pressure will increase with depth below the fill surface. Hinge 4 will occur at the location that minimises N_α. This location will depend on the distribution of stabilising pressures acting on the arch due to fill. This distribution will in general depend on the progressive

mobilisation of the soil strength of the fill. Therefore the initial hinge position will not necessarily be the same as the ultimate hinge position. This migration of hinge 4 has been observed in the numerical model as discussed earlier with reference to (Figure 4.14).

4.1.16 A generalisation of Rankine passive earth pressure theory to model fully mobilised restraining pressures from the fill on segment 3

Consider the rotation of segment 3 about hinge 4 at angular location β_2 where Coulomb frictional slip occurs at the arch-fill interface. As discussed in section #, it is reasonable to assume slip throughout segment 3 for the ultimate limit state. With reference to Figure 4.21, a family of linear slip surfaces may be defined that satisfy boundary conditions at the extrados interface as well as equilibrium with adjacent fill as described in below with reference to Figure 4.21c

$$d\theta \to 0 \;\Rightarrow ds = r_e.d\theta \to 0 \Rightarrow dw \to \gamma\left({R_s}^2 - {r_e}^2\right).\frac{d\theta}{2}.cos(\xi)$$

$$\Rightarrow \frac{dw}{ds} = \frac{\gamma}{2r_e}.\left({R_s}^2 - {r_e}^2\right).cos(\xi)$$

Where θ is the angle of the normal to the extrados surface from the vertical, $\upsilon(\theta)$ is the angle of V_S from the vertical and $\xi(\theta) = \upsilon - \theta$.

In the case of slip at the interface, the principal stress σ_1, will act at angle δ to the normal of the extrados and from Mohr's Circle, the direction of shearing will occur at an angle $45 - \frac{\phi'}{2}$ from the direction of σ_1. A more detailed explanation of the aforementioned observations and the bases for assuming a state of slip on segment 3 is given in section #.

Resolving forces parallel to V_S where $\upsilon(\theta)$ is the angle of V_S from the vertical, θ is the angle of the normal to the extrados surface from the vertical and N_e is the force normal to the extrados.

$$N_e.cos(\xi) - N_e.tan(\delta).sin(\xi) = (N_2 - N_1).tan(\phi') + dw.cos(\upsilon)$$

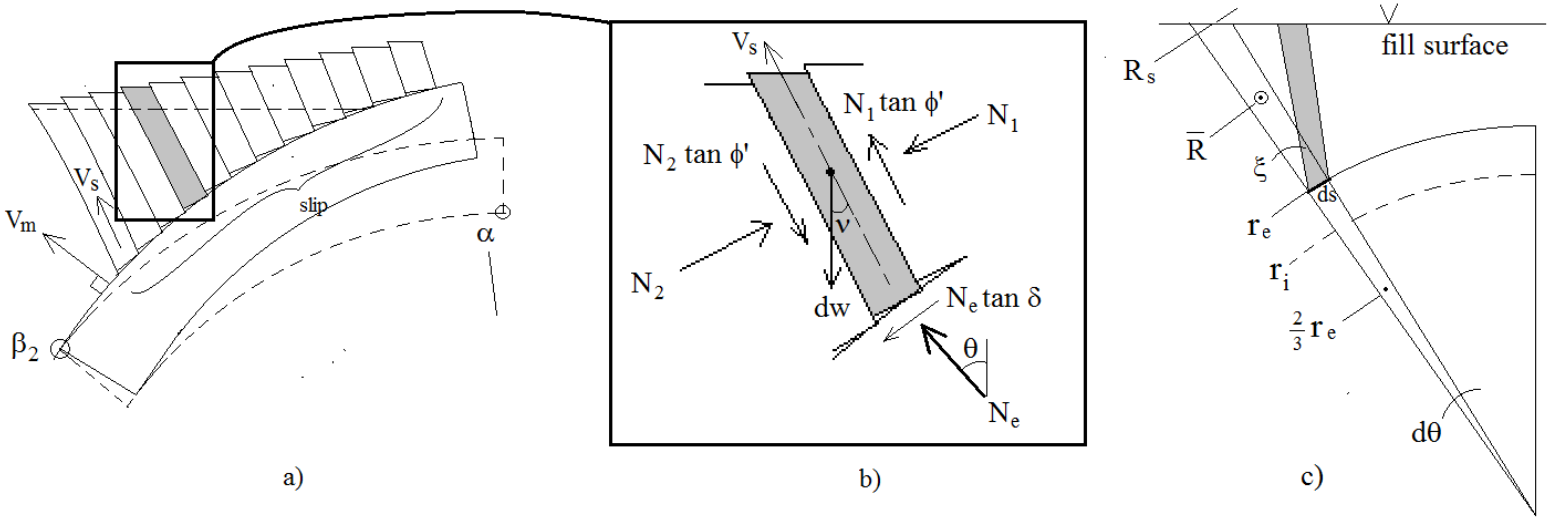

Figure 4.21 – Illustrating the formulation of a family of linear lamina used to derive a generalisation of Rankine lateral earth pressure in the ultimate passive case for segment 3

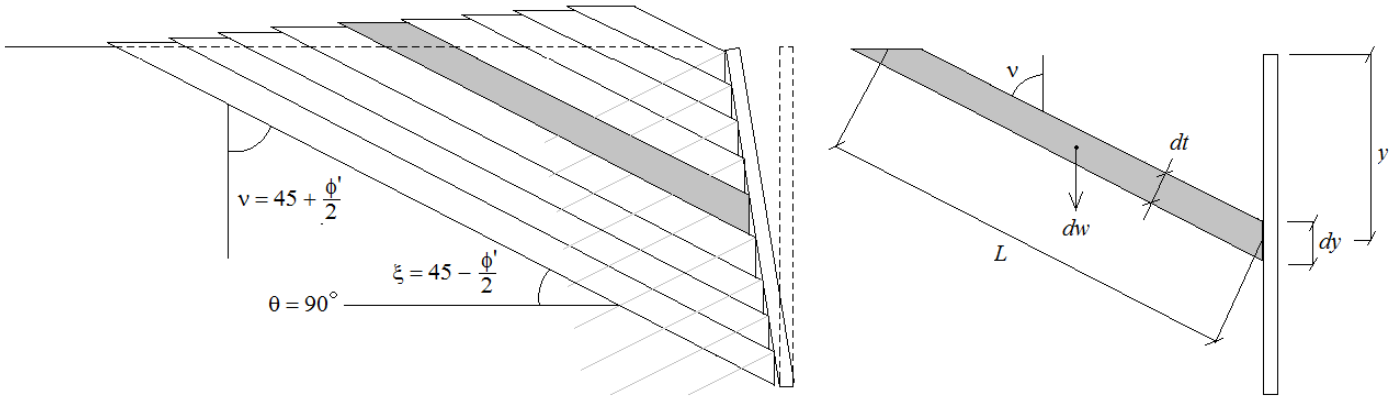

Figure 4.22 – Application of proposed approach to derive The Rankine Coefficient of passive earth pressure

Equilibrium in the direction perpendicular to V_S:

$$N_e.sin(\xi) + N_e.tan(\delta).cos(\xi) = (N_2 - N_1) - dw.sin(\upsilon)$$

$$\frac{N_e}{ds} = \sigma_e$$

$$\Rightarrow \quad \sigma_e = \frac{dw}{ds}.\left[\frac{cos(\upsilon) + sin(\upsilon).tan(\phi')}{\big(cos(\xi) - tan(\delta).sin(\xi)\big) - \big(sin(\xi) + tan(\delta).cos(\xi)\big).tan(\phi')}\right] \qquad (35)$$

For a smooth interface where $\delta = 0$, this reduces to:

$$\Rightarrow \quad \sigma_e = \frac{dw}{ds}.\left[\frac{cos(\upsilon) + sin(\upsilon).tan(\phi')}{cos(\xi) - sin(\xi).tan(\phi')}\right] \qquad (36)$$

For a smooth vertical wall with level fill (Figure 4.22) where:

$$\theta = 90°,\ \xi = 45 - \frac{\phi'}{2} \text{ and } \upsilon = 45 + \frac{\phi'}{2}:$$

$$ds = dy \to 0 \ \Rightarrow dw \to \gamma.L.dt = \gamma.y.tan(\upsilon).dy$$

$$\Rightarrow \quad \frac{dw}{ds} = \frac{dw}{dy} = \gamma.y.tan(\upsilon)$$

Thus Eq.(36) reduces to the Rankine passive pressures $\sigma_h = \gamma.y.K_p$ with horizontal fill:

$$\Rightarrow \quad \sigma_e = \gamma.y.tan(\upsilon).\left[\frac{cos(\upsilon) + sin(\upsilon).tan(\phi')}{cos(\xi) - sin(\xi).tan(\phi')}\right]$$

$$\Rightarrow \quad \sigma_h = \gamma.y.\left[\frac{1 + sin(\phi')}{1 - sin(\phi')}\right] = \gamma.y.K_p$$

4.1.17 The resultant force P_p due to passive pressure on segment 3

With reference to Figure 4.21, in order to determine the location of the resultant force on the extrados of segment 3, N_e and $N_e.tan(\delta)$ may be resolved into the horizontal and vertical directions, using σ_e from Eq. (35)

$$\Rightarrow \qquad \sigma_{px} = \sigma_e.sin(\theta) + \sigma_e.tan(\delta).cos(\theta)$$

$$\sigma_{py} = \sigma_e.cos(\theta) + \sigma_e.tan(\delta).sin(\theta)$$

$$P_{px} = \int_{\beta_2}^{\alpha} \sigma_e.\big(sin(\theta) + tan(\delta).cos(\theta)\big).d\theta$$

$$\Rightarrow$$

$$P_{py} = \int_{\beta_2}^{\alpha} \sigma_e.\big(cos(\theta) + tan(\delta).sin(\theta)\big).d\theta$$

The vertical location of P_{px} may be determined by taking moments about hinge 4 located at β_2:

$$\Rightarrow \qquad y_{px} = \frac{\int_{\beta_2}^{\alpha} \sigma_{px}.r_e.\big(cos(\theta) - cos(\beta_2)\big)d\theta}{P_{px}}$$

Similarly, the horizontal location of P_{py} may be determined:

$$\Rightarrow \qquad x_{py} = \frac{\int_{\beta_2}^{\alpha} \sigma_{py}.r_e.\big(sin(\theta) - sin(\beta_2)\big)d\theta}{P_{py}}$$

The line of action of $\vec{P}_p = \begin{bmatrix} P_{px} \\ P_{py} \end{bmatrix}$ would therefore pass through the point (x_{py}, y_{px}), as shown in Figure 4.23 and be inclined at an angle $tan^{-1}\left(\frac{P_{px}}{P_{py}}\right)$ to the vertical.

As observed in Figure 4.14, the location of hinge 4 (β_2), occupies a range of values and increases as loading progresses. As the shear strength of the fill approaches full mobilisation the value of β_2 converges to a critical state value. The model for stabilising pressures on segment 3 is based on full mobilisation of the internal friction of a cohesionless soil fill. Thus P_p obtained from this model will correspond to the final value of β_2. The value β_2 will satisfy the limiting equilibrium state at the verge of rotation of segment 3 about hinge 4. Thus a factor of safety against overturning may be obtained by finding β_2 that minimises N_α.

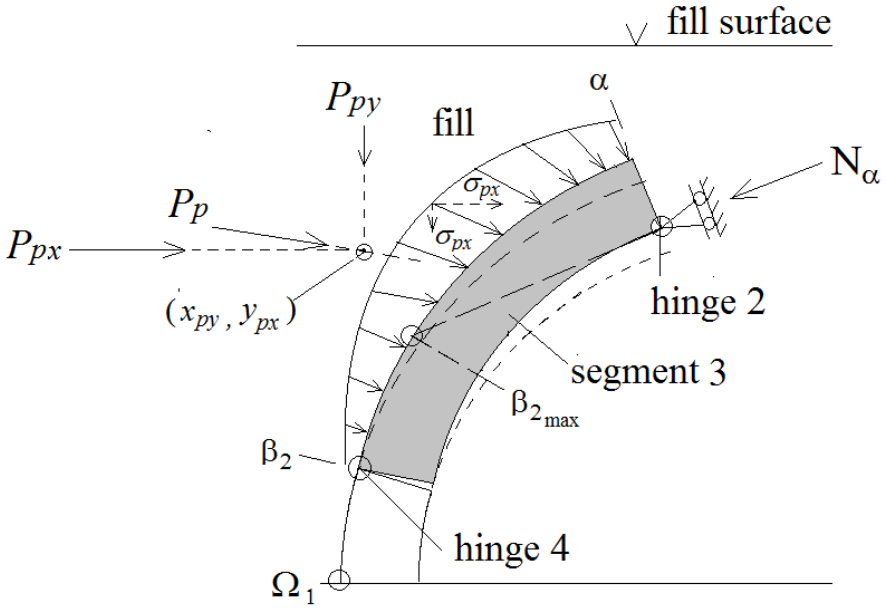

Figure 4.23 – Illustrating the location of resultants due to pressures acting on segment 3

Taking moments about hinge 4:

$$\Rightarrow \qquad N_\alpha = \frac{{}^{\alpha}_{\beta_2}P_{px}.y_{px} + {}^{\alpha}_{\beta_2}P_{py}.x_{py}}{(r_i - r_e.cos(\alpha - \beta_2))} \qquad (37)$$

Thus the ultimate position of β_2 will be that corresponding to the minimum N_α with respect to β_2 in Eq. (37) over the range of possible values of β_2, i.e. from the fixed abutment to the point on the extrados at which $\vec{N}_\alpha$ intersects the extrados, where: $\Omega_2 \leq \beta_2 \leq \beta_{2\,max}$. The value of applied load corresponding to this value of N_α will then be the estimate of the load baring capacity.

4.1.18 Implementation of the proposed method of analysis to the Physical model tests with Boussinesq dispersal and the generalised Rankine theory for fill resistance

The method of analysis described in the preceding sections has been implemented by means of a Matlab script for the load tests described in section # carried out on the physical model during the resent research.

The geometry of the experimental model, test chamber and loading arrangements were used in the script. Material properties from of the constituents of the physical models that were available with reasonable accuracy were used in the script. For material parameters relevant to the theoretical model, which were estimated with less confidence, a range of values within which the true values may reasonably be expected to lie was given to the script for evaluation across that range. Specifically, these were the angle of internal friction of the limestone fill and the angle of friction at the interface between the masonry and the fill. The Script for this computation is given in Appendix A.

The range of values for the angle of effective internal friction ϕ' within the fill for which the theoretical model was evaluated, were 40° to 55°. The angle of friction at the masonry-fill interface δ, was evaluated over the range $\frac{\phi\prime}{3}$ to $\frac{2\phi\prime}{3}$. These are plotted in for the three different loading arrangements tested with the physical model. Also plotted in are the ultimate hinge positions for each of the tests.

The theoretical model is also evaluated over a wider range of ϕ' and δ in order to observe the sensitivity of the ultimate load bearing capacity of the system evaluated by the theoretical model to these two parameters. These are plotted in for the three different loading arrangements tested with the physical model.

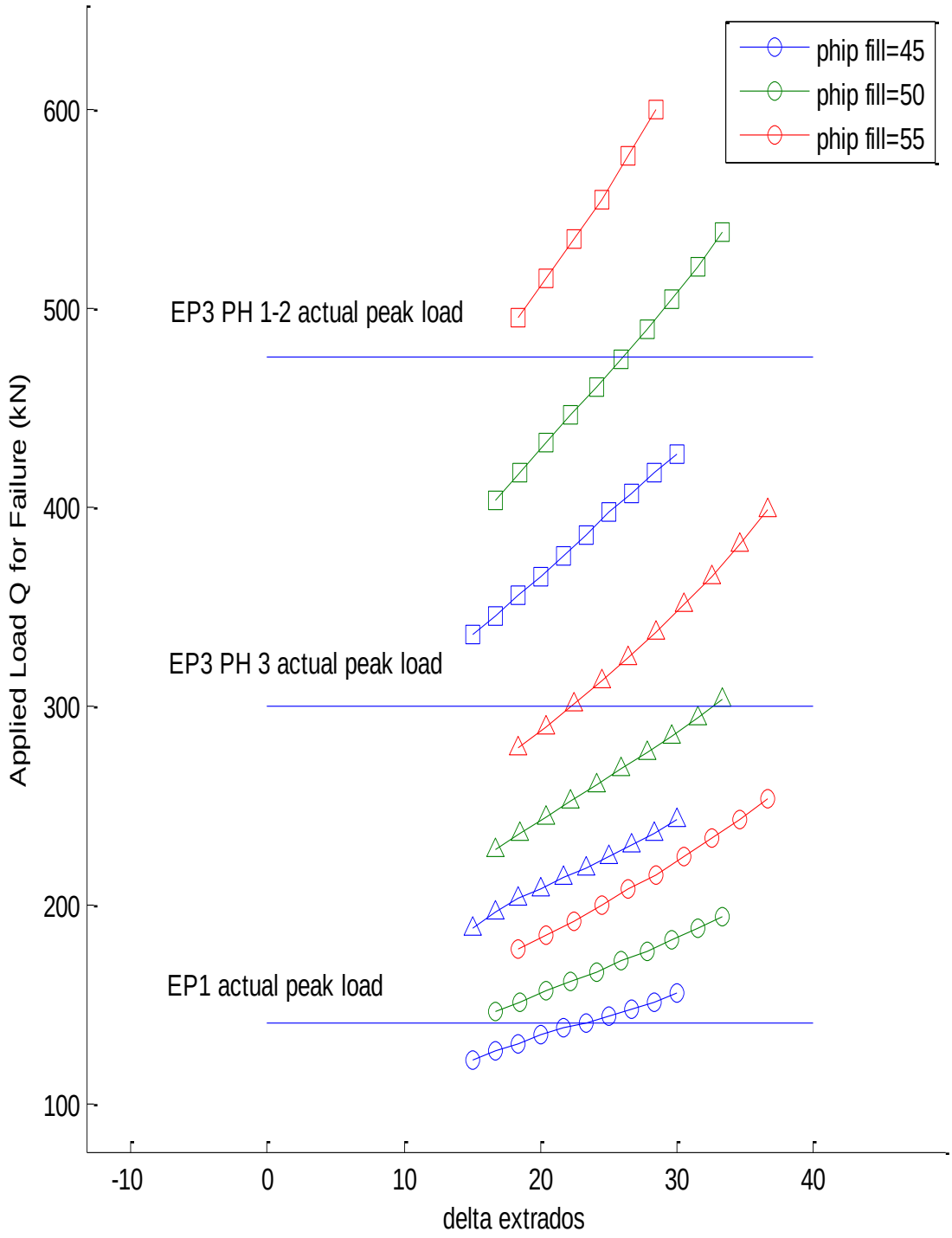

Figure 4.24 – Ultimate capacity estimates from the theoretical model for a range of effective internal soil friction angles ϕ' and soil-structure interface friction angles δ, superimposed with peak loads obtained from the physical model tests.

Chapter 5 Discussion & Conclusions

The aim of the present research was to provide a practical theoretical model based on elementary statics, for assessment for masonry arch bridges, that benefits from the large scale experimental programme at Salford University, together with insight gained from the Distinct Element numerical modelling work.

The need for large scale laboratory controlled load tests of physical models that may be reliably confined to a specific domain of behaviour with known parameters and modelling constraints, was highlighted in chapter 2 with reference to literature.

Load tests on various distributions of surcharge were carried and the mechanisms of failure observed. The numerical modelled was shown to agree with expected theoretical behaviour and shown good agreement with experimental results.

A theoretical model was developed which benefitted from insight from the experimental and numerical work to provide a means of predicting the failure load of the arch-fill system for the lading arrangements carried out in the physical and numerical tests.

The model provided predicted failure loads for a range of material variation within a reasonable expected range and showed promising resemblance to the physical modelling results.

References

Albuerne A, Huerta S, (2010), *Coulomb's theory of arches in Spain ca. 1800: the manuscript of Joaquín Monasterio, Proc*. 6th International Conference on Arch Bridges, pp. 354-362

Arede A, Costa A, Costa C, (2010), *Numerical simulation of stone masonry arch bridges behaviour under road traffic moving loads*, Proc. 6th International Conference on Arch Bridges, Fizhou University, Fizhou, China, Arch Bridges

Augusthus-Nelson, L. Swift, G. Smith, C. Melbourne, C. Gilbert, M. (2014). *Large scale physical modelling of soil-filled masonry arch bridges under cyclic loading*, Under review for International Journal of Physical Modelling in Geotechnics.

Augusthus-Nelson L, Swift G, Melbourne C, Gilbert M, Smith CC. (2017) *Large Scale Physical Modelling of Soil-filled Masonry Arch Bridges* – Not Published

Baker JF, Horne MR, Heyman J, (1956), *The steel Skeleton*, Vol. 2: Plastic Behaviour and Design, Cambridge

Block P, DeJong M, Ochsendorf J, (2006), *As Hangs the Flexible Line: Equilibrium of Masonry Arches*, Nexus Network Journal, Vol. 8, No. 2, pp. 13-24, Kim Williams Books, Firenze

Boothby TE, (2001), *Analysis of masonry arches and vaults*, Prog. Struct. Engng Mater, Vol. 3, pp. 246-256

Brencich A, Colla A, (2002), *The influence of construction technology on the mechanics of masonry railway bridges*, Department of structural and Geotechnical Engineering, University of Genoa, Italy

Brencich A, De Francesco U, Gambarotta L, (2001), *Elastic no tensile resistant - plastic analysis of masonry arch bridges as an extension of Castigliano's method*, Proc. 9th Canadian Masonry Symposium.

Breymann GA, (1849), *Bau-Constructions-Lehre*. Vol. 1: Constructionen in Stein. Stuttgart.

Bridle RJ, Hughes TG, (1990), *An energy method for arch bridge analysis*, Proc. Instn Civ. Engrs, Part 2, Vol. 89, pp. 375-385

Burroughs P, Hughes TG, Hee S, Davies M, (2002), *Passive pressure development in masonry arch bridges*, Proc. ICE, Structures & Buildings, vol. 152, no. 4, pp. 331-339

Calloway PA, (2007), Soil-structure interaction in masonry arch bridges, PhD thesis, University of Sheffield.

Calloway P, Gilbert M, Smith CC, (2012), Influence of Backfill on the Capacity of Masonry Arch Bridges. Proc. ICE, Bridge Engineering, 165(3). 147 - 157

Carpenteri A, Lucidogna G, Pugno N, (2004), *A Fractal Approach for Damage Detection in Concrete and Masonry Structures by the Acoustic Emission Technique*, Accoustique & Technique, No. 38, pp. 31-37

Carpenteri A, Lacidogna G, (2006a), *Damage evaluation of three masonry towers by acoustic emission*, Engineering Structures, Vol. 29, pp. 1569-1579, Elsevier

Carpenteri A, Lacidogna G, (2006b), *Damage monitoring of an historical masonry building by the acoustic emission technique*, Materials and Structures, Vol. 39, pp.161–167, RILEM

Carpenteri A, Lacidogna G, Pugno N, (2007), *Structural damage diagnosis and life-time assessment by acoustic emission monitoring* , Engineering Fracture Mechanics, Vol. 74, pp. 273–289, Elsevier

Chandrupatla TR, Belegundu AD, (2002), *Introduction to finite elements in engineering*, (Third Edition), New Jersey, USA, Prentice Hall.

Chettoe CS, Henderson W, (1957), *Masonry arch bridges: A study*, Proc. Inst. Civ. Eng, Vol. 7, pp. 723-774.

Chevalier, B. (2011). *Experimental and discrete element modeling studies of the trapdoor problem: influence of the macro-mechanical frictional parameters*, Acta Geotechnica, DOI 10.1007/s11440-011-0152-5

Choo BS, Coutie MG, Gong NG, (1991), *Finite element analysis of masonry arch bridges using tapered elements*. Proc. Instn Civ. Engrs, Part 2, Vol. 91, pp. 755-770.

Conti S, Gosling JP, Oakley JE, O'Hagan A, (2009), *Gaussian process emulation of dynamic computer codes*, Biometrika, Vol. 96, No. 3, pp. 663–676, Biometrika Trust

Coulomb, C. A., (1773). *On an application of the rules of maximum and minimum to some statical problems, relevant to architechture*. Memoires de Mathematique & de Physique, Volume 7, pp. 343-82.

Crisfield MA, (1984), *A finite element computer program for the analysis of masonry arches*, Department of Transport, TRRL Laboratory report 1115, Transport Research Laboratory, Crowthorne.

Crisfield MA, (1985a), *Computer methods for the analysis of masonry arches*, Proc. 2nd Int. Conference on Civil and Structural Engineering computing, Edinburgh, Civil-Comp Press.

Crisfield MA, (1985b), *Finite element and mechanism methods for the analysis of masonry and brickwork arches*, Department of Transport, TRRL Research Report 19, Transport Research Laboratory, Crowthorne.

Crisfield MA, Packham AJ, (1987), *A mechanism program for computing the strength of masonry arch bridges*, Department of Transport, TRRL Research Report 124, Transport Research Laboratory, Crowthorne.

Crisfield MA, Wills J, (1986), *Nonlinear analysis of concrete and masonry structures*, In: Bergan et al (Eds). Finite element methods for nonlinear problems, Berlin, pp. 639-652, Springer Verlag.

Cundall PA, Hart RD, (1992), *Numerical Modelling of Discontinua*, Engineering Computations vol.9, pp. 101-113, Pineridge Press

Das PC, (1995), *The Assessment of masonry arch bridges*, Proc. 1st Int. Conference on Arch Bridges, pp. 21-27.

Davey N, (1953), *Tests on road bridges*, National Building Studies, research paper No. 16, London, HMSO.

Department of Transport, (1984a), *The assessment of highway bridges and structures*, Departmental Standard BD 21/84

Department of Transport, (1984b), *The assessment of highway bridges and structures*, Advice note BA 16/84, London

Department of Transport, (1993a), *The assessment of highway bridges and structures*, Departmental Standard BD 21/93

Department of Transport, (1993b), *The assessment of highway bridges and structures*, Advice note BA 16/93, London

De Stefano, (2007), *Structural Identification and Health Monitoring on the Historical Architectural Heritage*, Key Engineering Materials, Vol. 347, pp. 37–54

Diamanti N, Giannapoulos A, Forde MC (2008), *Numerical modelling and experimental verification of GPR to investigate ring separation in brick masonry arch bridges*, NDT & E International, Vol. 45, No. 5, pp. 354-363, Elsevier.

Drucker DC, (1953), *Coulomb friction, plasticity and limit loads*, Transactions American Society Mechanical Engineers, Vol. 76, pp. 71-74

Emamian V, Kaveh M, Tewfik AH, Shi Z, Jacobs LJ, Jarzynski J (2002), *Robust Clustering of Acoustic Emission Signals Using Neural Networks and Signal Subspace Projections*, EURASIP Journal on Applied Signal Processing, Vol. 3, pp. 276–286, Hindawi Publishing Corporation

Fang Y, Chen T, Holtz R, Lee W, (2004), *Reduction of boundary friction in model tests*, Geotechnical Testing Journal, vol. 27, no. 1, pp. 3-12.

Flugge W, (1962), *Handbook of engineering mechanics*, New York, USA, McGraw-Hill

Foce F, Aita D, (2003), *The masonry arch between limit and elastic analysis: A critical re-examination of Durand-Claye's method*, Proc. First International Congress on Construction History, Madrid, Spain

Fyfe AG, Pande GN (Supervisor), (2000), *Numerical modelling of workmanship in masonry structures*, PhD Thesis, Department of Civil Engineering, University of Swansea

Gilbert M, (2007), *Limit analysis applied to masonry arch bridges: state-of-the-art and resent developments*, Proc. 5th International Conference on Arch Bridges, pp. 14-28

Gilbert M, Wang J, Calloway PA, Melbourne C, (2007), *Small and large scale experimental studies of soil-arch interaction in masonry bridges*, Proc. 5th International Conference on Arch Bridges, pp. 381-388.

Gilbert M, Casapulla C, Ahed HM, (2006), *Limit analysis of masonry block structures with non-associative frictional joints using linear programming*, Computers and Structures, Vol. 84, pp. 873–887

Gilbert M, Melbourne C, (1994), *Rigid-Block analysis of masonry structures*, The Structural Engineer, Vol. 72, No. 21, pp. 356-361.

Giordano A, Luca AD, Mele E, (2002), *Modelling of historical masonry structures: comparison of different approaches through a case study*, Engineering Structures Vol. 24, pp. 1057–1069, Elsevier

Harvey WJ, (1988), *The application of the mechanism method to masonry arch bridges*, Struct. Engr. Vol. 66, No. 5, p. 77-84.

Harvey WJ, (1991), *Stability, strength, elasticity and thrustlines in masonry structures*, The Structural Engineer, Vol. 69, No. 9, pp. 181-184.

Harvey WJ, (2001), *The complex relationship between analysis, testing and assessment of arch bridges*, Proc. Structural Faults and Repair.

Hashash YMA, (1992), *Analysis of deep excavations in clay*. PhD, Department of Civil and Environmental Engineering, Massatchusetts Institute of Technology, Cambridge.

Hashash YMA, Whittle AJ, (2002), *Mechanisms of load transfer and arching for braced excavations in clay*. Journal of Geotechnical and Geoenvironmental Engineering, 128(3):187–97.

Hashash YMA, Marulanda C, Ghaboussi J, Jung S, (2003), *Systematic update of a deep excavation model using field performance data*, Computers and Geotechnics, vol. 30, pp. 477–488.

Hendry AW, Davies SR, Royles R, (1985), *Test on stone masonry arch at Bridgemill-Girvan*, Department of Transport. TRRL Contractor Report 7, Transport Research Laboratory, Crowthorne.

Heyman J, (1966), *The Stone Skeleton, Int. J. Solids Structures*, Vol. 2, pp. 249-279. Pergamon

Heyman J, (1980), *Estimation of the strength of masonry arches*, Proc. Instn Civ. Engrs, Part 2, 1980, vol. 69, pp. 921-937

Heyman, J., (1997). *Coulomb's Memoir on Statics*. London: Imperial College Press.

Heyman J, (1998), *Structural Analysis: A Historical Approach*. Cambridge: Cambridge University Press.

Hight DW, Higgins KG, (1994), *An approach to the prediction of ground movements in engineering practice: background and application*, Int. Symposium on Pre-Failure Deformation Characteristics of Geomaterials, Sapporo, Japan, p. 187–223.

Horne MR, (1979), *Plastic theory of structures*, 2nd edition, Oxford: Pergamon Press.

Hulet, K.M, Smith, C.C., Gilbert, M. (2006), *The influence of flooding on the load carrying capacity of masonry arch bridges*, Proc. Inst. Civil Engrs, Bridge Engineering, Vol. 159, pp. 97-103

Ince NF, Kao CS, Kaveh M, Tewfik A, Labuz JF (2010), *A Machine Learning Approach for Locating Acoustic Emission*, EURASIP Journal on Advances in Signal Processing, doi:10.1155/2010/895486, Hindawi Publishing Corporation.

Kooharian A, (1953), *Limit analysis of voussoir (segmental) and concrete arches*. Proc. Am. Concr. Inst. 89, 317.

Kurrer, K.-E., (2009). *From Masonry Arch to Elastic Arch. In: The History of the Theory of Structures*. s.l.:John Wiley & Sons, pp. 205-206.

Livesley RK, (1978), *Limit analysis of structures formed from rigid blocks*, International Journal for Numerical Methods in Engineering, Vol. 12, pp.1853-1871

Lourenco, P.B, , (1994) *Analysis of Masonry Structures with Interface Elements – Theory and Applications*, *TNO Building and Construction Research: Computational Mechanics*, Delft University of Technology

Lourenco PB, (2004), *Current experimental and numerical issues in masonry research*, Department of Civil Engineering, University of Minho

Lourenco PB, Oliveira DV, (2004), *Implementation and validation of a constitutive model for the cyclic behaviour of interface elements*, Computers and Structures Vo. 82, pp. 1451–1461, Elsevier

Mana AI, Clough GW, (1981), *Prediction of movements for braced cuts in clay*, Journal of Geotechnical Division, vol. 107, no. GT6, pp. 759–77.

McKibbins LD, Melbourne C, Sawar N, Gaillard CS (2006), *Masonry arch bridges: condition appraisal and remedial treatment*, CIRIA

Melbourne C, Gilbert M, (1995), *The behaviour of multi-ring brickwork arch bridges*, The Structural Engineer, vol. 73 no. 3, p. 39–47.

Melbourne C, Gilbert M, Wagstaff M, *The Behaviour of Multi-span Masonry Arch Bridges* (1995), Proc. Int. J. Arch Bridges, pp 489-497

Melbourne C, Tomor AK, (2006), *Application of Acoustic Emission for Masonry Arch Bridges*, Strain, Vol. 42, pp. 165–172, Blackwell

Melbourne C, Tomor A, Wang J, (2007), *A new masonry arch bridge assessment strategy (SMART)*, Proc. Institution of Civil Engineers: Bridges Engineering, Vol. 160, No. BE2, pp. 81-87, ICE

Melbourne C, Wang J, (2007), *Finite element analyses of soil-structure interaction in masonry arch bridges*, Proc. 5th International Conference on Arch Bridges, pp. 365-372

Munjiza, A., Owen, D.R.J. and Bicanic, N., 1995. A combined finite-discrete element method in transient dynamics of fracturing solids. *Engineering computations*, *12*(2), pp.145-174.

Nadukuru, S.S. Michalowski, R.L. 2012. *Arching in Distribution of Active Load on Retaining Walls*, Journal of Geotechnical and Geoenvironmental Engineering 138, 575-584. ASCE

Ochsendorf, J. A., (2002). *Collapse of Masonry Structures*. PhD Thesis, University of Cambridge.

Oden JT, (1972), *Finite elements of nonlinear continua*, New York, McGraw-Hill

Orban, Z., (2007). UIC *Project on assessment, inspection and maintenance of arch railway bridges*. Proc. 5th International Conference on Arch Bridges, pp. 3-12.

Orban Z, Gutermann M, (2009), *Assessment of masonry arch railway bridges using non-destructive in-situ testing methods*, Engineering Structures, Vol. 31, No. 10, pp. 2287–2298, Elsevier

Owen, D.R.J., Peric, D., Petrinic, N., Brookes, C.L. and James, P.J., 1998. Finite/discrete element models for assessment and repair of masonry structures. In A. Sinopoli ed.,, *Arch Bridges–History, analysis, assessment, maintenance and repair. Proc. Second Int. Arch Bridge Conf., AA Balkema* (pp. 173-180).

Page J, (1995), *Load tests to collapse on masonry arch bridges*, Proc. 1st Int. Conference on arch bridges, pp. 289-298.

Pilch M, Trucano T, Peercy D, Hodges A, Young E, Moya J, (2001), *Guidelines for Sandia ASCI Verification and Validation Plans – Content and Format: Version 2.0*, Sandia National Laboratory report SAND2000-3101.

Pippard AJS, Tranter E, Chitty L, (1936), *The mechanics of the voussoir arch*, J. Inst, Civ. Eng, Vol. 4, No. 281.

Pippard AJS, Ashby RJ, (1938), *An experimental study of the voussoir arch*, J. Instn. Civ. Engrs, Vol. 10, pp. 383-404.

Pippard AJS, Baker JF, (1943), *The Analysis of Engineering Structures*, (2nd edition), Edward Arnold.

Pippard AJS, (1948), *The approximate estimation of safe loads on masonry bridges*, Civil engineer in warInst Civ Eng, Vol. 1, pp. 365–372

Prager W, (1959), *An Introduction to Plasticity*, Addison-Wesley.

Rots JG, (1997), Structural Masonry: An Experimental/Numerical Basis for Practical Design Rules, NTO Building and construction research, Centre for Civil Engineering Research (CUR), A.A. Balkema, Rotterdam, Netherlands

Rouf MA, (1984), *Fundamental Properties of brickwork with particular emphasis to brickwork arches*, Thesis, University of Liverpool.

Saltelli A, Chan K, Scott EM, (2004), *Sensitivity Analysis*, Wiley Series in Probability and Statistics", John Wiley and Sons, Inc., New York.

Shin HS, Pande GN, (2000), *On self-learning finite element codes based on monitored response of structures*, Computers and Geotechnics, vol. 27 , pp. 161-178.

Smith, Colin, and Matthew Gilbert. "Application of discontinuity layout optimization to plane plasticity problems." *Proceedings of the Royal Society of London A: Mathematical, Physical and Engineering Sciences*. Vol. 463. No. 2086. The Royal Society, 2007.

Stevin S, (1586), *De Beghinselen der Weeghconst*. (In The Principal Works of Simon Stevin, vol. 1,

Sustainable Bridges (2007), *Masonry Arch Bridges Background document D4.7*, Sustainable Bridges, EU FP6.

Terzaghi, K. (1936), *Stress Distribution in Dry and in Saturated Sand Above a Yeilding Trap-Door*. Proceedings, First International Conference on Soil Mechanics and Foundation Engineering, 307-311.

Terzaghi, K. (1943), *Theoretical Soil Mechanics*, John Wiley and Sons, New York, pp. 66-76

Towler KDS, Sawko F, (1982), *Limit State behaviour of brickwork arches*, Proc. 6th Int. Brick masonry conference, Rome, Italy.

Towler KDS, (1985), *Applications of nonlinear finite element codes to masonry arches*.=, Proc. 2nd Int. Conference on Civil and Structural Engineering computing, Edinburgh, Civil-Comp Press.

Wang J, Melbourne C, Tomor A, (2010), *Development of Pippard's elastic method for the assessment of short span masonry arch bridges*, Proc. 6th Int. Conference on Arch Bridges, pp. 490-497.

White D, Take W, (2002). *GeoPIV particle image velocimetry (PIV) software for use in geotechnical testing*. Technical Report 322. Cambridge, Geotechnics Group, Cambridge University Engineering Department.

Whittle AJ, Hashash YMA, Whitman RV, (1993), *Analysis of deep excavation in Boston*. Journal of technical Engineering, vol. 119, no. 1, pp. 69–90.

Zienkiewicz OC, Cheung YK, (1967), *The finite element method in structural and continuum mechanics*, London, McGraw-Hill